Al-3.5Cu-1.5Mg-1Si alloy and related materials produced by selective laser melting

Von der Fakultät Maschinenwesen der Technischen Universität Dresden
zur Erlangung des akademischen Grades
Doktoringenieur (Dr. -Ing.)
angenommene

DISSERTATION

von
Master of Engineering
Pei Wang
geboren am 25.02.1989 in Luoyang City, Henan Province, China

Tag der Einreichung: 03.05.2018

Tag der Verteidigung: 21.08.2018

1. Gutachter: Prof. Dr.-Ing. habil. Dr. h.c. Jürgen Eckert

2. Gutachter: Prof. Dr. Xin Lin

Contents

Abstract

Selective laser melting (SLM) is an additive manufacturing technology, which utilizes a layer-by-layer deposition process controlled by a three-dimensional computer model to produce fully dense materials with complex and intricate geometries. SLM not only has all the advantages of additive manufacturing, such as flexibility in component shape and intricacy, as well as optimized material use, but is also characterized by a significantly high solidification rate. Up to now, only a few series of Al-based alloys have been successfully fabricated using SLM. Most research has focused on 4xxx series alloys, which have good weldability and hardenability, and are easy to process. With the development of the technology and the understanding of the fundamental characteristics of the process, the research focus has been progressively shifted to the analysis of the 2xxx and 7xxx series alloys fabricated using SLM. All the results indicate that these Al-alloys display fine microstructures and considerably improved mechanical properties compared to the corresponding materials synthesized by conventional techniques.

In the course of this thesis, a heat-treatable Al-3.5Cu-1.5Mg-1Si alloy and related materials (composites and hybrid materials) have been successfully fabricated by selective laser melting and characterized in terms of densification, microstructure, heat treatment, mechanical properties as well as tribological and corrosion behavior.

The as-prepared SLM Al-Cu-Mg-Si samples show a fine-granular microstructure in the individual melt pool of the laser tracks and a coarse-granular microstructure in the areas between the tracks. After T6 heat treatment, the grain size of the specimens increases slightly and the Q phase formed in the as-prepared specimens transforms to $Al_2Cu(Mg)$, Mg_2Si, and Al_xMn_y. All Al-Cu-Mg-Si specimens before and after heat treatment fracture around the defects that were generated during processing and show intergranular fracture along columnar grains upon tensile quasi-static loading. The as-fabricated samples exhibit a good tensile strength along with appreciable plastic deformation. After T6 heat treatment, the tensile strength increases due to the formation of nano-sized $Al_2Cu(Mg)$ precipitates, while the ductility remains fairly similar.

Compared with the standard AA2024 alloy O, the fine secondary phase of the SLM Al-Cu-Mg-Si alloy leads to lower specific wear rate and average coefficient of friction. After T6 heat treatment, the SLM Al-Cu-Mg-Si alloy displays a lower specific wear rate but similar average coefficient of friction compared with the heat-treated AA2024 alloy, indicating that the SLM Al-Cu-Mg-Si alloy has good overall tribological properties.

In 0.1 M NaCl solution, the corroded surface of the standard AA2024 alloy O and T6 exhibits a significant pitting phenomenon around the noble intermetallics. For the SLM Al-Cu-Mg-Si alloy, there is no obvious peripheral pitting phenomena around the secondary phase but a significant exfoliation phenomenon. Moreover, the results also indicate that SLM Al-Cu-Mg-Si alloys before and after T6 heat treatment have a lower corrosion rate than the AA2024 alloy at the same heat treatment condition.

The comprehensive analysis of the effect of composition on the microstructure and the properties of alloys processed by SLM would require the expensive production of a suitable amount of powders with proper compositions by gas atomization. With the aim of designing new alloy compositions and to examine the phases and microstructures of SLM Al-Cu alloys and to correlate their microstructures with the observed mechanical properties, Al-xCu (x = 4.5, 6, 20, 33 and 40 wt. %) alloys have been synthesized in-situ by SLM from mixtures of Al-4.5Cu and Cu powders. The results indicate that the insufficient Cu solute diffusion during the layer-by-layer processing results in an inhomogeneous microstructure around the introduced Cu powders. The boundaries between the melt pools of all alloys display different microstructural characteristics, indicating the occurrence of both high- and low-cooling-rate zones as well as heat-affected zones. With increasing Cu content, the Al_2Cu phase in the alloys increases improving the strength of the material. SLM Al-33Cu alloy with a nano-eutectic microstructure exhibits the highest compressive strength exceeding 1000 MPa. These results show that powder mixtures can be used for the synthesis of SLM composites but the reaction between the matrix and the second-phase should be considered carefully.

A heat treatable TiB_2/Al-3.5Cu-1.5Mg-1Si composite was successfully fabricated by SLM of powder mixture. The results show that the phase distribution and phase transformation in the matrix of the composite before and after heat treatment is the same as observed in the unreinforced Al-Cu-Mg-Si alloy. The introduction of the TiB_2 particles results in a remarkable grain refinement, which causes an improved compressive strength of the SLM TiB_2/Al-Cu-Mg-Si composite in comparison to the unreinforced Al-Cu-Mg-Si alloy. Additionally, the formation of Al_2Cu(Mg) precipitates further enhances the compressive strength of the heat treated TiB_2/Al-Cu-Mg-Si composite.

Finally, an Al-12Si/Al-3.5Cu-1.5Mg-1Si hybrid with a good interface was fabricated successfully. The results indicate that the SLM hybrid alloys along the building direction exhibits successively four zones: Al-12Si zone, interface zone, precipitate free zone and Al-Cu-Mg-Si zone. This hybrid alloy shows a good yield strength and elongation at room temperature, indicating an effective potential of selective laser melting in the field of hybrid manufacturing.

Kurzfassung

Das selektive Laserschmelzen (nachfolgend als SLM bezeichnet) ist ein additives Fertigungsverfahren, das durch den schichtweisen Aufbau eines dreidimensionalen Computermodels dichte Probenkörper erzeugt, die durch eine komplexe Geometrie gekennzeichnet sind. Das SLM-Verfahren ist, neben den Vorteilen der additiven Fertigung wie der Flexibilität und Komplexität in der Bauteilform, ebenso durch hohe Erstarrungsraten charakterisiert. Bislang wurden nur wenige aluminiumbasierte Legierungen erfolgreich mittels SLM verarbeitet. Der große Teil der Forschung fokussiert sich auf die Aluminiumlegierungsserie 4xxx, die eine gute Schweißbarkeit und Härtbarkeit zeigt und ebenso problemlos zu verarbeiten ist. Durch die Entwicklungen der Technologie und dem Verständnis fundamentaler, den Prozess betreffender Charakteristika wurde der Forschungsschwerpunkt zunehmend auf die Untersuchung der mittels SLM hergestellten Legierungsserien 2xxx und 7xxx verschoben. Alle Ergebnisse zeigen, dass diese Aluminiumlegierungen ein feines Gefüge und beträchtlich verbesserte mechanische Eigenschaften, verglichen mit konventionell synthetisiertem Material, aufweisen.

Im Zuge dieser Dissertation wurde die vergütbare Legierung Al-3,5Cu-1,5Mg-1Si sowie artverwandte Werkstoffe (Verbundwerkstoffe und Mischungen) erfolgreich durch selektives Laserschmelzen verarbeitet und hinsichtlich relativer Dichte, Gefüge, Wärmebehandlung, mechanischen Eigenschaften sowie tribologischen und korrosiven Verhaltens untersucht.

Die Al-Cu-Mg-Si SLM-Proben zeigen ein feinkörniges Gefüge innerhalb des Schmelzbereiches der Laserbahnen und ein gröberes Gefüge zwischen den Schmelzbahnen. Nach der T6-Wärmebehandlung steigt die mittlere Korngröße leicht an und die Q-Phase wandelt sich in Al_2Cu(Mg), Mg_2Si, and Al_xMn_y um. Zusammengefasst kann gesagt werden, dass alle Al-Cu-Mg-Si Proben, vor und nach der Wärmebehandlung, in der Nähe von Defekten, die während des Prozesses entstanden sind, versagen und ein intergranulares Risswachstum entlang stängelförmiger Körner bei quasistatischer Zugbelastung zeigen. Die Proben im Ausgangszustand weisen eine gute Zugfestigkeit zusammen mit einer beträchtlichen plastischen Dehnung auf. Nach der T6-Wärmebehandlung steigt die Zugfestigkeit, aufgrund der Bildung von nanoskaligen Al_2Cu(Mg)-Ausscheidungen, an, während die Duktilität annähernd gleich bleibt.

Verglichen mit der Standardlegierung AA2024 O führt die feine Zweitphase des SLM-prozessierten Al-Cu-Mg-Si zu einer niedrigeren spezifischen Verschleißrate und einem ähnlich

durchschnittlichen Reibungskoeffizient. Nach der T6-Wärmebehandlung weist das SLM-prozessierte Al-Cu-Mg-Si eine niedrigere Verschleißrate und einen vergleichbar durchschnittlichen Reibungskoeffizient, verglichen mit der wärmebehandelten AA2024 auf, dies zeigt, dass das SLM-gefertigte Al-Cu-Mg-Si im Allgemeinen durch gute tribologische Eigenschaften charakterisiert wird.

In 0.1M NaCl-Lösung zeigen die korrodierten Oberflächen der Standardlegierungen AA2024 O und T6 einen signifikanten Lochfraß in der Nähe von edleren intermetallischen Verbindungen. Für das SLM-hergestellte Al-Cu-Mg-Si sind keine offensichtlichen Anzeichen von Lochfraß in der Nähe der zweiten Phase zu erkennen, allerdings tritt ein deutliches Abblättern auf. Außerdem dokumentieren die Ergebnisse, dass das SLM-prozessierte Al-Cu-Mg-Si vor und nach der Wärmebehandlung durch eine geringere Korrosionsrate gekennzeichnet ist, als AA2024 bei gleichen Wärmebehandlungsbedingungen.

Die umfangreiche Analyse der Zusammensetzung und die Eigenschaften der mit SLM-prozessierten Legierungen würde eine kostenintensive Produktion von einer geeigneten, durch Gasverdüsung hergestellten, Pulvermenge mit korrekter Zusammensetzung nach sich ziehen. Mit dem Ziel neue Legierungszusammensetzungen zu designen und die Phasen und das Gefüge von SLM-prozessierten Al-Cu zu untersuchen und um deren Gefüge mit den beobachteten mechanischen Eigenschaften zu korrelieren wurde Al-xCu (x = 4.5, 6, 20, 33 and 40 wt. %) im SLM-Prozess in-situ durch Vermengung von Al-4,5Cu und Cu-Pulver hergestellt. Die Ergebnisse zeigen, dass eine unzureichende Diffusion von Kupfer während der schichtweisen Herstellung zu einem inhomogenen Gefüge im Umfeld des eingeführten Kupferpulvers führt. Die Grenzen zwischen den Schmelzpools aller Mischungen zeigen verschiedene Gefügecharakteristika mit Hinweisen auf das Vorhandensein sowohl einer Zone mit hoher als auch niedriger Abkühlgeschwindigkeit sowie Wärmeeinflusszonen. Mit ansteigendem Kupfergehalt erhöht sich der Anteil der Al_2Cu-Phase in der Legierung und der Festigkeit des Materials. SLM-prozessiertes Al-33Cu mit einem nano-eutektischem Gefüge weist die höchste Druckfestigkeit von mehr als 1000 MPa auf. Diese Ergebnisse dokumentieren, dass Pulvermischungen für die Herstellung von SLM-Verbundwerkstoffen genutzt werden können, das Verhalten zwischen Matrix und zweiter Phase jedoch sorgfältig betrachtet werden muss.

Ein wärmebehandelbarer Verbundwerkstoff aus TiB_2/Al-3,5Cu-1,5Mg-1Si wurde erfolgreich mittels SLM aus einer Pulvermischung hergestellt. Diese Ergebnisse dokumentieren, dass die

gleiche Phasenverteilung und Phasenumwandlung in der Matrix des Verbundwerkstoffes vor und nach der Wärmebehandlung auftreten wie in unverstärktem Al-Cu-Mg-Si. Die Einführung von TiB_2 Teilchen resultieren in einer spürbaren Kornfeinung, die eine Verbesserung der Druckfestigkeit von TiB_2/Al-Cu-Mg-Si SLM-Verbunden nach sich zieht im Vergleich zu unverstärkten Al-Cu-Mg-Si. Die Bildung von Al_2Cu(Mg) Ausscheidungen verstärkt zusätzlich weiter die Druckfestigkeit der wärmebehandelten TiB_2/Al-Cu-Mg-Si Verbunde.

Schlussendlich kann festgestellt werden, dass eine Verbindung aus Al-12Si/Al-3,5Cu-1,5Mg-1Si mit einer guten Grenzfläche erfolgreich hergestellt wurde. Die Ergebnisse zeigen in den SLM-Verbindungen entlang der Baurichtung erfolgreich vier Zonen: die Al-12Si Zone, das Verbindungszentrum, die ausscheidungsfreie Zone und die Al-Cu-Mg-Si Zone. Die Verbindungen weisen eine gute Streckgrenze und Dehnung bei Raumtemperatur auf und demonstrieren ein effektives Potential des selektiven Laserschmelzens im Feld der Verbundmaterialien.

Aims and objectives

Selective laser melting (SLM) has gradually emerged from a peculiarity to a research field in the recent decade due to the advantages of materials performance and the design of complex geometries. Owing to the rapid solidification during SLM processing, SLM alloys with non-equilibrium microstructures can achieve better chemical/physical properties than alloys fabricated by conventional processing technologies. Moreover, the method of selectively melting and the layer-by-layer processing strategies improve the design flexibility of complex structures and meet the demand of the cost-saving and energy-saving materials processing, especially in the aerospace and automobile industries. Thus, the development of selective laser melting has been focused on both scientific and engineering aspects. However, because of the short R&D course of the SLM technology, just a few alloys could be developed and applied to the real industry. To take aluminum alloys as an example, the selective laser melting technology was firstly and widely used to fabricate the Al-Si series alloys (Al-12Si, Al-10Si-Mg, Al-7Si-Mg and Al-9Si-3Cu) due to their excellent castability and weldability. In order to get improved mechanical and chemical properties, the attention was focused on the heat treatable SLM Al alloys (Al-Cu and Al-Zn series alloys). However, for these heat treatable Al alloys, Cu and Mg are easy to lead to the formation of pores and solidification cracks during the high cooling rate, and the serious evaporation of low-boiling point elements (such as Zn and Mg) also can cause the formation of processing defects. Therefore, the research of how to get crack-free and near-fully dense heat-treatable Al alloys by SLM is a hot topic in the recent period, and their microstructures and properties also attract much attention. Accordingly, the present thesis focuses on the fabrication and characterization of the SLM heat treatable Al-Cu-Mg-Si alloy and its related materials.

The specific objectives of this thesis are:

- ➢ An Al-3.5Cu-1.5Mg-1Si alloy was chosen as a basis for the alloys examined in this work due to its most common composition in the Al-Cu series alloys (close to AA2024 and AA2028 alloys: widely used in many aerospace structural applications, such as in fuselage structures, wing tension members, wing shear webs and ribs). Based on the variation of the composition of the four elements (Al, Cu, Mg and Si), Al-Cu-Mg-Si alloys with different properties have been developed to be applied in different fields. Therefore, the research based on the SLM Al-Cu-Mg-Si alloy is of great significance for the industrial application. Moreover, the investigation of the SLM Al-Cu-Mg-Si alloy can contribute to a better understanding of the feasibility of SLM processing for Al-Cu series alloys and the relationship between the compositions, microstructures and properties.

- Based on the Al-Cu phase diagram and the successful fabrication of Al-3.5Cu-1.5Mg-1Si alloy by SLM, Al-xCu alloys (x = 4.5, 6, 20, 33, and 40 wt. %) were synthesized by selective laser melting of powder mixtures, which gives additional understanding of the rapid solidification and diffusion of the SLM Al-Cu-Mg-Si alloys and their related materials (e.g, composites and hybrid alloys) during SLM processing.
- Aluminum matrix composites (AMCs) display high specific properties and are, therefore, particularly attractive for automotive and aerospace applications. Unfortunately, their application is limited because of the difficulties to synthesize composite parts with complex geometry by conventional technologies. In order to further improve the properties of Al-based materials and expand their application, TiB_2/Al-3.5Cu-1.5Mg-1Si composite was designed and fabricated by selective laser melting.
- In order to broaden the application of the SLM Al alloys and take advantages of the good properties of various Al series alloys in the complex working condition, the Al-12Si/Al-3.5Cu-1.5Mg-1Si hybrids (non-heat treatable Al-Si series and heat treatable Al-Cu series alloys) were designed and fabricated by SLM.

All of these works can broaden the SLM materials and provide the theoretical fundamental and practical experience for the fabrication and analysis of the other new SLM materials.

CHAPTER 1

Technical and theoretical background

The present chapter will firstly introduce the historical development of additive manufacturing (AM) technology and the basic principles of the current AM technologies, with particular emphasis on selective laser melting (SLM). Then, the working principles and the processing parameters of selective laser melting, the phenomena occurring during processing, and the current SLM alloys are described systematically. Also, the basic knowledge of the classification and application of Al alloys is summarized. The last part of this chapter is dedicated to the current research status of SLM Al alloys, including the densification behavior, processing drawbacks and chemical/physical properties.

1.1 Additive manufacturing

Additive manufacturing technologies (AM) are a relatively new concept of the manufacturing processing based on the computer technology, which lies in a stark contrast to traditional subtractive manufacturing processes. This concept was put forward firstly by JF Blanther and the first corresponding patent was approved in USA in 1892 [1]. After that, thousands of patents show a tidal wave of applications. The first commercial Stereo Lithography Apparatus (SLA) was sold in 1988, which marks the birth of the applied Rapid Prototyping (RP). Rapid Prototyping is the predecessor of additive manufacture technologies. Because the latter appellation highlights the concept and processing strategies of the technology, the terminology (Additive Manufacture technology) was accepted and referred by more and more fields [2,3]. With the help of the additive manufacturing strategy and the computer aided design, AM can produce complex parts simultaneously without the tedious post-processing [4-7]. Furthermore, AM meets the increasing demand of cost-saving and energy-saving processing in different industries. Accordingly, with the development of the laser technology and this derivative technology, more and more materials can be successfully processed, including polymers [8], glasses [9], metals [10], metallic glasses [11], ceramics [12] and biological cells [13].

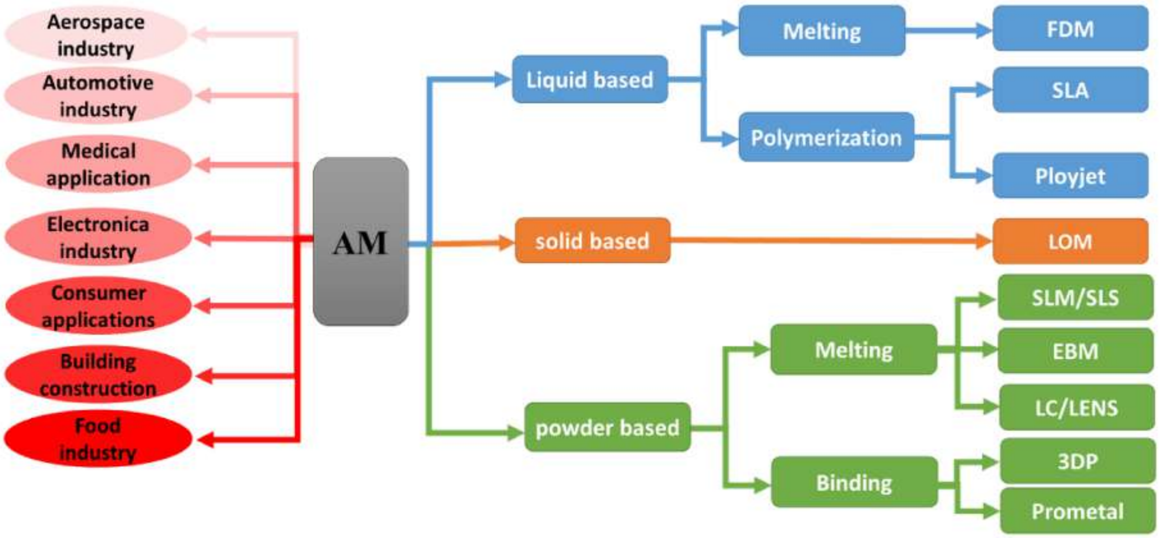

Figure 1.1 Categories of AM technologies and their applications.

Until now, in order to fabricate the different materials, dozens of related technologies have been developed and applied in different fields, as shown in Fig. 1.1 [2,3,14-17], such as Stereo-Lithography Apparatus (SLA), Fused Deposition Modelling (FDM), Ink Jet Printing, Three Dimensional Printing (3DP), Selective Laser melting (SLM), Selective Laser Sintering (SLS), Laser Cladding (LC), Laminated Objective Manufacture (LOM), Acoustic Droplet Ejection (ADE) and Electron Beam Melting (EBM). All technologies have their own advantages in the different aspects, such as feasibility of the processing, surface quality, properties of the products and the forming efficiency.

Figure 1.2 Applications of additive manufacturing in the different fields [18].

With the introduction of the additive manufacturing concept into the industry, the products fabricated by AM are brought into our daily life from the low capital-intensive industry (e.g., food industry, personal care, clothes, and art ware & crafts [19-21]) to high capital-intensive industry (e.g., heavy equipment of mining, huge buildings, automotive industry and the aircraft industry [22,23]), from the low-end market to sophisticated manufacturing markets [22-24], as described in Fig. 1.1. Some products, which are impossible or difficult to process by the conventional technologies, can be now designed and fabricated cheaply. Accordingly, the variety of products meets the needs of consumers and enriches our colorful world, as shown Fig. 1.2.

In order to have an in-depth understanding of the characteristics of the different AM technologies, this thesis will give a brief introduction on some typical and popular technologies, mainly metal-based materials.

(1) Stereo Lithography Apparatus (SLA) [14]

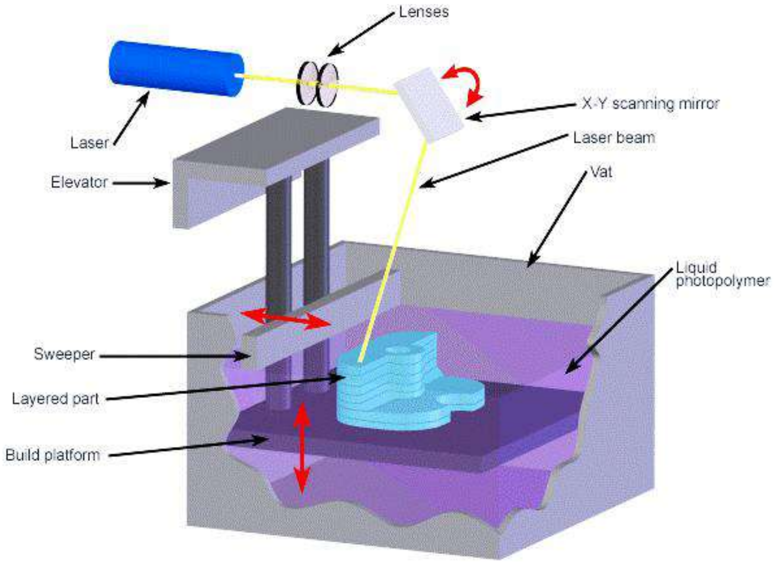

Figure1.3 Schematic of the Stereo Lithography Apparatus [25].

The SLA is the first commercial AM technology which was invented by Charles Hull in 1988 at the 3D Systems Company [26]. The process begins with the vat filled with the liquid photopolymer materials and the build platform with an elevator set just below the surface of the liquid resin, as shown in Fig. 1.3. The laser beam follows the CAD program and leads to the photo polymerization process (linking the monomers into chain-like polymers) of the materials; this causes the polymer to harden precisely at the point where the ultraviolet light hits the surface [14].

After that, the sweeper moves across the cross-section parts and recoats the solidified surface with fresh material. In this way, the materials are fabricated from bottom to top through the layer-by-layer strategies in accordance with the scheduled CAD model.

The SLA technology is applied for acrylate materials [14]. The manufacturing accuracy of SLA is around 0.025 mm [14]. The products are used in aerospace, armaments, automotive, consumer electronics, consumer produces, toys, industrial equipment, and medical equipment [14].

(2) Laser Cladding (LC) [27-29]

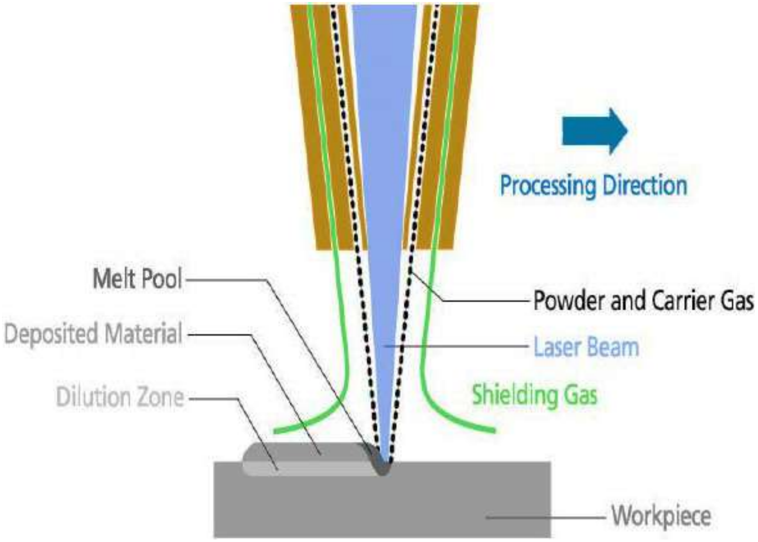

Figure 1.4 Schematic of the Laser Cladding [30].

Laser Cladding is a new AM processing technique, where powder delivery and powder melting are undertaken simultaneously. Compared with the layer-by-layer principle of other AM technologies, the LC technique, being based on the line-by-line strategy, is more flexible for the component repair, composites design and the design of structural gradient material [31]. Therefore, in recent years, there are lots of derivative technologies, such as Laser Direct Cladding (LDC), Laser Engineered Net Shaping (LENS), Direct Metal Deposition (DMD), Direct Light Fabrication (DLF) and Selective Laser Cladding (SLC) [32-34]. But all of these technologies are based on the same principles of the laser cladding. As shown in Fig. 1.4, a carrier gas containing fine metal powder sprays out via a coaxial nozzle through the path of the laser beam, which is cladded slightly onto the workpiece. However, similarly to the other AM, the LC technology also utilizes a STL file generated from a CAD model to build an object.

The LC technology can be applied to various metals. The manufacturing accuracy of this processing is above 1 mm, which is its main drawback [27]. However, due to the shorter production cycle and the outstanding advantages of the parts repair, this technology is widely used in the aerospace and automobile industries [28].

(3) Selective Laser Melting (SLM) [23,35]

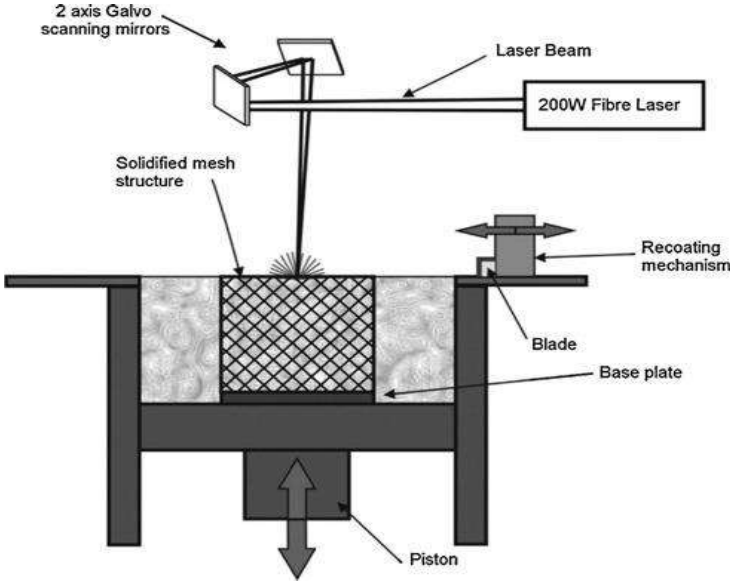

Figure 1.5 Schematic of Selective Laser Melting [36].

Selective laser melting utilizes the same working principle to the SLA technology. Due to the improvement of the laser source, SLM technology has the ability to fully melt the raw metal powder to fabricate the complex products. In general, selective laser melting (SLM) was developed in the last decade, which is based on selective laser sintering (SLS) technology [37,38]. SLS technology utilized the liquid phase sintering (LPS) mechanism involving a partial melting of the powder (semisolid consolidation mechanism) [35]. Different from the LPS mechanism, SLM technology utilizes the complete melting/solidification mechanism. Therefore, compared to SLS alloys, SLM alloys show a significant improvement of the densification rate, surface smoothness, microstructural homogeneity and mechanical properties [35,39]. Thus, the use of SLM is focused on the fabrication of metallic parts. As shown in Fig. 1.5, this technology is one of a layer-wise material addition techniques that allows generating complex 3D parts by selectively melting successive layers of metal powder on top of each other with the thermal energy supplied by a focused and computer-controlled laser beam [40].

The SLM technology is mainly used for the metals processing. Because of the higher manufacturing accuracy (around 0.02 mm) and less post-processing, this technologies are widely used to produce materials with complex geometry, strong personalized customization and good performance [40]. Therefore, this technology is selected as my thesis topic and will be discussed in more detail in the next section.

(4) Electron Beam Melting (EBM) [10,17,41]

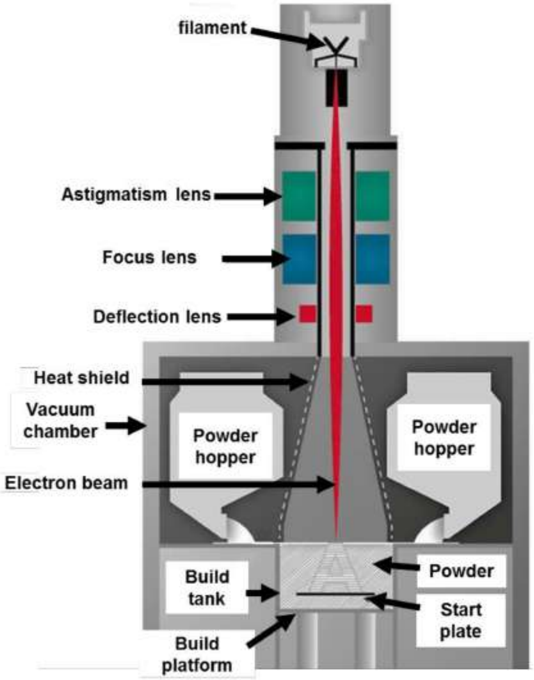

Figure 1.6 Schematic of Electron Beam Melting [42]

Electron beam melting (EBM) is becoming a viable additive manufacturing technology for a rapid fabrication of metallic parts directly from 3D CAD model like SLM (Fig. 1.6). The main difference between EBM and SLM is that EBM utilizes the electron beam column as heating source instead of the laser beam of SLM. The change of the heating source broadens the equipment design and has an effect on the microstructure and properties of the materials [43].

The EBM is also mainly used for the processing of metals. The manufacturing accuracy of EBM processing (around 0.1 mm) is worse than SLM [44]. Compared with the AM of metals, especially SLM, the lower residual stress generated during the EBM processing is the main advantage for the synthesis of metals with high crack susceptibility [10].

1.2 Selective laser melting (SLM)

1.2.1 Working principle

Selective laser melting (SLM) is an emerging smart additive manufacturing technology and is mainly used to produce metals and metal matrix composites [23,45]. It was developed by Dr. M. Fockele and Dr. D.Schwarze of F & S Stereolithographietechnik GmbH, and Dr. W. Meiners, Dr. K. Wissenbach and Dr. G. Andres of the Fraunhofer ILT institute. They firstly utilized this new technology based on the forming of the metallic powder to produce metallic components. The patent for this technology was firstly applied in 1997 to the German Patent and Trade Mark Office and published in 1998 [23]. SLM is a powder bed fusion process that uses high intensity laser as an energy source to fuse selectively regions of powder, accumulate the products with a layer by layer strategy based on the computer aided 3D design (CAD) data, as mentioned above. The processing schematic is shown in Fig. 1.7.

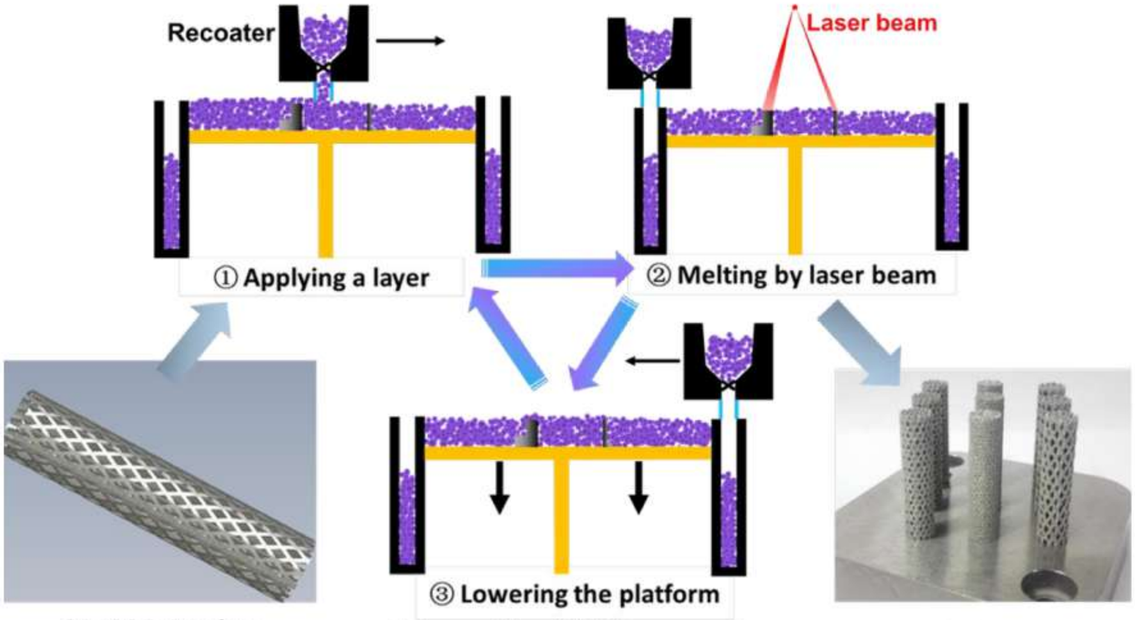

Figure 1.7 Steps involved in the SLM production from 3D design to finial parts.

SLM is a complex processing, which needs the precise control of numerous parameters to get fully-dense materials with ideal microstructures [46]. The main parameters that control the quality of the final product include the laser power (P), scanning speed (v_s), layer thickness (l_z) and hatch spacing (l_{hs}). With the adjustment of these parameters, the qualities and properties of the SLM products are optimized.

With the in-depth and extensive research on the SLM processing, more and more researchers realized that the values of volume-energy density (E_V) have a remarkable influence on the densification of SLM alloys [47,48], which can explain the formation of defects and microstructures [49,50]. Therefore, the volume-energy is important to overcome the formation of defects and improves the chemical/physical properties of SLM materials [51-55]. The volume-energy density (E_V) during SLM processing generally can be described by: [45, 56]

$$E_V = \frac{P}{v_s \times l_z \times l_{hs}} \ , \tag{1.1}$$

The design and fabrication from point, to line, to surface, and to volume are a typical feature of the SLM processing. Therefore, in addition to the four main parameters (P, v_s, l_{hs}, l_z and E_V), the hatch style is also an important factor, which has a significant effect on the properties of the SLM materials and on the design of their complex structures.

Typically, in order to solve the special problems, such as the microstructure homogeneity, surface roughness, residual stress distributions, and the cancellation of defects, the hatch style should be considered [57,58]. In addition, the optimization of the hatch style is a common method to decrease the defects and increase the relative density of the materials [50]. The proper hatch style is helpful to design microstructure and texture, which can have a significant effect on the mechanical properties [57,59,60]. As shown in Fig. 1.8, the ordinary hatch styles include the continuous single melt (A), the single melt (B), and the offset scanning (C), which can be treated as a scanning unit for one single layer. Also, combining with the scanning unit (A, B, and C), the chessboard (D) strategy can be used as the processing of a single layer as shown in Fig. 1.8. The scanning angle between each scanning unit also can increase the diversity of the hatch style (Fig. 1.8). With the increment of the scanning unit along the building direction, the residual stress, microstructure, texture and chemical/physical properties of SLM materials can be changed and further designed.

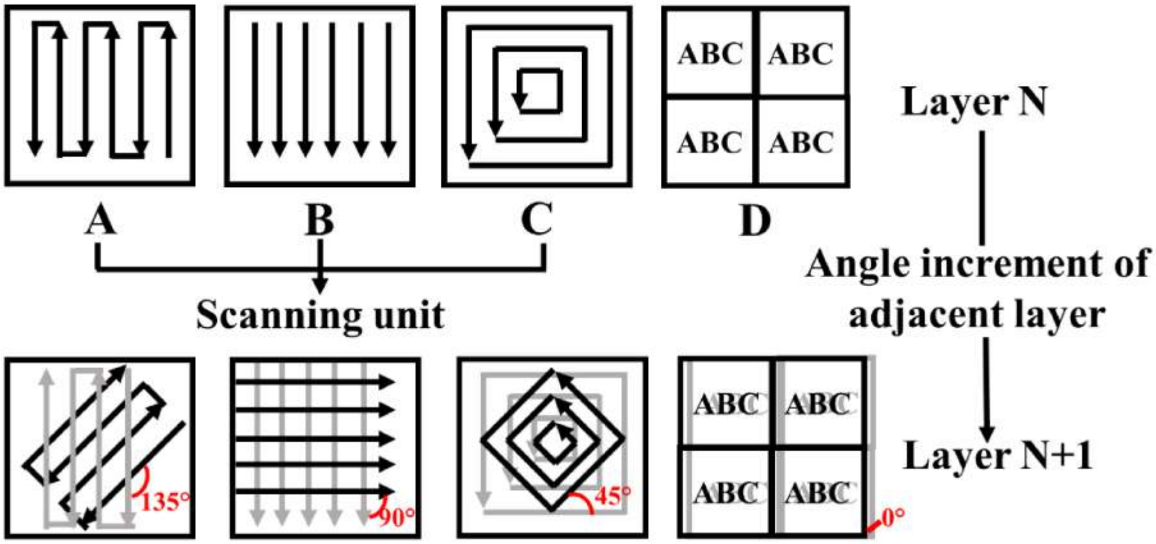

Figure 1.8 Overview of the scanning strategies: continuous single melt (A), the single melt (B), offset scanning (C), chessboard (D), which could use A, B, and C as the scanning unit to fill in the block), and angle increment of the adjacent layers.

1.2.2 Solidification fundamentals

Selective laser melting is an AM technology based on the laser beam, which results in a series of particular solidification phenomena during processing. The solidification fundamentals play a central role in understanding SLM processing, the microstructure evolution and the chemical homogeneity. Furthermore, it is also the necessary prerequisite for the pre-design of the mechanical properties and other chemical/physical properties of the materials.

Due to the laser beam used as the heating source of SLM, the heat transfer between the laser beam and materials is considered to be controlled by the inverse bremsstrahlung absorption mechanism (IBA) [61]. The IBA mechanism indicates that the interaction between a laser with high energy density (10^5-10^7 W/cm^2) and materials needs a short interaction time (10^{-3}-10^{-2} s) [62,63]. The high energy density and short interaction time result in the rapid heating rate and the following high cooling rate (10^3-10^5 K/s) [64-66]. On such a rapid cooling condition, the rapid solidification behavior is generally considered to occur during selective laser melting.

1.2.2.1 Basic equilibrium phase diagram

The equilibrium phase diagrams (Fig. 1.9) are generally used to reflect the liquid/solid composition of metallic alloys and the reaction rates at the solid/liquid interface [67]. It can provide a theoretical fundamental on the further understanding of non-equilibrium solidification.

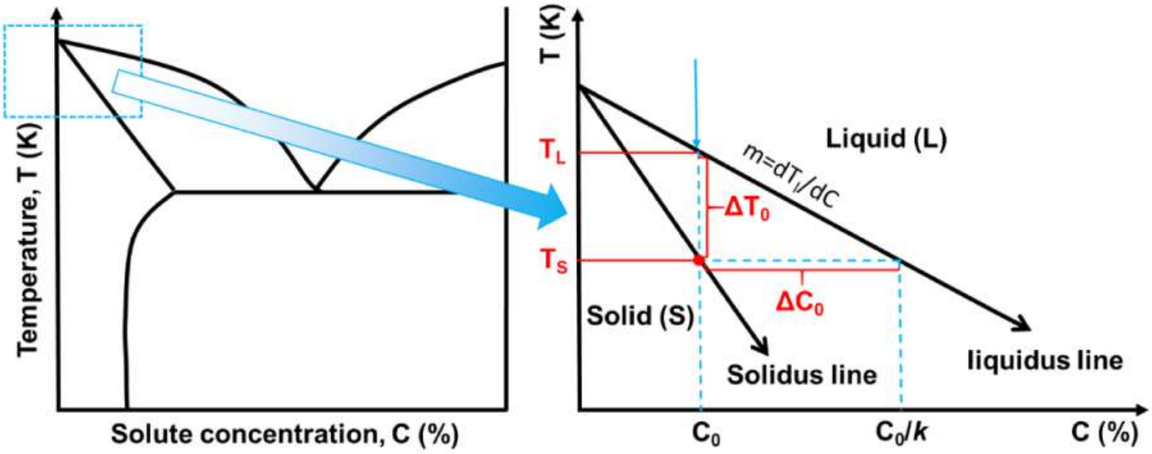

Figure 1.9 Solid/Liquid equilibrium. Adapted from Refs. [67,68]

In general, in order to simplify the mathematical treatment of solidification processes, the liquidus and solidus lines of the phase diagram are straight as shown in Fig. 1.9. The lines lead to two constant parameters: equilibrium distribution coefficient (k) and liquidus slope (m) [67]. The quantity $(k-1)m$ is generally defined as a positive value [67]. As shown in Fig. 1.9, the two important parameters, the liquidus-solidus temperature interval for an alloy of a given composition (ΔT_0) and the concentration difference between the liquid and solid solute contents at the solidus temperature (ΔC_0), are indicated as follows [67]:

$$\Delta T_0 = -m\Delta C_0 = T_L - T_S \ , \tag{1.2}$$

$$\Delta C_0 = \frac{C_0(1-k)}{k} \ , \tag{1.3}$$

These concepts and the mathematical equations are the basis for the understanding of non-equilibrium solidification, which will be highlighted in the next sections.

1.2.2.2 Rapid solidification mode and corresponding microstructures

The common understanding of the term, rapid solidification processing (RSP), is that the technology use the high cooling rate or large undercooling to obtain the high rates of advance of the solidification front (generally $V_s > 1$ cm/s) [67]. Under high cooling conditions, the rate of the interface displacement is comparable to or, even larger than the diffusion rate, causing that the solid/liquid (S/L) interface is no longer at equilibrium [67]. Therefore, new theories have been proposed to quantitatively describe the evolution of the S/L interface during rapid solidification. Generally, there are two famous theories applied in this description: the constitutional supercooling theory by Chalmer *et al*. [69,70], and the stability theory by Mullins and Sekerka (M-S theory) [71-73]. The former theory considers the thermodynamic aspect of the problem (mainly the effect of diffusion and thermal gradient on the S/L interface); the MS theory considers the surface tension of the interface and introduces the perturbation analysis of the temperature field and concentration field in the S/L field, which successfully predicts the existence of the absolute stability and provides the corresponding criterion for the interface stability.

1.2.2.3 Constitutional supercooling theory

The change of the solidification temperature (T) and concentration (C) field in the solidification front of the S/L interface are depicted in Fig. 1.10 according to equation 1.2. The main parameters include the distance from the S/L interface (z), the liquidus temperature (T_L) and the diffusion coefficient of the liquid (D). In order to investigate the stability of the interface, the temperature, T_q, is also defined, which is imposed by the temperature gradient arising from the heat flow occurring in the casting.

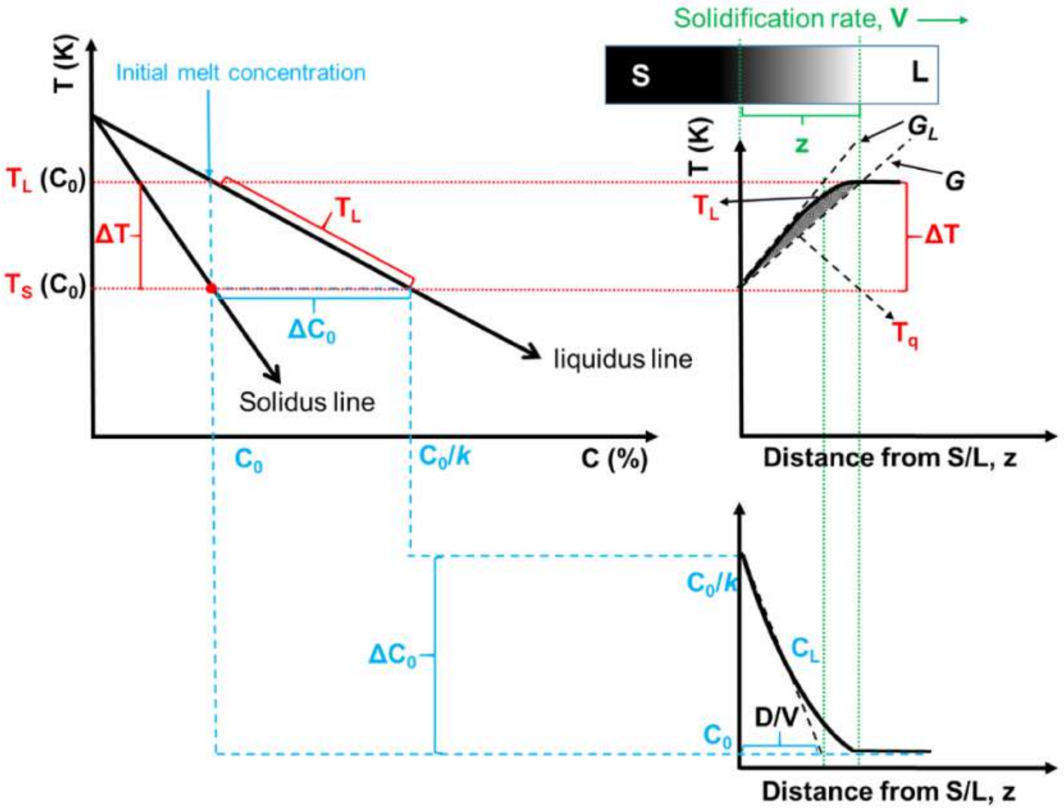

Figure 1.10 Relationship of phase diagram, concentration field in liquid and temperature field in liquid. Adapted from Refs. [67, 68].

The temperature gradient (G) resulting from the heat flux and the liquidus temperature (G_L) can be given by $(\frac{dT_q}{dz})_{z=0}$ and $(\frac{dT_L}{dz})_{z=0}$, respectively. Under the constitutional undercooling condition, the difference (Φ) between the liquidus temperature gradient and the heat-flux-imposed temperature gradient at the interface can be described as [67]:

$$\Phi = (\frac{d\Delta T}{dz})_{z=0} = (\frac{dT_L}{dz} - \frac{dT_q}{dz})_{z=0} = G_L - G \ , \tag{1.4}$$

The $\Phi = 0$ is the limiting condition for the constitutional supercooling. The positive Φ ($G < G_L$) can provide a positive driving force causing the perturbation [67]. The driving force results in an unstable planar interface leading to the formation of a dendritic microstructure [67].

According to the concentration field profile in Fig. 1.10, at the steady state, the flux balance is given by:

$$G_c = (\frac{dC_l}{dz})_{z=0} = -(\frac{V}{D})\Delta C_0 \ , \tag{1.5}$$

Depending on the equations 1.4, 1.5 and the relationship of the liquidus temperature gradient and concentration gradient ($G_L = mG_c$), the criterion for the existence of the constitutional supercooling can be written as [67]:

$$\Phi = mG_c - G > 0 \ , \tag{1.6}$$

or

$$\mathrm{G} < -\left(\frac{V}{D}\right)\Delta C_0 \ , \tag{1.7}$$

Also, because of the equation 1.2, the limit of constitutional undercooling can be expressed in the form [68]:

$$\frac{G}{V} = \frac{\Delta T}{D} \ , \tag{1.8}$$

According the above discussion, it is clear that to ensure a stable planar S/L interface, the actual temperature gradient G at the S/L interface must be at least $V\Delta T/D$, namely, $G \geq V\Delta T/D$ [68]. Moreover, the microstructure evolution from the planar to cellular, to columnar dendritic, and to equiaxed dendritic as a function of constitutional supercooling can be depicted reasonably in Fig. 1.11(a) [68]; these phenomena have been verified experimentally by numerous works [74,75]. As shown in Fig 1.11(a), the mushy zone, where dendrites (columnar or equiaxed) and the liquid phase coexist, can become wider with the increasing constitutional supercooling. Fig. 1.11(b) depicts the various solidification morphologies and their dependence on the temperature gradient (G) and the solidification rate (V). It indicates that the G/V value largely affects the morphologies of dendrites while $G \times V$ value influences the growth of dendrites, especially the dendrite arm spacing.

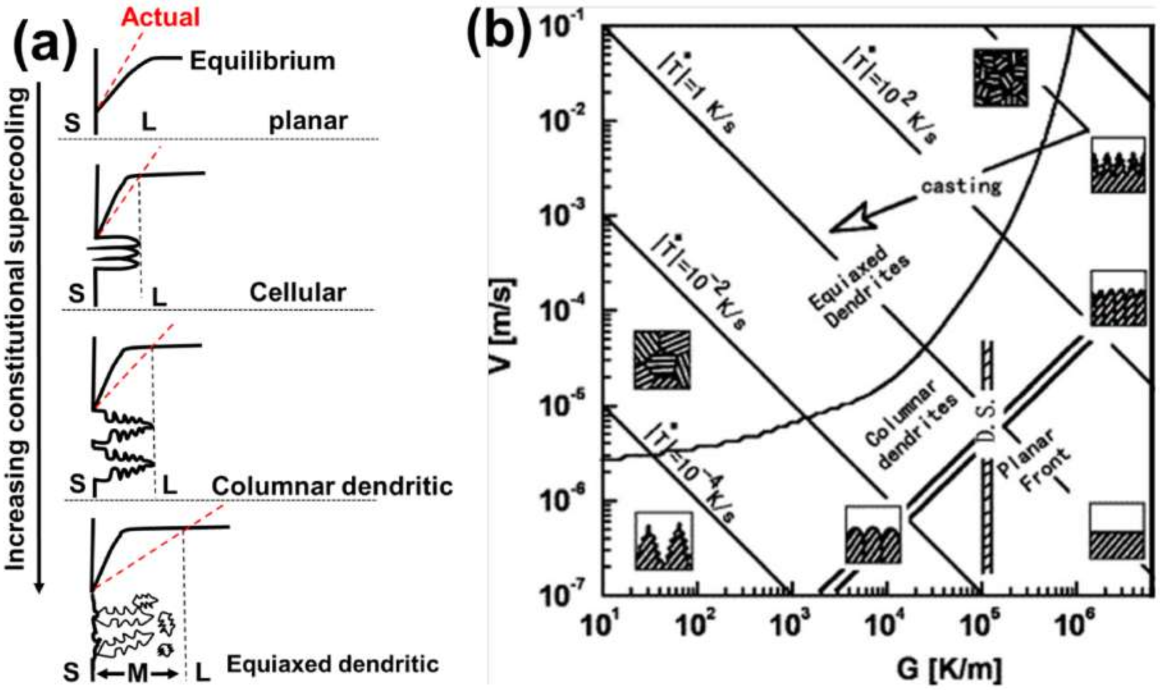

Figure 1.11 Effect of the constitutional supercooling on the solidification mode [60]; (b) schematic summary of *G*-*V* diagram with single phase solidification morphologies. Both adapted from Refs. [67, 76].

Simple theories similar to the constitutional supercooling theory cannot predict reasonably the columnar-to-equiaxed transition (CET), which needs to consider the effect of the nucleation sites and grain refinement [77].

1.2.2.4 Mullins-Sekerka theory

According to the mathematical perturbations analysis at the S/L interface, the S/L interface has a certain amplitude and the perturbed interface is considered as a two-dimension sine function [67]:

$$z = \varepsilon \sin(\frac{2\pi y}{\lambda}) \quad , \qquad (1.9)$$

where ε is the amplitude of the S/L interface and λ is the wavelength of the S/L interface.

The introduction of variable value of the perturbed interface (z) results in the two-dimension diffusion [67]. The solute distribution in the liquid, the temperature distribution in the liquid and the temperature distribution in the solid become variables value which are affected by ε and λ simultaneously. It is the main different assumption between the constitutional supercooling theory and the M-S theory. Due to the complex mathematical derivations and assumptions, in the present thesis, only the important equations of the M-S theory are listed to briefly explain the solidification behavior. In the M-S theory, the interface stability can be determined as [67]:

$$S(w^2) = -\Gamma\omega^2 - G + mG_c\xi_c \ , \tag{1.10}$$

where Γ is the Gibbs-Thomson coefficient. ξ_c is the stability parameters of the effective concentration gradient.

As shown in Equation 1.10, the interface stability is mainly affected by three factors: thermal gradient (G), the interface energy (related to Γ) and the concentration gradient (G_c). Obviously, when the interface energy is neglected, the criterion of M-S theory is similar to the constitutional supercooling theory, namely equation 1.6. Therefore, similar to Φ in the constitutional supercooling theory, a positive $S(w^2)$ can also provide the positive driving force causing the instability of the interface.

It should be mentioned that ξ_c is a function of the corresponding Péclet numbers (P_c) [67]:

$$\xi_c = 1 - \frac{2k}{\left\{\left[1+\left(\frac{2\pi}{P_c}\right)^2\right]^{\frac{1}{2}} - 1 + 2k\right\}} \ , \tag{1.11}$$

The analysis of equation 1.11 shows that the stability parameter is equal to unity at low Péclet numbers but tends towards zero as the Péclet numbers tends infinity. When the Péclet number is high but not infinite, ξ_c is approximately equal to $\pi^2/(kP_c^2)$ under a certain condition that $1/[1+(2\pi/P_c)^2]^{1/2}$ is approximately to $1-2\pi^2/P_c^2$ [67]. Under the criterion condition of the stable interface ($\xi_c \rightarrow \pi^2/kP_c^2$), other factors in Equation 1.10 can be substituted as following, namely the $S(w^2) = 0$, $G = 0$ (at very high solidification rate), $\omega = 2\pi/\lambda$, and $m\ G_c = \Delta T_0 V/D$. Thus [67]:

$$\frac{kV\Gamma}{\Delta T_0 D} = 1 \ , \tag{1.12}$$

When this condition is satisfied or exceed, the interface is stable regardless of the thermal gradient (G). This phenomena is referred as 'absolute stability', which also can be defined by a critical velocity [67]:

$$(V_a)_c \geq \frac{\Delta T_0 D}{k\Gamma} \ , \tag{1.13}$$

The absolute stability indicates that a planar interface also can be stable at high solidification rates and cooling rates, a phenomenon that has been verified in numerous works about laser melting [78-81].

Despite both theories have the limitation to the prediction of the solidification phenomena, they still have the important theoretical significance to explain the solidification phenomena of the new technologies, especially selective laser melting.

1.2.2.5 Solidification of SLM alloys

Due to the layer-by-layer processing strategy and the features of the laser melting, the solidification during SLM not only has the typical characters of the rapid solidification, but also displays a special solidification behavior.

Thijs *et al*. [59], Li *et al*. [82] and Gambaryan-Roisman *et al*. [83] investigated different SLM alloys using different measurement methods and reached a similar conclusion: the temperature along the building direction decreases with increasing distance from the top surface of melt pool, as shown in Fig. 1.12.

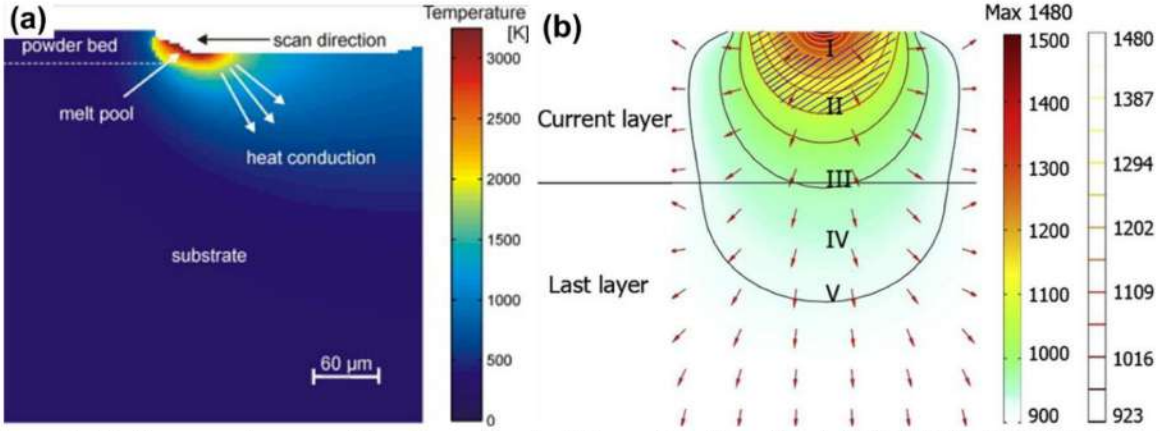

Figure 1.12 Temperature profile along the building direction for (a) SLM Ti-6Al-4V alloy [84] and (b) SLM Al-12Si alloy [82].

Depending on the investigation of the temperature distribution in the melt pool, the increase of the cooling rate and solidification rate from the bottom of the melt pool to the top are deduced further [82,85,86]. Due to the numerous works carried out on the solidification of the eutectic Al-33Cu alloy [80,87], Lei *et al*. selected the Al-33Cu alloy treated by the laser beam to study the relationship between the microstructure, the solidification rate and the mechanical properties. The results suggest that the microstructures from the boundary to the center of the melt pool are refined from the micro-scale (Fig. 1.13(l)) to the nano-scale (Fig. 1.13(c)). Moreover, along the same direction, the non-equilibrium microstructure changes from dendritic, to banded structure and even to the micro-segregation-free structure, whose theory is discussed in detail in Sections 1.2.2.3 and 1.2.2.4. In addition, the microstructure evolution of the Al-33Cu alloy from the boundary to the center of melt pool leads to the increase of hardness at the corresponding position [86]. Similar conclusions have also been reported in the investigations of SLM AlN/AlSi10Mg composite [65], SLM AlSi10Mg [85], SLM A357 alloy [88] and SLM TiC/Inconel 625 alloy [89].

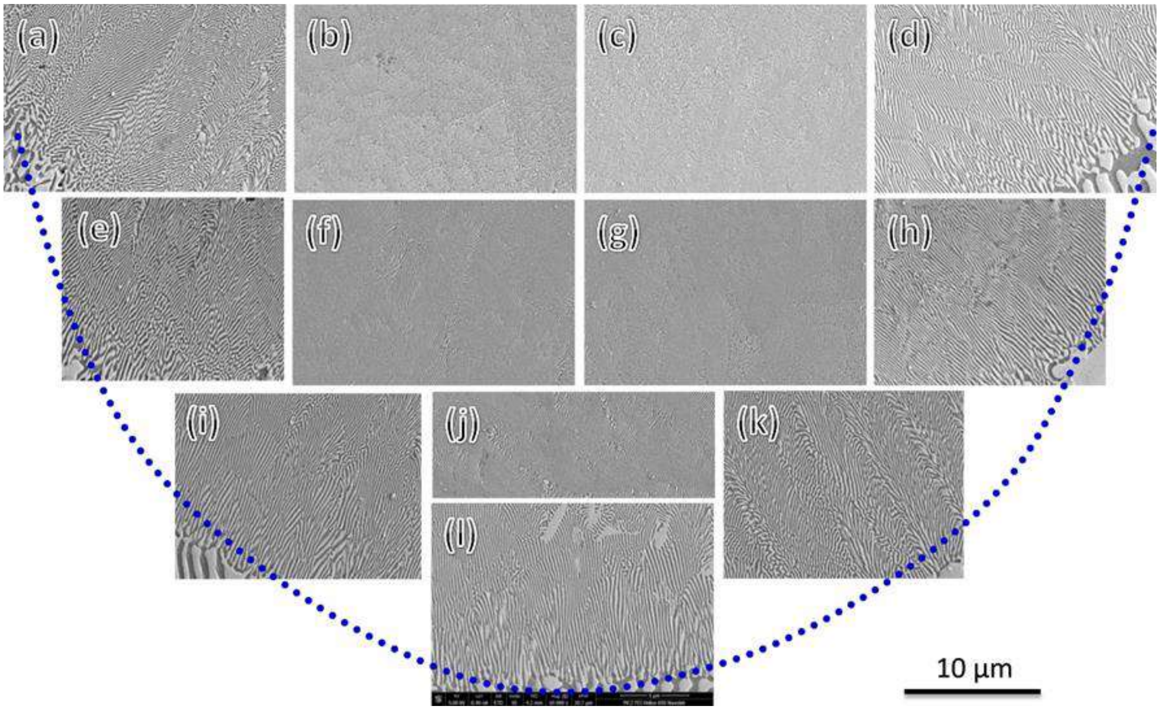

Figure 1.13 SEM images of the laser treated Al-33Cu alloy in the cross-section view of one laser track [86].

It should be highlighted that during SLM processing, the cooling rate of multilayers decreases gradually due to the heat preservation of the previous solidification [65,90]. The decline of the cooling rate results in a coarse microstructure and a reduced hardness in the initial layers [65,90]. However, the thermal effect of the former layer is reduced with increasing the processing layers, and the microstructure and the hardness gradually tend to be steady [65]. In addition, there is an obvious heat affected zone (HAZ) between the neighboring laser tracks (around the boundary of the melt pool), where the microstructure is significantly different from the microstructure in the melt pool, as shown in Fig. 1.14 [59,88,91].

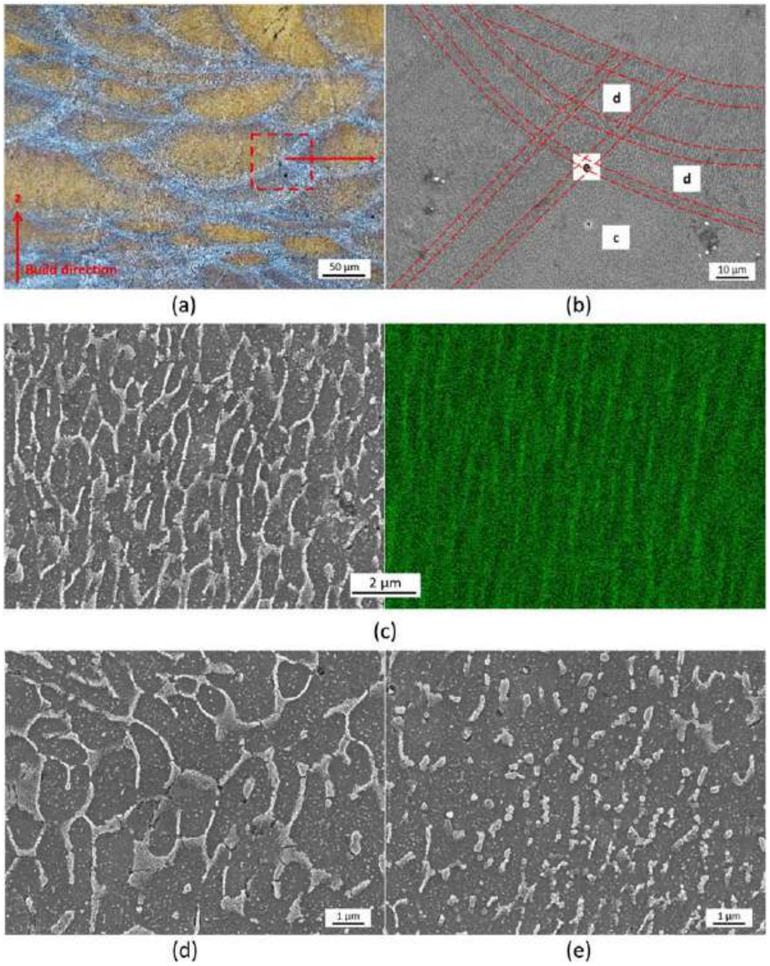

Figure 1.14 (a) Optical microstructure along the building direction; (b) SEM microstructure showing the arrowed area at higher magnification corresponding to (c) melt pool core with a EDS image, (d) melt pool boundary and (e) heat affected zone (HAZ) [88].

It is striking that differently from the inhomogeneous microstructure of the SLM alloys, the bulk metallic glass without any crystallization can also be fabricated by SLM, which shows a homogenous microstructure and even has no heat affected zone [11,92,93]. The fully glassy SLM parts also show a uniform nano-hardness distribution [11]. These special phenomena will be investigated in the future, which can help the better understanding of the solidification behavior during SLM processing.

1.2.3 Optimization factors

For the SLM processing, in addition to the main processing parameters mentioned in Section 1.2.1, other important factors which can be used to optimize the densification, microstructure and mechanical properties of the SLM alloys will be described in this section, including the powder properties, auxiliary design (contour and support parts), preheating and post-heating, protect-air circulation and air-pressure control [94].

1.2.3.1 Powder properties

The powder properties play an important role on the quality of the final SLM products. The chemical/physical properties of the powders (e.g., the density, the melting point, the composition, the flowability of powders, the shape factor and the spheroidization rate) can determine the type, the shape and the distribution of defects as well as the formability of the materials and the surface quality of the products [95-98].

The chemical composition of the powders can influence the melting conditions of the powders due to the IBA mechanism [99]. Therefore, it is important to determine the formability of an SLM alloy. The elements with low melting and boiling points in the starting powders, such as Zn and Mg, evaporate violently during SLM processing, which not only affect the composition of the SLM alloys but also result in the instability of the optimized parameters [96,100]. This behavior directly causes the formation of disastrous defects of the SLM alloys. Therefore, until now, the SLM processing of 7xxx series Al alloys, which is the most widely useful Al alloy in the aviation and aerospace application, is still an unresolved problem. However, through the optimization of the chemical composition, the formation of defects such as cracks, pores can be avoided [101,102]. Also, the low oxygen and hydrogen content of powders can contribute to the good densification of SLM materials [103]. Therefore, the chemical composition design of the starting powders is the first step for their processing by SLM.

The shape factors, such as the distribution of the powder sizes and the sphericity, have a strong influence on the powder flowability [104]. The powders with high sphericity own a high flowability which leads to reduced defects and a higher relative density of SLM alloys [97,105]. Typically, the high solidification rate during the gas atomization can cause that gas atomized powders obtain a fine dendrite morphology [106]. Therefore, the powders with different sizes may lead to different microstructures. Moreover, the powder sizes can also affect the surface roughness and the mechanical properties of the SLM products [98,105].

1.2.3.2 Contours

As a typical example, Fig. 1.15 shows the morphology of the SLM Al-12Si alloy with contours. Typically, the design of the contour has a significant effect on the surface quality of the final products, improving the surface roughness and, consequently, the mechanical properties [57]. Therefore, the parameters (such as the scanning speed and the laser power) characterizing the contours should be selected carefully [107]. It should be mentioned that in order to match the processing of the volume and contour, the parameters for the contour offset should also be properly selected.

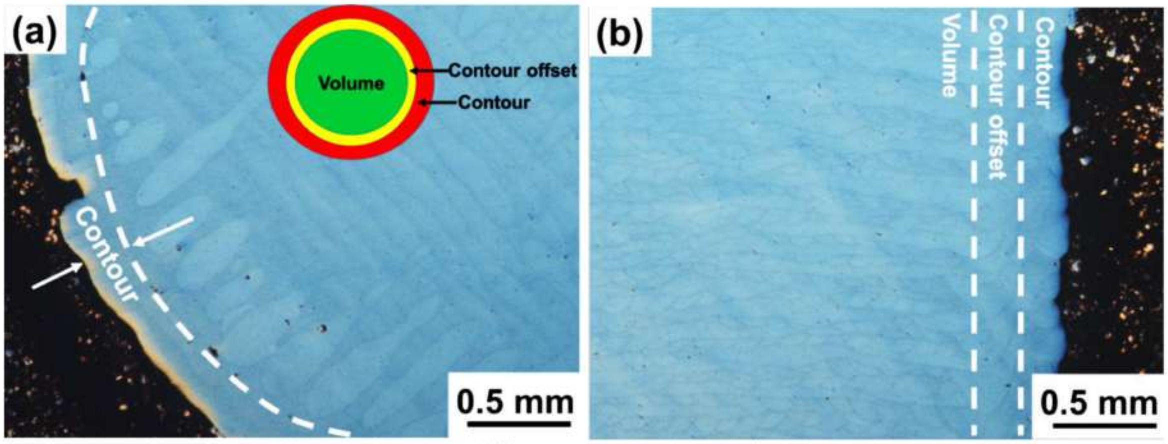

Figure 1.15 Schematic illustrating the different zones identified in a SLM sample: (a) scanning direction, (b) building direction.

1.2.3.3 Preheating and post-heating treatment

Due to the rapid solidification during SLM processing, high thermal residual stresses can be generated, which can lead to the distortion of the products and premature failure [108-110]. In order to avoid the defects resulting from the SLM processing, preheating and post-heating treatments method can be used to reduce the thermal stresses and microstructural stress concentrations [111]. Moreover, because the preheating method is to heat the powder bed at a certain temperature during SLM processing [111], this method (normally less than 473 K) also could decrease the formation of cracks and pores and further improve the surface quality of the samples [57,112]. Recently, with the development of new devices and in-depth research, more and more researchers utilize the preheating and post-heating methods to control the microstructure of alloys and optimize the mechanical properties [82,113,114].

1.2.4 SLM alloy systems

Due to the advantages of the flexible fabrication of parts with intricate shapes and the good performance of the SLM alloys with the non-equilibrium microstructures resulting from the rapid solidification, more and more researchers focus on the SLM technology and try to use it to produce different commercial alloys [115]. Moreover, in this decade, the business opportunities provided by the advantages of SLM cause that in the global scale, the industrial giants (e.g., General Electric Company (GE), Airbus S.A.S, Pratt & Whitney and Rolls-Royce Group plc) cooperating with the SLM companies (such as Concept Laser GmbH, SLM Solutions Group AG, Arcam AB and Renishaw) focus on the research and development of standardized SLM productions [5,22]. Nowadays, the SLM technology has been brought into almost all alloy systems.

Among the aluminum alloys, due to the excellent castability and weldability of the 4xxx and 6xxx series Al alloys, the Al-10Si-Mg and Al-12Si alloys are the most popular SLM Al alloys [39]. With the development of the SLM technology, the microstructure, solidification behavior, tensile properties, tribological properties, fatigue performance, fracture toughness and the corrosion behavior of the SLM Al-10Si-Mg and Al-12Si alloys have been investigated systematically and comprehensively [116-118]. Moreover, in order to further improve the physical/chemical properties of SLM Al alloys, composites based on Al-Si alloys have been developed successfully [119-121].]. Compared with the Al-Si alloys fabricated with conventional methods, the SLM Al-Si series alloys display high tensile strength, low wear rate and low coefficient of thermal expansion [119-121]. Therefore, more and more Al-Si series alloys (such as Al-7Si-Mg and Al-9Si-3Cu) were commercialized [122,123]. Recently, the processing drawbacks of SLM 2xxx and 7xxx series have been overcome by different methods (e.g., optimization of processing parameters, chemical composition of powders, and change of processing environment [46,112,124,125]) and these new heat treatable SLM Al alloys also display good mechanical properties in contrast to the corresponding Al alloys synthesized by conventional methods. The details about SLM alloys will be discussed further in the next section.

Ti-based materials are of a particular interest for biomedical, aeronautical and chemical applications due to their outstanding biocompatibility, appropriate mechanical properties and excellent corrosion resistance even at high temperatures [126-128]. However, due to the expensive price and the difficult shaping ability of Ti alloys, the components of Ti-based alloys with the complex geometry by conventional processing technologies (such as casting, forming and machining) will spend more money, time and energy than that of other common alloys (Fe alloys, Al alloys, and Cu alloys) [56,129,130]. Therefore, the advantages of the SLM processing for the fabrication of complex products attract the attention of the experts in the field of Ti alloys. Moreover, the high cooling rate during SLM processing results in the martensite microstructure and the formation of α' phase in SLM Ti alloys, leading to a higher tensile strength than Ti alloys processed by the conventional casting method [131]. As a result, the SLM Ti-6Al-4V, Ti-45Nb, Ti-5333 and Ti-6Al-7Nb alloys were developed and applied to the aviation, aerospace and clinical implant (like bracket connector, embedded cooling channels, and breastbone [22,131-135]). Recently, the new SLM Ti-47Al-2Cr-2Nb and Ti-45Al-2Cr-5Nb alloys which owns the better mechanical properties at higher temperature were developed [55,136]. In addition, some SLM Ti-based composites, such as TiB_2/Ti-6Al-4V, TiC/Ti, have also been fabricated successfully, which show a higher strength and lower specific wear rate than their matrix alloys [56,137-139].

Iron-based alloys, especially SLM 316L stainless steel, were researched and applied widely. Due to the fine cellular structure, the low-angle grain boundaries and the high dislocation density generated during SLM processing, SLM 316L stainless steel has the higher strength and low specific wear rate than conventional casting [140-142]. Based on the study on the SLM 316L stainless steel, new kinds of steels, such as FeCrMoVC tool steel [143], TRIP steel [144] and H13 high speed steel [145], were successfully developed and applied to the industrial production. All alloys show the good mechanical properties [146]. In order to improve the mechanical properties and wear performance further, the composites, such as TiB_2/H13 steel, TiB_2/316L stainless steel and TiC/316L stainless steel, also have been designed and synthesized successfully [145,147,148].

Due to the poor machinability of Ni-based superalloys, which have the ultra-strength, the good resistance to oxidation at high temperatures and the favorable weldability, the SLM technology has a significant advantage of their processing [149,150]. Therefore, in recent years, because of the wide application in the aeronautic and nuclear industries, SLM IN718 superalloy was investigated widely [151,152]. Moreover, due to the wide demand in the aerospace industry, the

SLM IN625 and IN 738LC with the good tensile and creep strength were also developed and applied in the heavy-duty gas turbines for hot gas path components such as the turbine blades and heat shields [153,154].

In recent years, some alloys, which were considered to be difficult to be processed by SLM in the past, have also be fabricated successfully. For example, due to the low laser absorption and high thermal conductivity requiring high powder input, SLM Cu-based alloys are difficult to be fabricated. However, recently, pure copper metal, Cu-10Sn alloy, Cu-Al-Ni-Mn alloy, Cu-4.3Sn alloy and Cu-15.5Zn-2.8Si alloy were produced successively [50,155-158]. In certain aspects, especially mechanical properties, these SLM Cu alloys display a good performance. In addition, owing to the low melting point and balling point of Mg and Zn elements, the successful fabrication of Mg-based and Zn-based alloys by SLM is still a problem. But some groups have already got involved into these difficult fields and got some exciting results. These researches not only provides an experimental foundation on Mg-based and Zn-based alloys but gives a guidance for the processing of alloys with high Mg and Zn contents, such as Al-Mg and Al-Zn series [159-161].

In addition, with further research on SLM processing, some special materials, such as brittle eutectic alloys [102,162], shape memory alloys [163,164], nanoparticle reinforced composites [138,165,166], functionally gradient materials [167,168], bulk metallic glass [11,64,92,93,169], high entropy alloy [170,171] and quasicrystal alloy [172], stepped into the vision of SLM scientists and engineers, and some of these materials also have been produced successfully.

2.2 SLM Al alloys and related materials

Aluminum alloys and their composites, most heavily consumed non-ferrous metal, play an important role in the industrial production and are applied to every aspect of the daily life. Every year, the industry uses up more than 24 million tons of Al alloys to meet the needs of mankind [173]. Because of the high specific strength and low cost, the Al alloys are used widely in the daily life (e.g., buildings, architecture, furniture, transport, heat exchanger and electrical conductors) [173,174]. It is conventional to divide the aluminum alloys into cast and wrought Al alloys, or heat-treatable and non-heat treatable Al alloys [175]. However, the category based on the main alloying element is the most simple and common way to classify Al alloys, as listed in Table 1.1 [175,176].

Table 1.1 Classification of aluminum alloys including their heat treatment, ultimate tensile strength (UTS) and applications. Adapted from Ref. [173,175]

Series	Main alloying elements	Heat treatment	UTS (MPa)	Applications
1xxx	≤1 % (non)	non-heat treatable	70 ~ 175	Electrical and chemical industries
2xxx	Cu	heat treatable	70 ~ 520	Aircraft structures, automotive
3xxx	Mg	non-heat treatable	140 ~ 280	Architectural application
4xxx	Si	non-heat treatable	105 ~ 350	Welding rods and brazing sheet
5xxx	Mn	non-heat treatable	140 ~ 380	Boat hulls, gangplanks, and marine products
6xxx	Mg and Si	heat treatable	150 ~ 380	Architectural extrusion and automotive components
7xxx	Zinc	heat treatable	380 ~ 620	aircraft structural components and other high-strength applications
8xxx	Others (Li, Sn)	heat treatable	280 ~ 560	Bearing application and connecting rod

Due to the widespread applications in the aerospace industry and the automotive industry, aluminum alloys became one of the earliest alloys fabricated by SLM technology, when the SLM market was quite new and small, leading to the high cost of the SLM products [177,178]. However, with the expansion of the market demand, more and more SLM aluminum parts are produced and applied, resulting in the decrease of the production costs [5,22].

1.3.1 SLM Al-Si series alloys

Due to the good castability and weldability of Al-Si series alloys during the laser processing, Al-Si alloys have been the first candidates fabricated by SLM [38,179]. Nowadays, SLM Al-Si series alloys are the most famous and abundant alloys in the family of SLM Al alloys and are applied successfully in aerospace and automotive sectors; examples are the vertical tail plane bracket, motorsports and aerospace interiors [5,37,38,180]. Especially, SLM processing of Al-12Si and Al-10Si-Mg alloys and their corresponding products have been standardized and commercialized in recent years [10,38]. The focus on these alloys has changed from the optimization of the processing parameters [59,177,181,182] to the analysis of the physical/chemical properties, such as fatigue, toughness, corrosion and thermal properties [57,91,120,167,183]. The results indicate that, owing to the fine cellular structure composed of nano-size eutectic Si, all Al-Si series alloys (such as SLM Al-12Si, Al-10Si-Mg and Al-50Si alloys) show a higher tensile strength but lower ductility than the corresponding cast alloys [57,119,182,184]. The high strength of the Al matrix with the dispersed nano-sized Si particles synergistically results in the high wear resistant of the SLM Al-Si series alloys [119]. Moreover, the supersaturates Si in the Al matrix of SLM Al-Si alloys can cause a decrease of the coefficient of thermal expansion (CTE) at low temperature in contrast to the cast alloys [120]. However, not all properties of the SLM Al-Si alloys are better than conventional Al-Si alloys. For example, the corrosion resistance of SLM Al-12Si is similar to the cast Al-12Si alloy [185]; the fatigue crack growth threshold and the unnotched fatigue strength of the SLM Al-12Si alloy are worse than the corresponding cast alloys [116]. Therefore, in the future, more properties of the SLM Al alloys and their corresponding conventional alloys should be compared to further understand the SLM processing.

1.3.2 SLM Al-Cu series alloys

Al-Cu series alloys are widely used in the aerospace industry due to their high specific strength, good fatigue properties and damage tolerance [186-188]. Most of the optimized properties of the Al-Cu alloys, such as high tensile strength and corrosion resistance, can only be obtained after post-processing (heat treatment, cold working, hot working and/or stretching) [173]. In order to shorten the post-processing steps and improve the physical/chemical properties, many suitable processing technologies have been applied to Al-Cu series alloys [39,187]. In the last few years, the research of SLM Al-Cu alloys focused on their densification [189-191], solidification principles [192] and mechanical properties [193]. The results suggest the SLM Al-Cu series alloys are difficult to be fabricated due to the effect of Cu on the solidification crack susceptibility [194,195]. It results in the crack generation during high cooling rates. Therefore, the synthesis of crack-free materials becomes the burning issue in the research of SLM Al-Cu alloys. In order to avoid the cracks generated during SLM processing, the optimization of the processing parameters and alloy composition become the main and effective methods to improve the product quality and mechanical properties. In fact, these methods have been successfully used for other series of Al alloy [101,196,197].

Al-Cu-Mg-Si alloys are an important kind of 2xxx series aluminum alloys. The different ratios of Cu, Mg and Si elements can result in different phase constitution (such as Q phase, Mg_2Si, Al_2Cu, Si and Al_2CuMg), leading to the diversity of physical/chemical properties [198-200]. Moreover, the addition of Si decreases the solidification crack susceptibility of Al alloys [124]. Therefore, the Al-3.5Cu-1.5Mg-1Si alloys fabricated by SLM were selected as the topic of my Ph.D. thesis, which will be discussed further in the subsequent chapters.

1.3.3 SLM Al-Zn series alloys

Al-Zn series alloys are the most popular Al alloys due to their high strength, relatively large ductility, good welding properties and corrosion resistance [201]. The processing of SLM Al-Zn alloys are more difficult than SLM Al-Cu alloys due to the serious vaporization of Zn and Mg during SLM processing [96,161]. The vaporization of Zn and Mg can result in the generating of cracks and pores, which limits the forming of SLM Al-Zn alloys [100] and leads to the disastrous decrease of their mechanical properties [100,112]. Some researchers try to use the different methods (e.g., the addition of alloy elements, parameter optimization and preheating) to avoid the generation of the defects [100,112,124,125]. Until now, the ideal method is to change the composition of Al-Zn series alloys to get the fine grains, which can result in the decrease of the thermal stress induced at the high cooling rate of SLM processing [124,202]. However, the change of the composition could remarkably affect the phase constitution and phase formation during SLM processing and subsequent heat treatment. The change of the phase constitution has a significant effect on the mechanical properties of these SLM Al-Zn alloys [124]. Therefore, the Al-Zn series alloys produced by SLM still will be a challenge in SLM Al alloys in next few years.

1.3.4 SLM Al-based composites

Aluminum Matrix Composites (AMCs) reinforced with ceramic particles are promising materials for structural applications due to their excellent combination of low density, high specific strength, good wear performance and high corrosion resistance [203,204]. Owing to the age-hardening capability, the heat-treatable aluminum alloys (e.g. 2xxx and 7xxx series alloys) with high strength are widely used in the aeronautics industry [198,199]. Therefore, heat-treatable AMCs have attracted significant attention for the development of high-strength lightweight materials with customized properties [205,206].

In addition, the demand of complex-shaped products in numerous industrial fields by the conventional fabrication methods of AMCs (e.g., powder metallurgy, stir casting, compo-casting and squeeze casting) is extremely difficult to meet [7,8]. Therefore, SLM also has the advantages of the fabrication of the AMCs with the complex geometry compared with composites fabricated by conventional methods [145,207,208]. With the application of SLM in the fabrication Al-Si series alloys described in Section 1.3.1, SLM paved a new way for the design and fabrication of Al-12Si and Al-10Si-Mg composites ((e.g., SiC/Al-10Si-Mg [45], carbon/Al-10Si-Mg [209], TiC/Al-10Si-Mg [166], TNM/Al-12Si [207] and TiB_2/Al-10Si-Mg [165]). All these SLM AMCs exhibit better mechanical properties than the corresponding SLM unreinforced alloys.

Recently, crack formation (the major processing bottlenecks related to SLM processing of heat-treatable Al alloys) was overcome and, thus, some defect-free heat-treatable Al alloys were successfully fabricated by SLM as described in Section 1.3.2 [46,210]. In order to eliminate the evolution of defects upon SLM processing and to further improve the mechanical properties, Zr/Al-Cu, Zr/Al-Zn and Si/Al-Zn alloys were produced by SLM of powder mixtures [101,124,202]. It was reported that the addition of these alloying elements (Zr and Si) results in grain refinement and elimination of cracks, which is obviously of great benefit for the improvement of the mechanical properties [101,124,202]. Simultaneously, reactions between the alloying elements and the matrix alloy can lead to the formation of brittle intermetallic phases [101,202]. Unfortunately, these reactions also result in a change of the chemical/physical properties of the matrix and, thus, a remarkably different phase transformations, especially in the course of the heat treatment [124,202]. This clearly indicates that the design of heat-treatable SLM AMCs has to be done carefully to avoid any composition related drawbacks.

Generally, due to the high melting temperatures (> 2000 K) achieved during SLM processing, the introduced reinforcement can affect the Al matrix significantly according to the supersaturation and the possible reaction between matrix and reinforcement [45,165,166,209]. Therefore, the composite design has to be carefully designed. Most of these reinforcement can improve the mechanical properties and wear resistant of SLM Al alloys dramatically [165,166,207]. But some of them are still not favorable to the processing of the fully dense SLM Al-based composites and result in the deterioration of properties, as shown in Fig. 1.16.

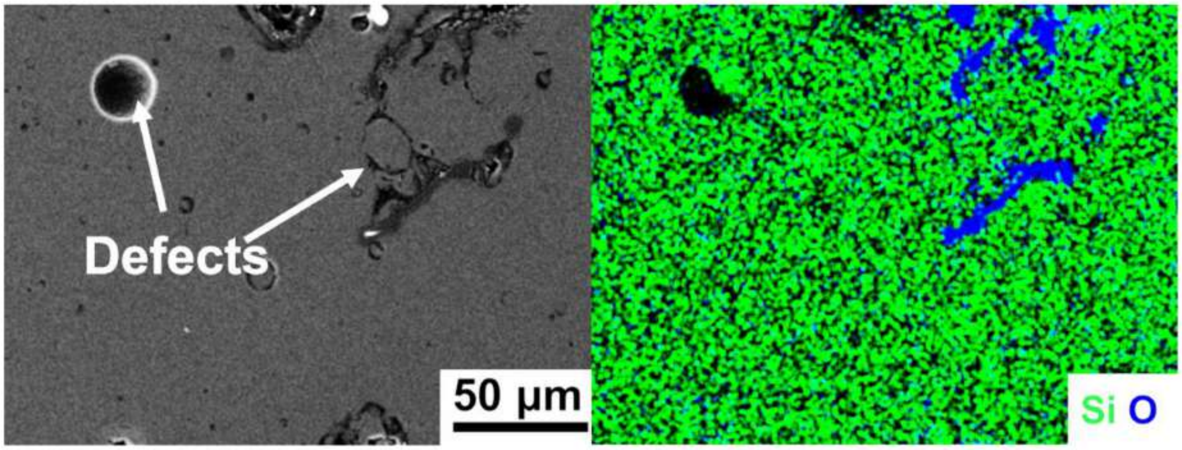

Figure 1.16 SEM images and corresponding EDS map of Al_2O_3/Al-12Si composites fabricated by selective laser melting.

As mentioned above, the inappropriate reaction between the reinforcement and matrix can change the phase constitution of the composites and result in the deterioration of the physical/chemical properties. Therefore, the selection of the reinforcement for heat treatable Al alloys is more critical than in Al-Si series alloys.

Due to the good wettability between TiB_2 and Al alloys, the good physical properties of TiB_2 at high temperature and its pronounced effect as grain refiner for Al alloys [211,212], TiB_2 is an ideal choice as reinforcement in AMCs. In addition, TiB_2 exhibits a good chemical stability and low solubility in Al alloys, which may avoid or reduce undesirable reactions between the TiB_2 reinforcements and the Al matrix [211,213]. In order to synthesize heat-treatable AMCs by SLM, the choice of a suitable heat-treatable matrix is a necessary prerequisite. Therefore, in the thesis (Section 5.2), the heat treatable Al-3.5Cu-1.5Mg-1Si alloy was selected as the matrix for the production by SLM of novel heat-treatable TiB_2/Al-Cu-Mg-Si composites.

1.3.5 SLM Al-based hybrids

Although Al-Cu series alloys are widely used in the aerospace sector due to their high strength and fracture toughness, good damage tolerance and good resistance to fatigue crack propagation as described in Section 1.3.2 [186,214], some drawbacks of 2xxx series, such as poor weldability and low corrosion and wear resistance, limit their application in many fields [215,216]. In order to overcome their drawbacks and adapt these alloys to the critical working conditions, a number of dissimilar materials of different series aluminum alloys (such as AA2024/AA7075, AA2024/AA6056 and AA2024/AA4043 hybrid alloys) were designed and applied to aerospace and non-aerospace sectors (e.g. aluminum vessels for the marine applications, fasteners, suspension parts and seat components in the automotive industry) [216-219]. Due to the low coefficient of thermal expansion (CTE) and superior tribological properties of Al-Si alloys [185,220,221] and the excellent mechanical properties of Al-Cu-Mg-Si alloys [198,222], dissimilar materials of these two materials have attracted much attention in the aerospace and marine industry [216, 219, 223]. Moreover, in order to meet the demand of the low energy consumption, advanced technologies are expected to fabricate the hybrid alloys with extremely complex geometries [167,224].

Due to the reduced need for post-machining and the improved properties of the SLM parts [57,185,210], hybrid alloys synthesized by SLM would have remarkable advantages compared to hybrid alloys fabricated by conventional welding technologies, such as friction stir welding, laser welding and metal inert gas welding [216,225]. Recently, Bartkowiak *et al.* forecasted the feasibility and good economic benefits of SLM Al hybrid materials [177]. Unfortunately, only limited attention has been paid until now to the generation of dissimilar materials by additive manufacturing [31,226], especially selective laser melting [167]. Therefore, in this Thesis, an Al-12Si/Al-3.5Cu-1.5Mg-1Si hybrid alloy was designed and fabricated by selective laser melting.

CHAPTER 2

Synthesis and characterization methods

The present chapter provides the preparation information of various samples and the characterization techniques used in this thesis. Firstly, an extensive insight on the experimental details of the SLM process and powder mixtures are given here. In order to investigate the effect of heat treatment, the conventional T6 heat treatment is designed and described in detail. This is followed by the methods used for the phase analysis, the microstructural characterization, and the mechanical, tribological and corrosion tests.

2.1 Sample preparation

2.1.1 Selective laser melting

Gas-atomized Al-3.5Cu-1.5Mg-1Si powders (powder size: 20-60 µm; d_{50} of the powders: 41 ± 1 µm) were supplied by the TLS Technik GmbH & Co. Spezialpulver KG, and were used as starting materials for the SLM processing. In order to compare the properties of different SLM Al alloys, Al-12Si powders (powder size: 20-60 µm) and Al-4.5Cu powders (powder size: 20-60 µm), are also used to fabricate SLM specimens. Also, the AA2024 alloy O is supplied by the Harbin Institute of Technology as a reference material. With the help of Andrea Voß at IFW Dresden, the composition of all materials mentioned above was investigated using ICP-OES (Inductively Coupled Plasma-Optical Emission Spectroscopy) and is shown in Table 2.1.

Table 2.1 Chemical composition of the powder materials.

Element (wt. %)	Cu	Mg	Si	Mn	Al
Al-3.5Cu-1.5Mg-1Si powder	3.56 ± 0.03	1.45 ± 0.01	1.12 ± 0.01	0.62 ± 0.01	balance
AA2024 alloy O	4.06 ± 0.01	1.36 ± 0.01	0.18 ± 0.01	0.57 ± 0.01	balance
Al-4.5Cu powder	4.47 ± 0.01	< 0.10	0.24 ± 0.01	< 0.01	balance
Al-12Si powder	< 0.10	< 0.10	11.78 ± 0.15	< 0.10	balance

An SLM 250^{HL} system (SLM Solutions Group AG) was used to prepare the samples, as shown in Fig. 2.1. The system is equipped with a 400 W Nd: YAG laser (continuous wave) and a beam diameter of 80 μm. All SLM specimens were fabricated on an Al-10Si-Mg substrate. All SLM processing was done under protective argon atmosphere (purity 99.999 %). The oxygen content in the SLM chamber was below 0.02 vol. % during the complete processing time.

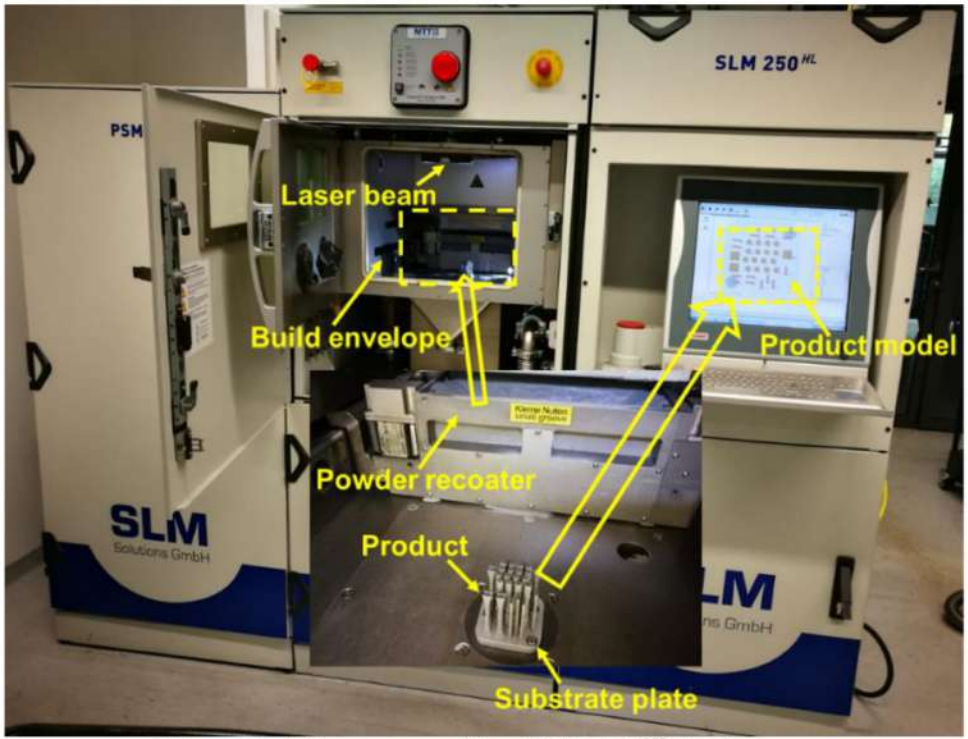

Figure 2.1 Overview of the SLM 250^{HL} device.

The parameter optimization was carried out to fabricate the SLM Al-3.5Cu-1.5Mg-1Si alloy using the following parameters: the laser power was varied between 100 and 330 W, the laser scanning speed between 160 and 1500 mm/s, the hatch spacing between 0.07 and 0.11 mm, and the layer thickness between 0.04 and 0.06 mm. With numerous work about the parameter optimization, the parameters (power input of 190 W, scanning speed of 165 mm/s, hatch spacing of 0.08 mm and layer thickness of 0.04 mm) are selected to fabricate the specimens for the analysis. The details about the parameter optimization will be described in Chapter 3.

In Chapter 5, the optimized parameters for the SLM Al-3.5Cu-1.5M-1Si alloy are used to fabricate the Al-xCu alloys (x = 4.5, 6, 20, 33 and 40 wt. %), TiB_2/Al-3.5Cu-1.5M-1Si composite and the Al-3.5Cu-1.5M-1Si part of Al-12Si/Al-3.5Cu-1.5M-1Si hybrid alloy. In the thesis, an SLM

Al-12Si alloy was synthesized using the following optimized parameters: power input of 320 W, scanning speed of 1455 mm/s, hatch spacing of 0.11 mm and layer thickness of 0.05 mm [184].

Due to the complex preparation for the fabrication of Al-12Si/Al-3.5Cu-1.5M-1Si hybrid alloy, the detailed procedure is described as follows:

Firstly, cylindrical rods of Al-12Si parts (Ø15 mm × 27 mm) were fabricated by selective laser melting. After the fabrication of Al-12Si rods, the residual Al-12Si powder in the device was removed, and the building chamber and the recoater were cleaned carefully. The SLM Al-12Si parts built on the Al-10Si-Mg substrate were moved out from the workbench and then the top surfaces of the Al-12Si parts were grinded by P400 sandpaper. Adhering particles on the surfaces of the Al-12Si parts were removed by sandblasting and the SLM parts were cleaned with ethanol (purity 99.5 %). The cleaned Al-10Si-Mg substrate with SLM Al-12Si parts was fixed back on the workbench. Al-3.5Cu-1.5Mg-1Si powders were refilled into the cleaned recoater and the space around the SLM Al-12Si parts, and then the first layer of Al-Cu-Mg-Si powders on the top surfaces of the Al-12Si parts was prepared carefully. Cylindrical rods (Ø4.5 mm × 27 mm) and rectangular cuboid parts (4.5 mm × 4.5 mm × 27 mm) of Al-Cu-Mg-Si alloy were simultaneously fabricated on the SLM Al-12Si parts by selective laser melting with optimized parameters. Moreover, considering the influence of the processing parameters used for the fabrication of the Al-Cu-Mg-Si alloy on the hardness and microstructure of the top layers of the Al-12Si parts at the interface, additional reference Al-12Si specimens (hereafter termed Ref-Al-12Si), were prepared with the parameters used for the synthesis of the Al-Cu-Mg-Si parts (power input of 190 W, scanning speed of 165 mm/s, hatch spacing of 0.08 mm and layer thickness of 0.04 mm).

2.1.2 Powder mixtures

The Al-xCu powder mixtures (x = 4.5, 6, 20, 33 and 40 wt. %) were obtained by mixing Al-4.5Cu powders with copper powder (powder sizes < 63 μm) under protective argon atmosphere by using a drum hoop mixer (JEL RRM Mini-II as shown in Fig. 2.2) for 30 min at a speed of 30 rounds per minute (RPM). The TiB_2 powders (d_{50} = 3 ± 0.5 μm) and Al-3.5Cu-1.5Mg-1Si powders were also mixed under the same condition with the same mixture parameters.

Figure 2.2 Photograph of the drum hoop mixer.

2.1.3 Heat treatment

The heat treatment was carried out by Siegfried Neumann and Juliane Scheiter at IFW Dresden. The specimens were heat treated in a FRH-3-40-500-1100 furnace provided by Linn High Therm. Company. All samples were put in a glass tube before heat treatment. The interior of the glass tube was continuously flowed with Ar gas to prevent the oxidation of the samples. In order to analyze the effect of the conventional heat treatment on the performance of the SLM Al-Cu-Mg-Si alloy and Al-Cu-Mg-Si-based composites, the T6 heat treatment condition [227] was selected and its schematic is drawn in Fig. 2.3. The SLM Al-Cu-Mg-Si alloy, SLM TiB_2/Al-3.5Cu-1.5M-1Si composite and AA2024 alloy O were solution treated at 793 K for 1 h, water quenched, and then subjected to aging at 463 K for 10 h followed by air cooling. The specimens subjected to T6 heat treatment are termed T6.

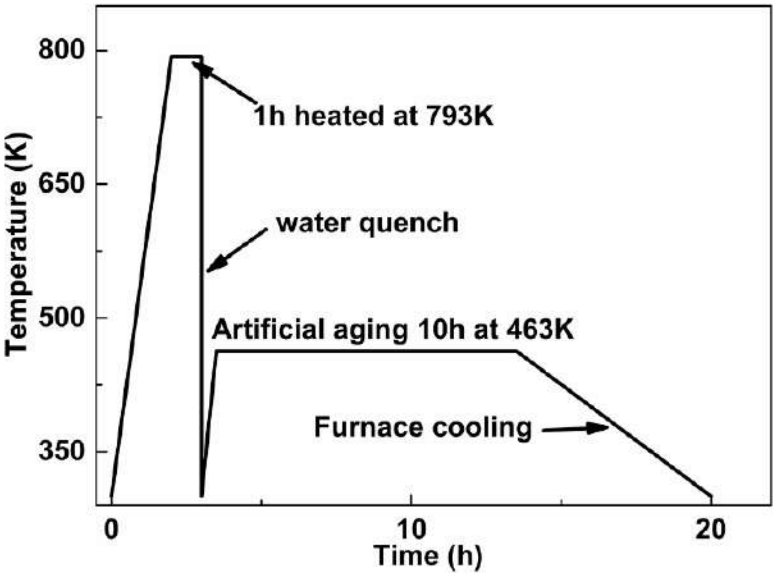

Figure 2.3 Schematic of the T6 heat treatment.

2.2 X-ray diffraction

Phase and structural analysis was performed by X-ray diffraction (XRD; D3290 PANalytical X'pert PRO, Co-K_{α} radiation (λ= 0.178897 Å)) in reflection mode. In order to maintain the uniformity in the height of the samples, the bulk samples were grinded to 0.8 ± 0.1 mm. The patterns were measured between 2θ = 20 ° and 120 ° with a step size of $\Delta(2\theta)$ = 0.013 ° and 2 s acquisition time per step. The diffractometer operated at a voltage of 40 kV and a current of 40 mA.

2.3 Microscopy

2.3.1 Optical microscopy (OM)

Optical microscopy was carried out by using a VHX-2000 digital microscope (OM; Keyence). The microscope can observe the samples from 5× to 1000× magnification using different objective lenses. The device is equipped with a built-in camera which is connected to the VHX software, so that the figures can be recorded and analyzed directly. The samples were embedded in a conductive resin at room temperature to avoid the artificial aging and grinded using a Struers Rotopol with the grinding papers as the following sequence: P240→P600→P1200→P2500→P4000. The grinded samples were polished with 3 µm diamond suspensions for 4 min and 0.25 µm diamond suspensions for 2 min. some of the specimens were etched by using Keller's reagent (47.5 mL H_2O, 1.25 mL HNO_3, 0.75mL HCl and 0.5mL HF) for 9 s dwell time.

2.3.2 Scanning electron microscopy (SEM)

The microstructures were characterized by a high-resolution scanning electron microscopy (SEM; Gemini LEO 1530 microscope). The SEM is equipped with an energy-dispersive X-ray spectroscopy system (EDS; Quantax400 with SDD-Detector Xflash4010, Bruker) for element analysis and electron backscatter diffraction (EBSD; CrystAlign, Bruker). Based on the imaging principles of scanning electron microscopy, back scattered electrons mode (BSE) and secondary electrons mode (SE) were used to observe the microstructure. The BSE mode was used to distinguish the matrix and phases, and the SE mode was used to observe the fracture morphology, worn surfaces and corroded surfaces. The operating parameters for the observations are: 15-20 kV voltage, 10 mm working distance and 60-120 µm aperture, i.e. a beam current of about 7 nA. In order to get the better polishing surface and analyze the information of the texture and grains, after the polishing step described in Section 2.3.1, the specimens for EBSD measurement were not etched but polished further for 10 h using a VibroMet^{TM} 2 Vibratory Polisher (Buehler GmbH). Depending on the polishing quality, the high quality surface was observed by SEM with EDS and EBSD equipment. For the EBSD measurement, to eliminate spurious boundaries caused by the orientation noise, the boundaries with misorientation angles lower than 1 ° were removed. A misorientation criterion of 15 ° was employed to differentiate between low-angle boundaries and high-angle boundaries [228]. The minimum grain size was selected as 5 µm at low magnification and 0.5 µm at high magnification; both values roughly represent 2 times the scan step (2.4 µm at low magnification and 0.24 µm at high magnification, respectively). The average equivalent grain sizes were counted by Tango software in the Channel 5 software package. Each counted area included at least 500 grains. Especially, for the EBSD measurement of the Al-12Si/Al-Cu-Mg-Si hybrid alloy, in order to ensure the accuracy, the average grain sizes per 0.1 mm from the interface along the building direction were counted using the linear intercept method of Tango software, and the number of the intercepted lines in each 0.1 mm area is set to be 5. The estimate of the uncertainty of all grain detection and size calculation is 10 %.

2.3.3 Transmission electron microscopy (TEM)

The TEM samples were firstly cut into slices with a thickness of about 0.5 mm from the bulk materials (4 mm × 4 mm × 8 mm). A mechanical grinding, down to 80 μm thickness, was done by using sandpapers (P1200→P2500→P4000). The samples were further grinded with a 1 μm suspension and polished with a 0.25 μm suspension to about 15-20 μm by using the Gatan 656 dimple-grinder. In order to obtain the final transparent area, with the help of Dina Bieberstein at IFW Dresden, Germany, Precision Ion Polishing system (PIPS, Gatan Model 691) was used to mill each surfaces of samples using an ion beam energy of 3 kV at a rotation angle of 5 ° for above 3-4 h.

The prepared TEM samples were investigated by Dr. Christoph Gammer at Erich Schmidt institute, Austria, by using a Philips CM12 transmission electron microscope (TEM) at an acceleration voltage of 120 kV. Bright-field images and selected area electron diffraction (SAED) patterns were recorded to analyze the phase distribution and microstructure. The TEM was equipped with an EDAX detector allowing to quantify the chemical composition of the precipitates.

2.4 Physical and chemical characterization

2.4.1 Density

The density of the specimens was measured by the Archimedes method using a Sartorius density measuring set YDK-01 (0D). The samples were weighed in air firstly, then immersed into the distill water for a few seconds before they were weighted again. The relative density was calculated by dividing the measured density by the theoretical density, which was calculated from the composition. The samples with the high relative density (≥ 99.00 %) were defined as the bulk materials, which are used for the physical and chemical characterization.

2.4.2 Microhardness

Vickers microhardness tests were performed using a HMV Shimadzu microhardness tester with 0.05 kg load and 10 s dwell time. The data of all specimens was averaged over at least 20 different points, which were selected automatically. For the interface of the Al-12Si/Al-Cu-Mg-Si hybrid alloy, the data shown were averages of at least five different points at the same distance from the interface. The measurement uncertainty of the HMV Shimadzu microhardness tester is 2 $HV_{0.05}$.

2.4.3 Compression and tensile test

Compressive and tensile tests both were carried out at room temperature using an Instron 5869 machine. The cylindrical specimens (Ø 3 × 6 mm) for compression were test at a fixed cross-head speed of 0.001 mm/s following the standard DIN 50106 [56].

The dimensions of the cylindrical samples used for tensile tests was $d_0 = 3.5$ mm (gauge length), $d_1 = 4$ mm, $L_0 = 17.5$ mm, $L_c = 21$ mm, $h \geq 13$ mm and $L_t = 52$ mm according to the ASTM E8/E8M-13a standard. The tests were carried out under quasi-static loading (strain rate 1×10^{-4} s^{-1}). The axial strain during the tensile and compressive tests was measured directly on the specimens using a Fiedler laser-extensometer. The mechanical property data shown in this thesis are values averaged over three specimens to ensure the reproducibility of the results.

The Al-Cu-Mg-Si specimens with the corresponding optimized parameters, the Al-12Si specimens with the corresponding optimized parameters and Al-12Si/Al-Cu-Mg-Si hybrid alloys were fabricated as a cylinder rod (Ø5 × 54 mm) and machined to the final shape for the tensile text. The surface quality of the machined samples fulfills the demand for the tensile test.

All mechanical tests were carried out along the building direction.

2.4.4 Sliding wear test

Sliding wear tests were carried out by pin-on-disk with a Tribometer (T500, Nanovea) at room temperature according to DIN EN 1071-13 [229] with the help of Alexander Schultze. In order to control the temperature, the temperature was detected during the measurement, which was stabilized in the range of 313-323 K. The pin-samples made from the tested alloys (Ø6 mm× 30 mm) and an X210Cr12 steel grinding disk were performed as shown in Fig 2.4. Before the wear tests, the samples were grinded by SiC grinding paper with a final finish of 1200 grit (P4000).

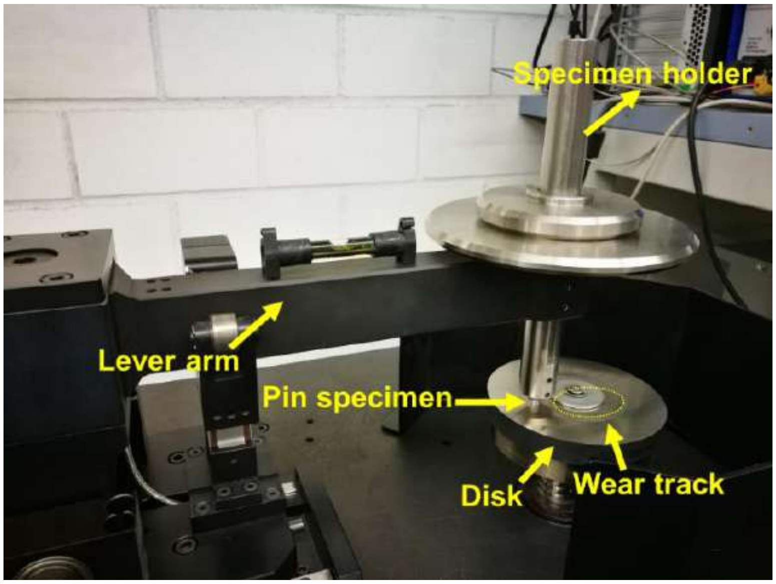

Figure 2.4 Photograph of the pin-on-disk wear test.

According to DIN EN 1071-13 the specific wear rate k was calculated as follows:

$$k = \frac{V}{F_N L} \ , \tag{2.1}$$

A normal load F_N of 15 N was applied on the lever arm during the measurement as shown in Fig. 2.4. The sliding distance is given by $L = 2\pi rvt$, where r is the radius of the wear track (30 mm), v is the rotating speed of disk (400 RPM) and t is the sliding time (60 min). According to the calculation the sliding distance (L) is 4521 mm. The wear volume V was hereby determined for every tested sample by $V = (m_0 - m)/\rho$, whereby m_0 is the mass of the pin specimens before the wear test and m the mass after testing.

In addition, the average value of the coefficient of friction (COF) was measured using a separate load system in contact with the continuous lever arm and recorded by Nanovea Tribometer system.

All data (specific wear rate and average COF) shown are averages of at least three different measurements.

2.4.5 Corrosion test

For electrochemical corrosion analysis, with the help of Dr. Annett Gebert and Marion Johne at IFW Dresden, Germany, polarization tests were carried out by using a standard three-electrode cell with the test material as working electrode, a saturated calomel electrode (SCE, E = 0.241 V versus SHE) as reference electrode and a Pt net as counter electrode. The cell was connected to a Solartron SI1287 electrochemical interface to control the measurement and to record the data. All tests were carried out in a 0.1 M NaCl solution with pH = 7 under ambient atmosphere (after de-aeration of the electrolyte by nitrogen purging). As working electrodes cylindrical samples (Ø3 × 15 mm) were electrically contacted and embedded in epoxy resin for electrochemical measurements and microstructural observation. The cross-sectional area of the samples was used as electrode surface. Prior to immersion in the electrolyte, the samples were grinded with emery paper up to P4000. Before the start of the potentiodynamic polarization tests, the samples were maintained at open circuit conditions for 30 min, while their open circuit potential (OCP) was monitored. To study the free corrosion, passivation, pitting and repassivation behavior, the samples were slowly polarized with a potential scan-rate of 0.5 mV/s. The measurement started from a cathodic potential (-100 mV more negative than the final OCP) and the potential was swept in positive direction up to the pitting region, which was characterized by a steep increase of the anodic current density. When the measured current density reached a defined value of 1 mA/cm^2, the polarization direction was reversed and the measurement was stopped after the second minimum. The corrosion parameters (e.g., corrosion potential E_{corr}, corrosion current density i_{corr}, pitting potential E_p and repassivation potential E_{re}) were determined by means of graphical extrapolations. An example curve analysis will be shown in Chapter 4 (Fig. 4.5(a)). For each material, 3-5 repeated polarization tests were conducted and one representative curve for one material was selected to determine the corrosion data.

After selected polarization tests, the corroded sample cross-sections were examined by scanning electron microscopy (SEM) and energy dispersive x-ray spectroscopy (EDS).

CHAPTER 3

Processing and characterization of SLM Al-Cu-Mg-Si alloy

The present chapter deals with the densification and characterization of a heat-treatable Al-3.5Cu-1.5Mg-1Si alloy fabricated by selective laser melting. Due to the significance of the powder characteristics on the SLM processing, the powder was analyzed in detail firstly. Then, an extensive insight on the parameter optimization of the Al-Cu-Mg-Si alloy and the relationship between parameters, defects and relative density were investigated. Furthermore, the phase analysis, microstructure and mechanical properties of the SLM Al-Cu-Mg-Si alloys was elaborated. Moreover, the effect of T6 heat treatment on the microstructure and mechanical properties of the SLM Al-Cu-Mg-Si alloy were systematically discussed by analyzing the grain size, the texture and the phase constitution. Finally, the strengthening mechanism of the SLM Al-Cu-Mg-Si alloy was analyzed depending on the fracture morphology.

3.1 Powder analysis

Fig. 3.1(a) depicts the information of the starting gas-atomized Al-3.5Cu-1.5Mg-1Si powders used for the SLM processing, which is important to set the initial value of hatch spacing (l_{hs}) and layer thickness (l_z). The size of powders mainly distributes from 40 to 50 µm. Fig. 3.1(b) shows the morphologies of the starting Al-Cu-Mg-Si powders. Small satellites are visible around the spherical Al-Cu-Mg-Si powders (Fig. 3.1(b)). The presence of satellites is a common phenomenon resulting from gas atomization. In general, the presence of satellites and powder clusters are detrimental for the flowability of the powders and their densification by SLM [230,231]. But the optimization of the processing parameters can eliminate this adverse effect [182,232]. The adhesive interface between the two particles at high magnification (the inset in Fig. 3.1(b)) suggests that the powder adhesion phenomenon happens during the solidification of the droplets. These powder adhesion and cluster can hinder the movement of the powder, which can negatively affect their flowability when the powder spread out the Al-10Mg-Si substrate. However, the high specific surface area of the small powders can result in high energy absorptivity of Al powder for the laser beam, which is good for the melting of Al powders during SLM processing [233].

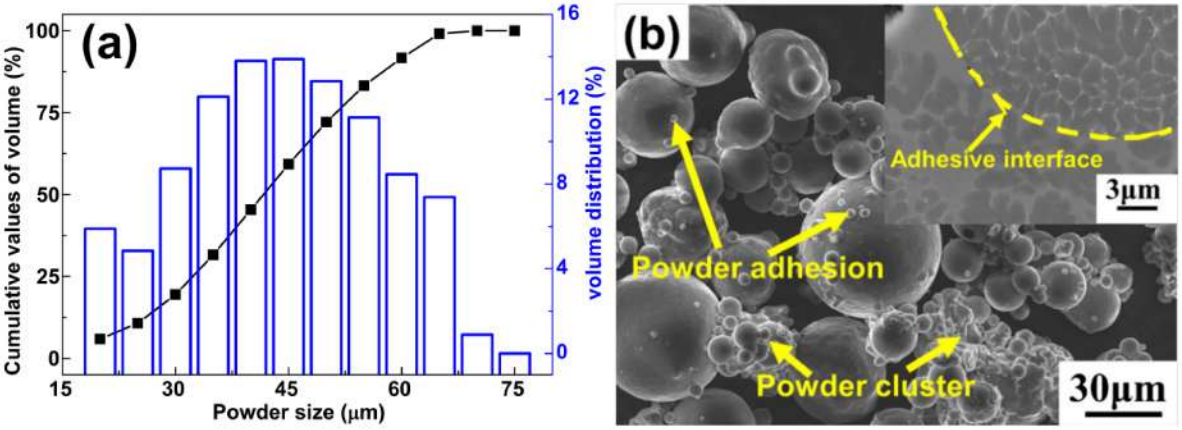

Figure 3.1 (a) the distribution of the powder size; (b) typical morphologies of the starting Al-3.5Cu-1.5Mg-1Si powders (inset: cross-section).

3.2 Parameter optimization and densification

Due to the size distribution of the as-atomized powder (Fig. 3.1), the initial values of the hatch space (l_{hs}) and the layer thickness (l_z) were selected to 0.11 mm and 0.05mm, respectively. Fig. 3.2 shows the relationship between the relative density of the samples and the employed scanning speed (v_s) and laser power (P) for processing with l_{hs} = 0.11 mm and l_z = 0.05 mm. The contour map suggests that low laser power ($P \leq 250$ W) and slow scanning speed ($V \leq 250$ mm/s) are beneficial for obtaining near-fully dense Al-3.5Cu-1.5Mg-1Si specimens (relative density ≥ 98 %). Processing at constant volumetric energy density (black dashed lines in Fig. 3.2) leads to considerable variations of density, which further indicates that materials synthesis by SLM cannot rely on predictions exclusively based on the energy density, as recently reported by Pauly *et al.* [92]. In order to further analyze the effect of the processing parameters on the relative density of the specimens, samples synthesized at constant laser power of 320 W (green points along the gray dashed line in Fig. 3.2) and at constant volumetric energy density of 182 J/mm^3 (green points along the black dashed line marked E_V = 182 J/mm^3) have been investigated by SEM and the results are shown in Figs. 3.3 and 3.4, respectively. It should be mentioned that the volumetric energy density is calculated by equation 1.1 (mentioned in Section 1.2.1).

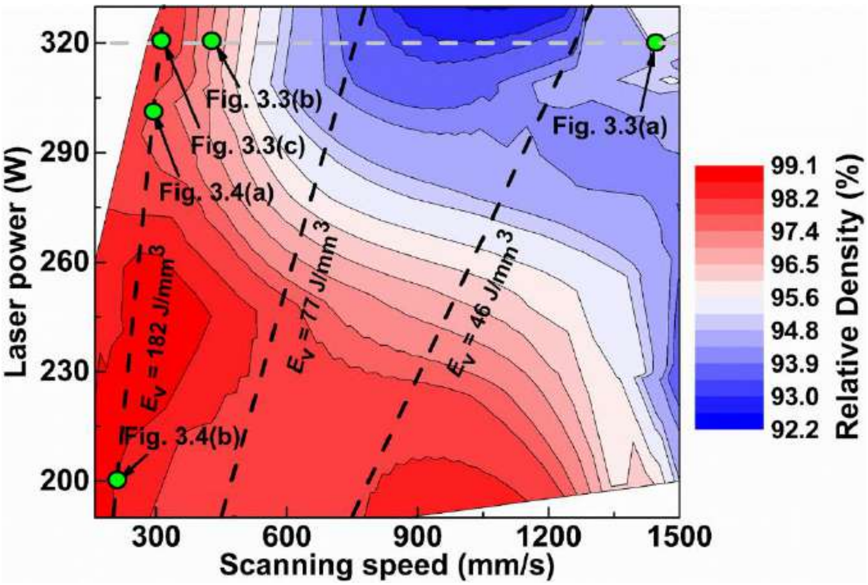

Figure 3.2 Contour map of the relative density of the SLM Al-3.5Cu-1.5Mg-1Si specimens as a function of scanning speed and laser power for processing with l_{hs} = 0.11 mm and l_z = 0.05 mm.

Fig. 3.3 displays the SEM micrographs of the samples subjected to different scanning speeds for processing at constant P, l_{hs} and l_z. The microstructure of the samples built with the fastest scanning speed (Fig. 3.3(a)), reveals the formation of cracks along the building direction. It is well-known that the rapidly cooled Al-based alloys with high contents of Cu and Mg are susceptible to cracks [64,194,195], since the cooling rates during SLM processing are considerably high (10^3-10^6 K/s) [65,66], which in turn may induce large degrees of supersaturation and consequently brittleness of the SLM parts. This may explain why using the same processing parameters, the SLM Al-3.5Cu-1.5Mg-1Si alloy shows cracks and the SLM Al-12Si alloy does not [184]. The quantity of cracks decreases with decreasing scanning speed (Fig. 3.3(b)). Below v_s = 320 mm/s, there are fewer cracks which are difficult to be clearly observed (Fig. 3.3(c)). According to the Equation 1.1, the reduced scanning speed results in an increase of the volumetric energy density (E_V), which has a positive correlation with the temperature in the molten zone [89,234]. Typically, a high E_V can lead to a temperature increase in the molten zone reducing the transverse stress, which can then reduce the formation of the solidification cracks [195,235]. Therefore, low scanning speeds can eliminate cracks in the Al-3.5Cu-1.5Mg-1Si alloy fabricated by SLM. Unfortunately, there are significantly more pores formed in the specimens produced at low scanning speeds (Fig. 3.3(b) and Fig. 3.3(c)); because of these pores, the relative density of the specimens cannot be improved further.

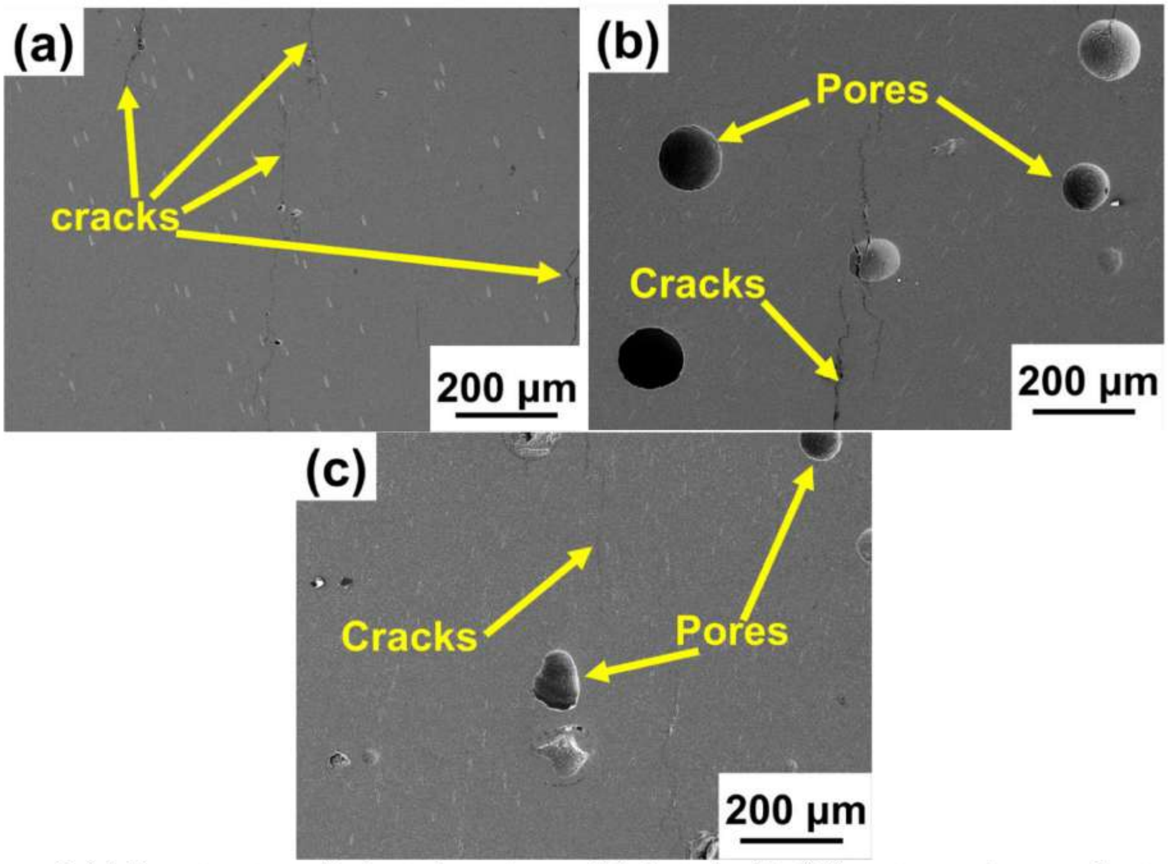

Figure 3.3 Microstructure of selected specimens fabricated with different scanning speeds at constant laser power (P = 320 W), hatch spacing (l_{hs} = 0.11 mm) and the layer thickness (l_z = 0.05 mm): (a) v_s = 1455 mm/s, (b) v_s = 450 mm/s and (c) 320 mm/s.

In order to investigate the quality of the laser track and scanning parameters for 316L stainless steel and Inox 904L stainless steel, Yadroitsev *et al*. performed experiments where the multi-layers were repeatedly heated with a single laser track with different power and scanning speed [236,237]. They found that in the processing of multi-layers with the same P/v_s ratio, the layers subjected to the low power and low scanning speed display a more continuous and stable track than multi-layers processed with higher laser power and high scanning speed [236,237]. Recently, Bertoli *et al*. also reported the same phenomenon for 316L stainless steel, where the single track changes from the continuous regime to the irregular and balling regimes with synchronously increasing laser power and scanning speed [49]. In order to reduce the formation of defects (mainly cracks and pores) and for obtaining nearly full dense materials, we processed the Al-3.5Cu-1.5Mg-1Si alloy at a constant P/v_s ratio (Figs. 3.4(a) and (b)). In contrast to the microstructure in Fig. 3.4(a), the pores in the specimens with low power and low scanning speed (Fig. 3.4(b)) decrease significantly and the relative density of these samples is about 98.9 ± 0.1 %, in agreement with previous other works reporting that the pores formed at high power and high scanning speed possibly result from the irregular and balling phenomena of the laser tracks [40-42]. As shown in Fig. 3.4(b), there are still irregular defects and unmolten powder particles in the specimens. In order to avoid the formation of these irregular defects and increase the relative density further, the hatch spacing and layer thickness were adjusted and the optimized parameters (P = 190 W, v_s = 165 mm/s, l_{hs} = 0.08 mm, and l_z = 0.04 mm) were selected to process fully dense Al-3.5Cu-1.5Mg-1Si specimens. The relative density of these optimized Al-3.5Cu-1.5Mg-1Si samples is 99.1 ± 0.1 % (Fig. 3.4(c)).

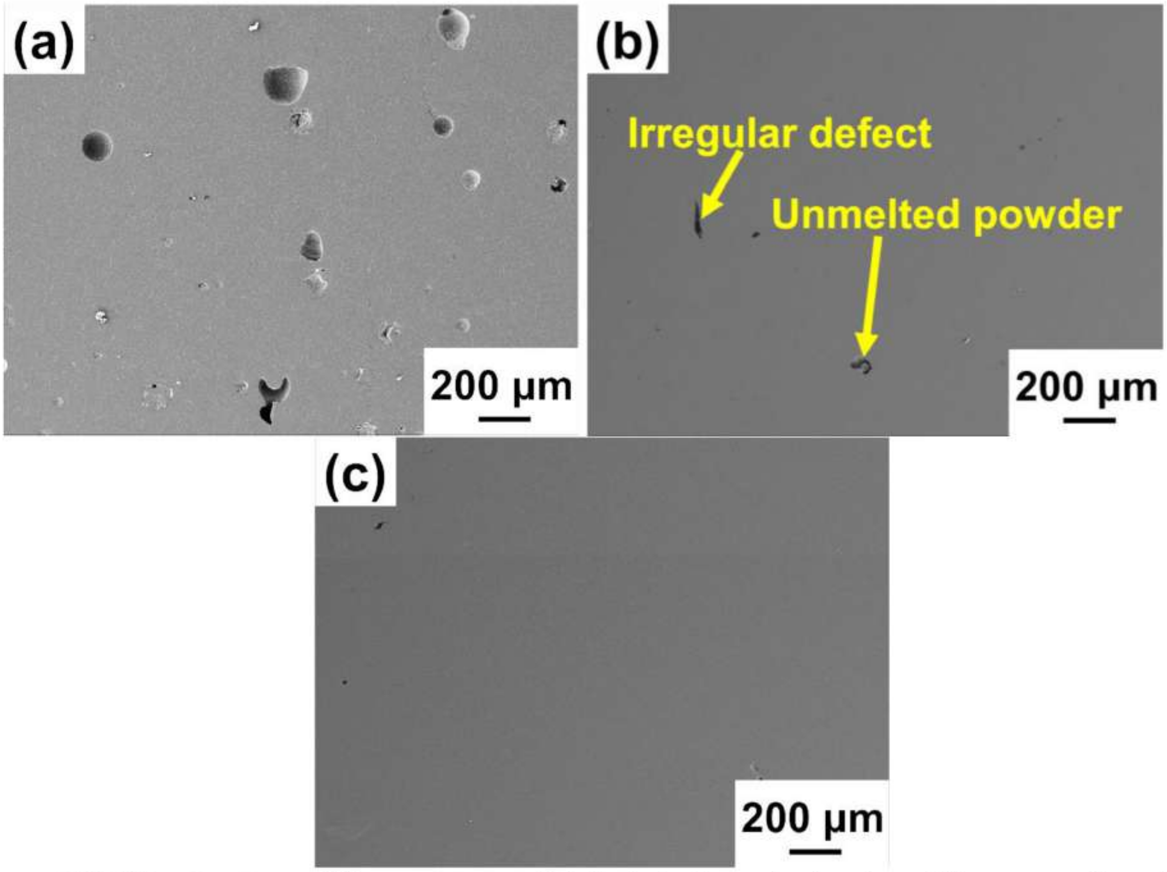

Figure 3.4 Micostructure of the specimens fabricated at constant volumetric energy E_V = 182 J/mm^3: (a) P = 300 W, v_s = 300 mm/s, l_{hs} = 0.11 mm and l_z = 0.05 mm, (b) P = 200 W, v_s = 200 mm/s, l_{hs} = 0.11 mm and l_z = 0.05 mm; (c) micostrucuture of the specimens built with optimized parameters: P = 190 W, v_s = 165 mm/s, l_{hs} = 0.08 mm and l_z = 0.04 mm.

Moreover, the chemical composition of the Al-Cu-Mg-Si powder and the SLM Al-Cu-Mg-Si alloy is listed in Table 3.1. It indicates that different from the SLM Al-Zn and Al-Mg alloys [210], there is no serious change of chemical composition during SLM processing of Al-Cu-Mg-Si alloy. It also contributes to the reliability of the processing parameters and the reproducibility of the SLM Al-Cu-Mg-Si alloy.

Table 3.1 Chemical composition of the as-received Al-Cu-Mg-Si powder and the as-SLM samples.

Element (wt. %)	Cu	Mg	Si	Mn	Al
Al-Cu-Mg-Si powder	3.56 ± 0.03	1.45 ± 0.01	1.12 ± 0.01	0.62 ± 0.01	balance
SLM Al-Cu-Mg-Si alloy	3.63 ± 0.03	1.42 ± 0.01	0.98 ± 0.01	0.63 ± 0.01	balance

3.3 Phase analysis and microstructural characterization

The phase analyses of as-prepared Al-Cu-Mg-Si samples and samples with T6 heat treatment are shown in Fig. 3.5. The as-SLM sample shows the presence of the α-Al phase (space group $Fm\bar{3}m$ [199]) and a few small peaks in the range between 46 ° to 51 ° from the Q phase (unknown space group) (Fig. 3.5(b)). After T6 heat treatment, the Al-Cu-Mg-Si alloy T6 contains the following phases: α-Al, Mg_2Si ($Fm\bar{3}m$ [198,199]) and Al_xMn_y (unknown space group), suggesting that the Q phase transforms to Mg_2Si and Al_xMn_y during heat treatment.

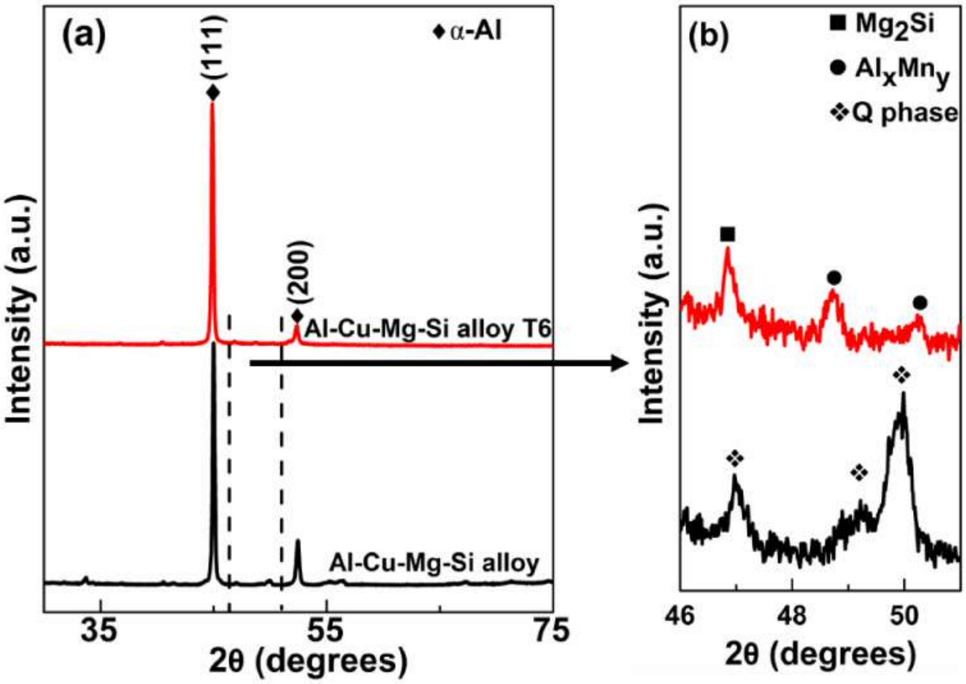

Figure 3.5 XRD patterns of the optimized Al-3.5Cu-1.5Mg-1Si samples processed by SLM in as-prepared and heat-treated conditions: (a) overview and (b) close-up view of the diffraction patterns between 46 °≤ $2\theta \leq$ 51 °

The microstructures of the SLM samples before and after heat treatment were observed by SEM and EDS (Fig. 3.6). Compared with Fig. 3.1(b), after SLM processing, the micro-segregation of the powders microstructure generated from the gas-atomization disappears and the SLM specimens exhibit a different microstructure with granular phases. Due to the low Cu content and high cooling rate, a fine granular phase is dispersed uniformly in the α-Al matrix of the individual melt tracks. A similar microstructure was reported for the Al-4Si alloy processed by SLM [102]. However, due to the gradual increase of the cooling rate with increasing distance from the top of the melt pool [85,238], the dissolution of elements at the bottom of the melt pool is lower than in the center, resulting in the coarser phase at the bottom of the melt pool. Moreover, it should be mentioned that the heat-affected zone at the boundary of the tracks, which has been studied in previous works (e.g., SLM Al-12Si alloy and SLM Al-10Si-Mg alloy, mentioned in Section 1.2.2.5) [59,65], also has a coarser microstructure between the tracks similar to the microstructure at the bottom of the melt pool. Therefore, there is an obvious boundary between two individual laser tracks, which shows a different microstructure than the melt pool. According to the EDS analysis of the as-SLM specimen at high magnification (Fig. 3.6(a)), the unidentified phase contains Cu, Mg and Si elements, which suggests that this secondary phase is probably the quaternary Q phase (common phase in Al-3.5Cu-1.5Mg-1Si alloys) [199,239]. The amount of Q phase evaluated from SEM analysis (7 ± 1 vol. %, analyzed by Image-Pro plus software (version 6.0 Software, Media Cybernetics, Inc. USA)) appears to be higher than that observed by XRD (Fig. 3.5). This behavior can be ascribed to the different resolution of the techniques, XRD being less sensitive to small amount of nano-sized or ultrafine-grained phases. As shown in Fig. 3.6(b), the Al-Cu-Mg-Si alloy T6 displays a uniform microstructure without the heterogeneities resulting from the melt tracks. In addition, two different secondary phases (black and white contrast phases) embedded in the Al matrix are visible. EDS analysis at high magnification (Fig. 3.6(b), lower panels) indicates that the white secondary phase in the Al-Cu-Mg-Si alloy T6 is Mn-rich, while the black phase contains more Mg and Si, in agreement with the XRD results in Fig. 3.5 showing the formation of the Mg_2Si and Al_xMn_y phases in this sample.

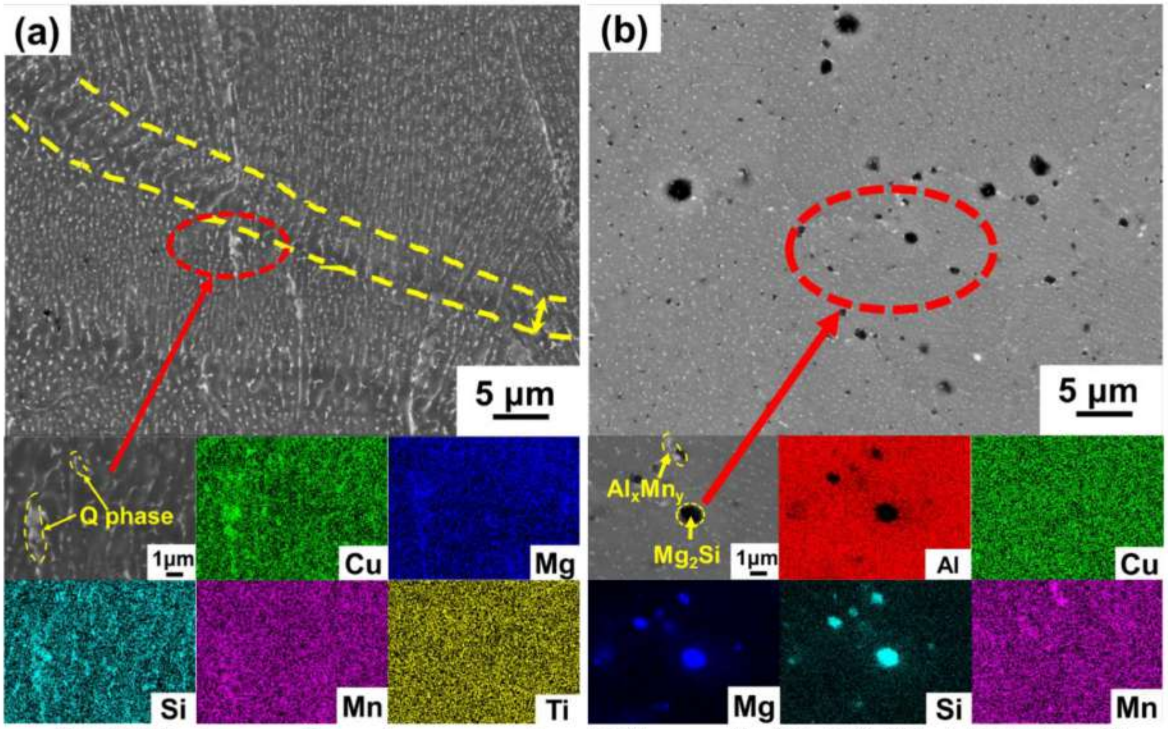

Figure 3.6 SEM micrographs and corresponding EDS maps for (a) Al-3.5Cu-1.5Mg-1Si alloy and (b) Al-3.5Cu-1.5Mg-1Si alloy T6.

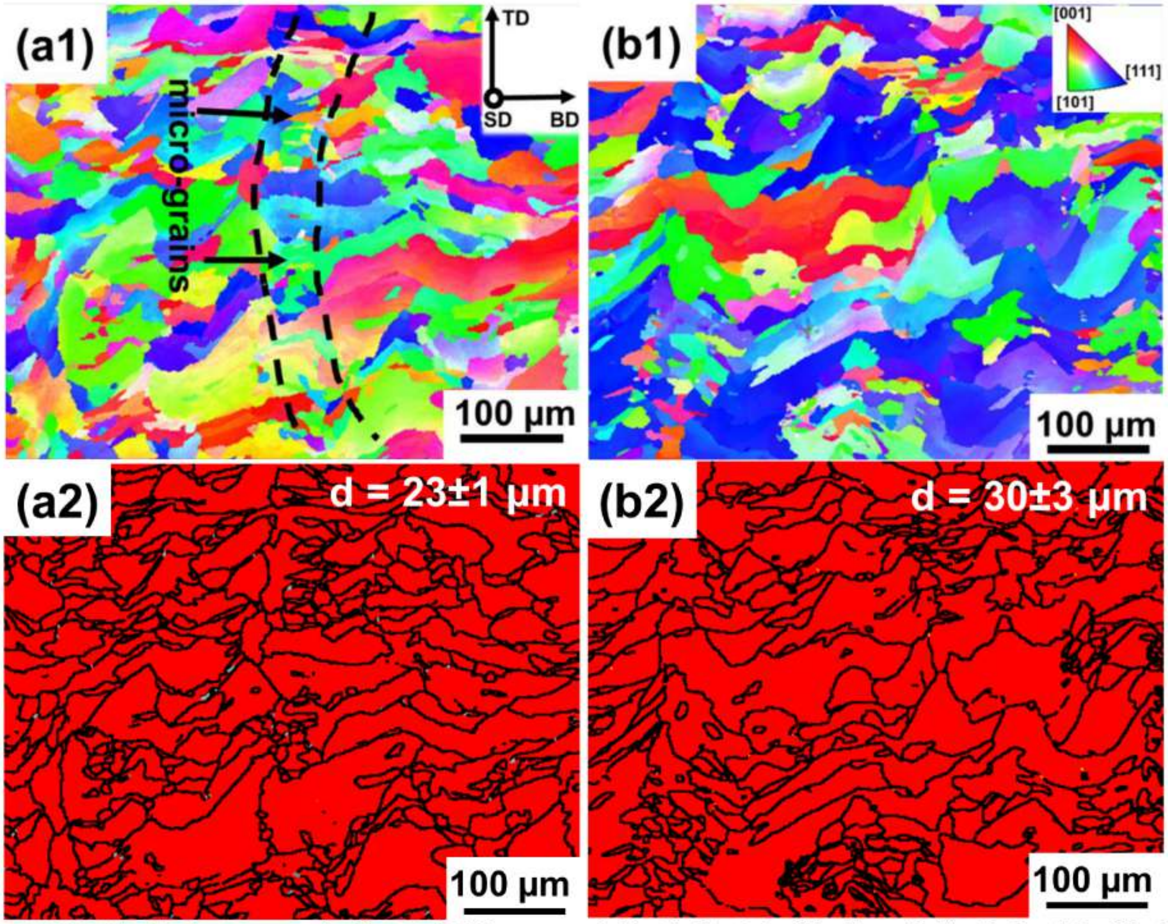

Figure 3.7 EBSD inverse pole figure (IPF) maps: (a1) Al-Cu-Mg-Si alloy, (b1) Al-Cu-Mg-Si alloy T6. Inset: the spatial orientation with respect to the building direction (BD), scanning direction (SD) and transverse direction (TD); the color code used for the crystal orientation along the building direction are given in the top part of the figure. EBSD grain boundary map of the Al-Cu-Mg-Si alloy (inset: equivalent grain diameter of Al): (a2) Al-Cu-Mg-Si alloy, (b2) Al-Cu-Mg-Si alloy T6.

Fig. 3.7 displays the EBSD IPF maps of the SLM Al-Cu-Mg-Si specimens with the crystal orientations plotted with respect to the building direction (BD) and the corresponding EBSD grain boundary map of the Al phase. In the as-SLM condition, the dominant microstructure features are columnar grains oriented almost parallel to BD. Fig. 3.7(a1) reveals an almost random texture with respect to BD, which is similar to other reports on SLM Al-based alloys like Al-Si and Al-Si-Mg alloys [59,88,116,192]. In addition, the micro-grains generated between the overlaps of tracks are visible, which might be due to the heat effect between tracks and the gradual decrease of the solidification rate from the center to the edge of the melt pool [59,86,89]. Fig. 3.7(a2) shows that the average grain size of as-prepared Al-Cu-Mg-Si alloy determined by EBSD is 23 ± 1 μm, which is significantly larger than the Al-Si and Al-Si-Mg alloys processed in Refs. [59,116]. In general, the grain size of the SLM Al-12Si and Al-10Si-Mg alloy is less than 12 μm and the columnarity is less pronounced than the SLM Al-3.5Cu-1.5Mg-1Si alloy. The reason for this might be on the one hand the comparably higher energy density used for SLM processing in the current study, leading to slower solidification rate and, thus, larger grains. On the other hand, the high amount of Si [59,116] might be responsible for significant grain refinement in the Al-Si and Al-Si-Mg alloys, as also reported by Sistiaga *et al*. [124]. After T6 heat treatment, the average grain size (30 ± 3 μm) is larger than in the case of the as-prepared Al-Cu-Mg-Si sample (23 ± 1 μm). It should be mentioned that the fiber texture of the Al phase has no clear evolution trend before and after heat treatment, which might be related to many factors, such as the heat treatment temperature, directional processed-induced residual stress and the selected position of samples for the EBSD measurement, as typically reported for additively manufactured materials [46,240,241].

Fig. 3.8 displays the TEM images and SAED patterns taken from the as-SLM and SLMT6 Al-Cu-Mg-Si specimens. The as-SLM specimen shows the presence of a high density of dislocations and sub-grain boundaries in the Al matrix (Fig. 3.8(a)). The SAED pattern of the matrix (Fig. 3.8(a1)) shows an [100] Al zone axis pattern and additional reflexes from a precipitate apart from the Al matrix. Combining the SAED patterns and the results from TEM/EDS analysis allows us to identify the precipitates to be mainly Q phase (63.6 ± 0.2 at. % Al, 4.3 ± 0.1 at. % Cu, 15.1 ± 0.1 at. % Mg and 5.3 ± 0.1 at. % Si) with the presence of some Al_2Cu (θ phase, 85.0 ± 0.2 at. % Al, 10.4 ± 0.1 at. % Cu, 1.4 ± 0.0 at. % Mg and 0.9 ± 0.0 at. % Si) [198,242]. After T6 heat treatment, the dislocations and sub-grains disappear, and different precipitates are observed in the Al matrix (Fig. 3.8(b)). The [100] Al zone axis SAED pattern taken from the Al matrix (Fig. 3.8(b)) reveals weak additional reflections. The highly streaked reflections are caused from different variants of needle-shaped nano-$Al_2Cu(Mg)$ (*S*' and *θ*' phase) precipitates (Fig. 3.8(b)) [242,243]. In addition, the phase in Fig 3.8(b) was identified as Al_xMn_y by using TEM/EDS (69.5 ± 0.3 at. % Al and 9.3 ± 0.2 at. % Mn), whose lattice structure is difficult to analyze by SAED. The presence of cubic Mg_2Si phase (59.6 ± 0.3 at. % Mg and 26.0 ± 2 at. % Si) was also revealed from TEM/EDS and SAED in Fig. 3.8(b). All TEM results are in accordance with the XRD patterns and the SEM/EDS results, which provides a strong support to the analysis of the mechanical properties.

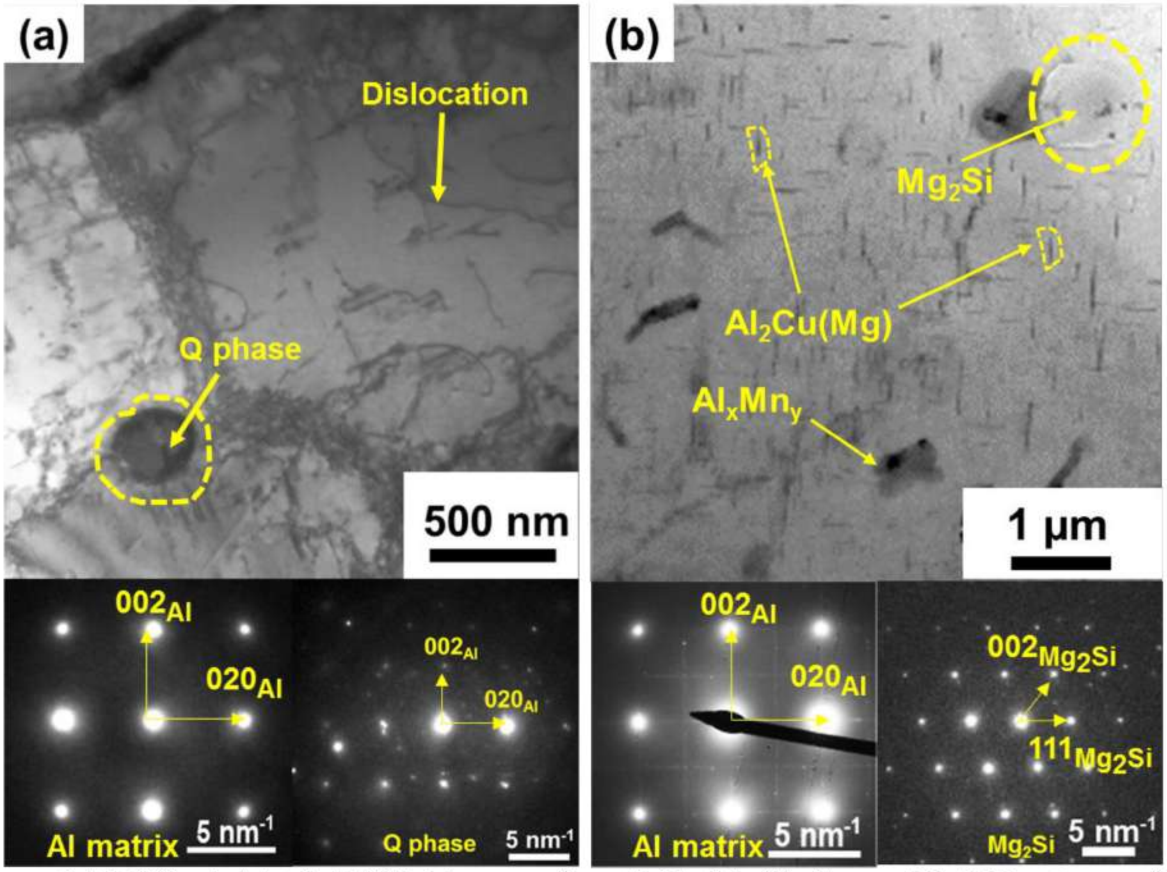

Figure 3.8 $[100]_{\mathrm{Al}}$ bright-field TEM images of an Al-Cu-Mg-Si alloy and SAED patterns of the corresponding phases: (a) overview of the as-prepared sample and corresponding SAED pattern of the Al matrix and Q phase; (b) overview of the heat treated specimens and corresponding SAED pattern of the Al matrix and Mg_2Si phase.

3.4 Mechanical properties and strengthening mechanism

Fig. 3.9 shows the characteristic room-temperature tensile stress-strain curves for the present as-SLM and SLMT6 Al-Cu-Mg-Si alloy and Table 3.2 compares their mechanical properties with different alloys, namely the Al-12Si alloy fabricated by SLM and the commercial 2024 alloy O and 2024 alloy T6. The as-SLM samples exhibit higher ultimate tensile strength (UTS) of 372 ± 7 MPa and yield strength (YS) of 222 ± 2 MPa, but lower elongation (5.8 ± 0.5 %) than the AA2024 alloy O. This results from the fact that due to the high cooling rate, a supersaturated solid solution of Cu, Mg and Si in the Al matrix is formed, leading to enhanced solid-solution strengthening. Additionally, the refined grains contribute to the refinement strengthening [59,184]. The high dislocation density (Fig. 3.8(a)) generated during SLM processing also contributes to enhance the strength. The strength of the as-prepared SLM specimens is improved significantly after T6 heat treatment. The YS (433 ± 4 MPa), UTS (512 ± 5 MPa) and elongation (6.5 ± 0.4 %) of the Al-Cu-Mg-Si alloy T6 meet the standard of the AA2024 alloy T6 (Table 3.2). Also, the UTS, YS and elongation of the Al-Cu-Mg-Si alloy T6 are higher than the SLM Al-12Si alloy (Table. 3.2). This mainly results from the generation of the nano-precipitates (θ' and *S*' phases) (Fig. 3.8(b)) enhancing the strength [214]. But the elongation is still around 5-6 % and, thus, not significantly improved by the T6 heat treatment. In order to investigate the fracture mechanism further, the fracture morphologies of the specimens are observed below.

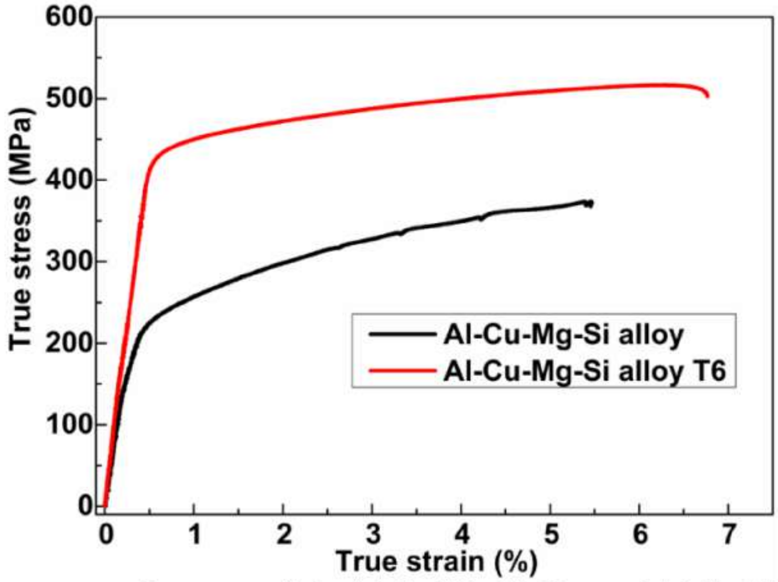

Figure 3.9 Tensile stress-strain curves of the Al-Cu-Mg-Si alloy and Al-Cu-Mg-1Si alloy T6.

Table 3.2 Comparison of the tensile properties of the SLM Al-3.5Cu-1.5Mg-1Si alloy with SLM Al-12Si alloy and commercial alloys.

Materials type	Method	YS (MPa)	UTS (MPa)	Elongation (%)
Al-Cu-Mg-Si alloy	SLM	222 ± 2	372 ± 7	5.8 ± 0.5
Al-Cu-Mg-Si alloy T6	SLM	433 ± 4	512 ± 5	6.5 ± 0.4
Al-12Si alloy	SLM	208 ± 8	403 ± 4	5.6 ± 0.3
Commercial 2024 alloy O	Ref. [173,189]	< 95	< 220	≥ 12
Commercial 2024 alloy T6	Ref. [173,189]	≥ 345	≥ 427	≥ 5

The fracture surfaces (Figure 3.10) were investigated both at low and high magnification to study the fracture mechanism. Pores are observed on the fracture surface of both the samples (Figs. 3.10(a1)-(b1)). The defects are surrounded by several un-melted powder particles and laser tracks.

This reveals that the failure of these samples starts around these defects indicating that the presence of pores is detrimental to the fracture of SLM Al alloys. A similar phenomenon was observed for SLM Al-10Si-Mg alloys [118]. Also, an intergranular fracture morphology can be observed from the high magnification images around almost fully dense sites for both types of specimens, which indicates that the cracks propagate along the grain boundaries. As shown in the bottom-left corner images (insets in Figs. 3.10(a1) and (b1)), the fracture zones are surrounded by deep cracks correspond to the grain size (20-40 μm) measured by EBSD. This confirms that the crack propagation occurs along the interface of the columnar grains. In addition, dimples are observed in Figs. 3.10(a2) and (b2), suggesting that both specimens exhibit fine dimples with different secondary phases according to the EDS maps. These dimples indicate the plasticity of the specimens with and without heat treatment. As displayed in Fig. 3.10(a2), the EDS maps show particles containing Cu, Mg and Si in the dimples. Corresponding to the previous discussion (Section 3.3), these particles should be the Q phase. The Q phase present in the as-prepared specimens helps to pin dislocations and results in the formation of the dimples, affects the plasticity of the as-SLM specimens. Moreover, the presence of a high density of dislocations and fine grains can further improve the strength of the as-prepared specimens. According to TEM and EBSD analysis, the dislocations disappear after T6 heat treatment, and the Q phase transforms to Mg_2Si and Al_xMn_y phases, which were also found in the dimples of the heat treated specimens by the EDS maps (Fig. 3.10(b2)). These phases have the same effect on the mechanical properties as the Q phase, i.e., they contribute to the pinning effect and the formation of dimples. Therefore, the presence of Al_xMn_y and Mg_2Si phases influences the plasticity of the SLMT6 specimens. It should be highlighted that after heat treatment, needle-shaped nano-precipitates (*S*' and *θ*' phases) are generated and disperse evenly in the Al matrix (Fig. 3.10(b1)). These nano-precipitates contribute to the overall strengthening through an additional Orowan bypass mechanism [244], which strengthens the Al matrix and improves the tensile strength of the SLM Al-Cu-Mg-Si alloy T6.

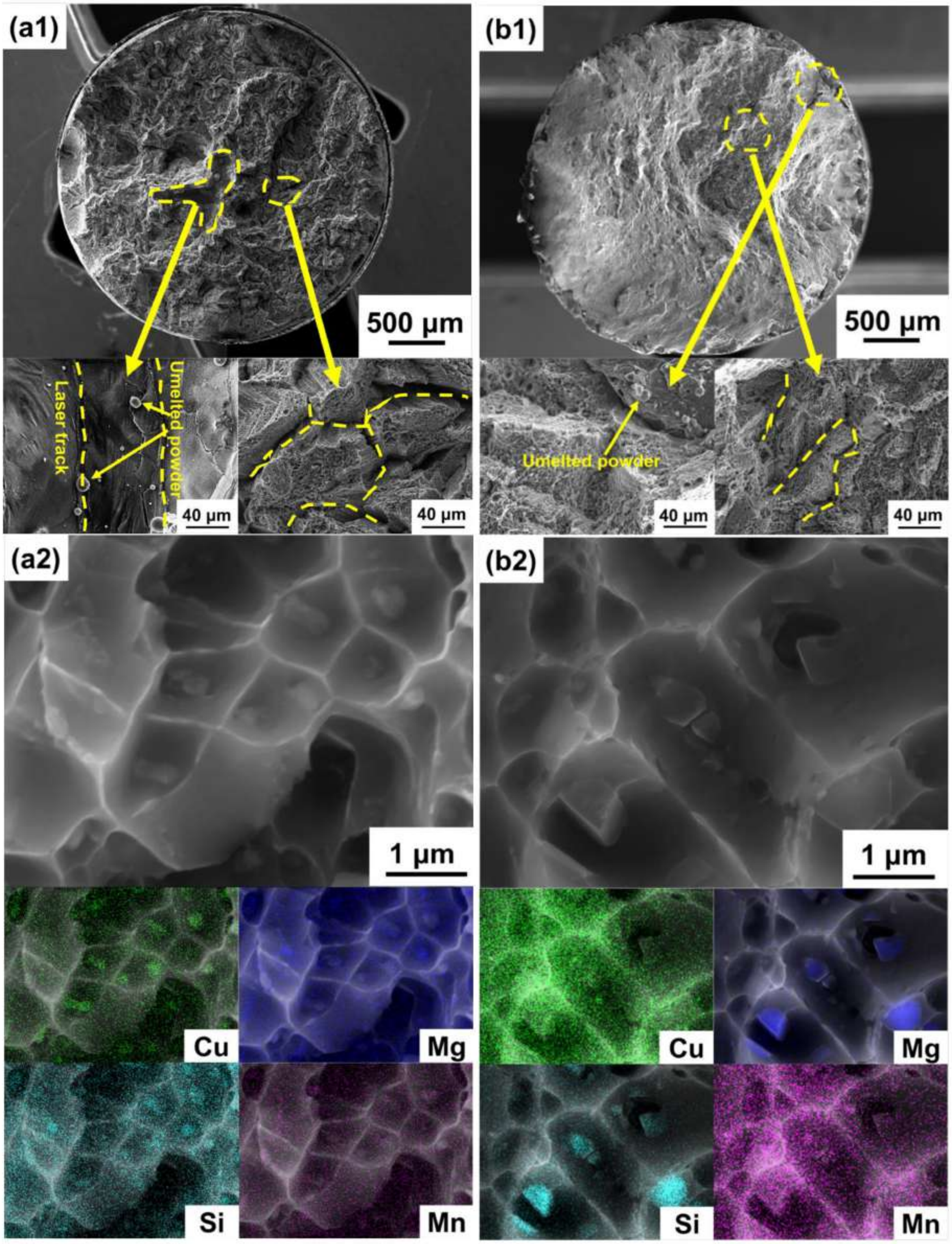

Figure 3.10 Fracture morphology and EDS maps of as-prepared Al-Cu-Mg-Si alloy (a1-low magnification; a2-high magnification) and heat treated Al-Cu-Mg-Si alloy (b1-low magnification; b2-high magnification) Al-3.5Cu-1.5Mg-1Si specimens processed by SLM.

CHAPTER 4

Tribological and corrosion properties of SLM Al-Cu-Mg-Si alloy

In general, engineering components work under a special environmental condition, thus the materials need to have a certain wear and corrosion resistance. Therefore, except for the good mechanical properties, the tribological and corrosion properties of materials have to been considered and investigated.

On the basis of Chapter 3, this chapter presents the tribological and corrosion behaviors of the SLM Al-Cu-Mg-Si alloy. In order to evaluate the tribological and corrosion properties of the SLM Al-Cu-Mg-Si alloy, the commercial AA2024 alloy O was investigated as a reference materials. The as-prepared SLM Al-Cu-Mg-Si alloy and AA2024 alloy O were also heat treated at the T6 heat treatment condition (described in Section 2.1.3), and all specimens before and after T6 heat treatment were investigated at the same test conditions. The morphologies of all materials and their corresponding phases before and after the tribological and corrosion test were characterized leading to the discussion of wear mechanism and corrosion mechanism.

4.1 Tribological properties of SLM Al-Cu-Mg-Si alloy

Fig. 4.1 displays the typical microstructures of the SLM Al-Cu-Mg-Si alloy and the AA2024 alloy before and after T6 heat treatment [59,91,184]. Due to the rapid solidification during SLM processing, the fine Q phase, which contains Al, Cu, Mg and Si elements, is generated in the Al matrix. After T6 heat treatment, the Al matrix shows the formation of the $Al_2Cu(Mg)$ (θ’ and S’) phase, which leads to a significant improvement of the tensile strength. In addition, the heat treatment results in the transformation of the fine Q phase into Mg_2Si and Al_xMn_y (Fig. 4.1(b1)). All the details have been described in Chapter 3. It should be mentioned that the formation of these phases, especially the Mg_2Si phase, has a significant importance in improving the friction and wear properties of the Al-Cu-Mg-Si alloys [245]. Compared with the SLM Al-Cu-Mg-Si alloy, the white θ-Al_2Cu phase (EDS measurement: 74.7 ± 1.2 at. % Al and 24 ± 1.1 at. % Cu) is the main phase dispersed in the AA 2024 alloy O (Fig. 4.1(a2)). After T6 heat treatment, the Al_2Cu phases is dissolved into Al matrix, and the undefined phases (EDS measurement: containing mainly more 65.5 ± 0.4 at. % Al, 6.2 ± 0.5 at. % Cu, 7.4 ± 0.4 at. % Mn and 12.9 ± 0.4 at. % Fe) are generated. Similar microstructures and phases were described in early works on the 2024 alloy [246-250].

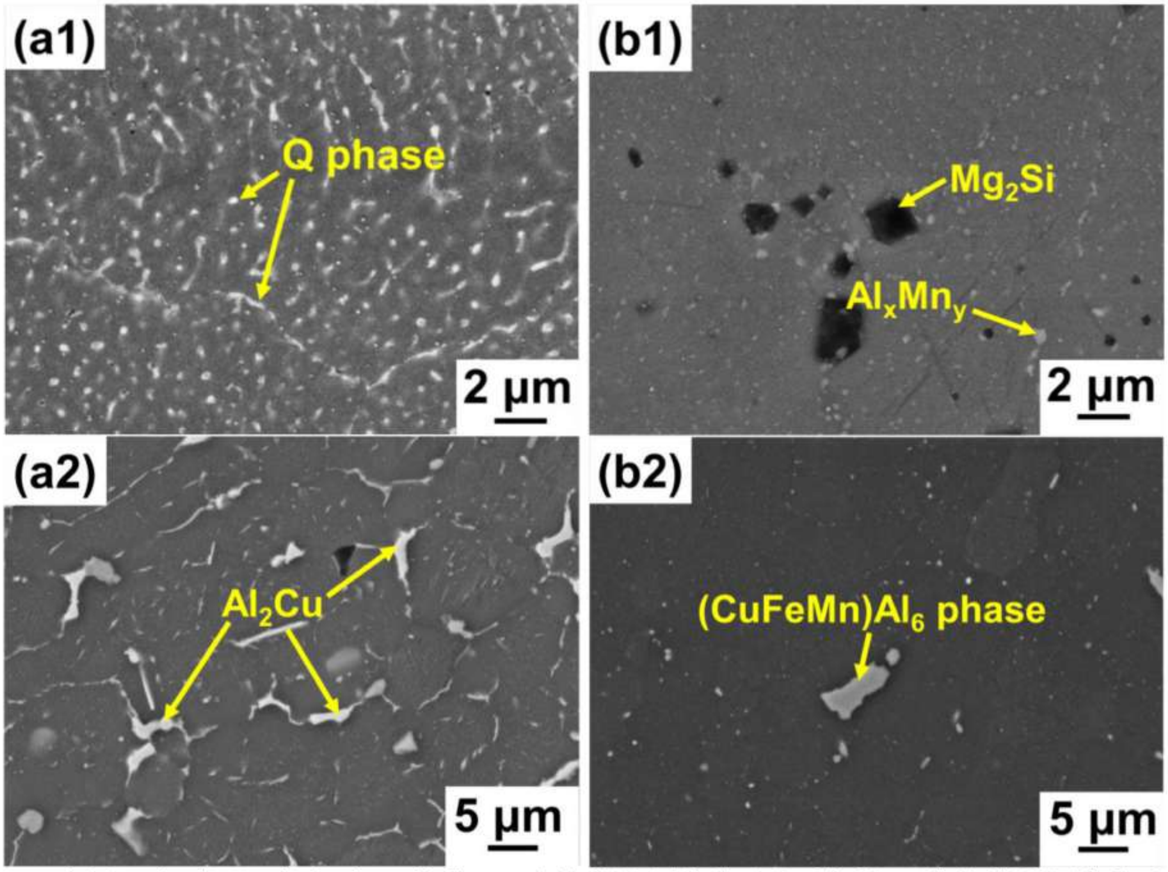

Figure 4.1 Typical morphologies of alloys: (a1) SLM Al-Cu-Mg-Si alloy, (b1) SLM Al-Cu-Mg-Si alloy T6, (a2) AA2024 alloy O, (b2) AA2024 alloy T6.

The microhardness, the average coefficient of friction (average COF) and the specific wear rate of all alloys are delineated in Fig. 4.2. The microhardness, the average COF and the specific wear rate of AA2024 alloy O and AA2024 alloy T6 is 73 ± 1 $HV_{0.05}$, 0.47 ± 0.02, 2.23 ± 0.01 × 10^{-4} $mm^3(Nm)^{-1}$; 179 ± 1 $HV_{0.05}$, 0.36 ± 0.01, 1.74 ± 0.08 × 10^{-4} $mm^3(Nm)^{-1}$, respectively. In this work, the as-fabricated SLM Al-Cu-Mg-Si alloy has a higher hardness (124 ± 1 $HV_{0.05}$), lower average COF (0.40 ± 0.01) and lower specific wear rate (1.8 ± 0.11 × 10^{-4} $mm^3(Nm)^{-1}$) than the 2024 alloy O. After T6 heat treatment, with increasing hardness of the SLM Al-Cu-Mg-Si alloy to (176 ± 1 $HV_{0.05}$), the average COF and the specific wear rate decrease to 0.34 ± 0.01 and 1.48 ± 0.02 × 10^{-4} $mm^3(Nm)^{-1}$. The formation of nano-$Al_2Cu(Mg)$ precipitates in the AA2024 alloy T6 and SLM

Al-Cu-Mg-Si alloy T6 leads to the enhancement of the mechanical properties. According to the classical Archard's equation, the coefficient of friction and wear loss of a materials is inversely proportional to its hardness on adhesive wear condition [251-253]. Therefore, after heat treatment, the strengthened Al matrix of the Al-Cu-Mg-Si alloy T6 results in the improvement of its frictional and wear properties. It is striking that the AA2024 alloy T6 has slightly higher hardness but relatively lower specific wear rate than the SLM Al-Cu-Mg-Si alloy. In general, the higher Cu and Mg contents (Table 4.1) in AA2024 alloy T6 can result in more nano-$Al_2Cu(Mg)$ precipitates in the Al-matrix than SLM Al-Cu-Mg-Si alloy T6, contributing to the higher hardness of AA2024 alloy T6 [227,254]. However, due to positive effect of the solid solution of Si on the wear properties of the Al-Cu-Mg alloy [245,255,256], the high Si content in SLM Al-Cu-Mg-Si alloy T6, especially the formation of Mg_2Si (Fig. 4.1(b1)), can lead to the lower average COF and specific wear rate than the AA2024 alloy T6.

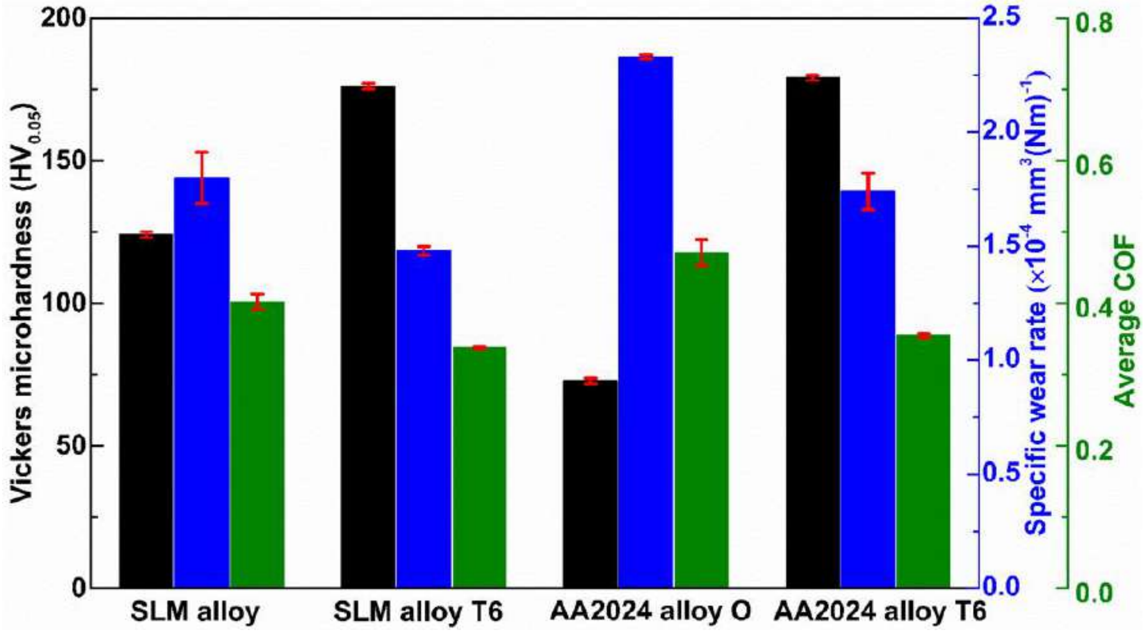

Figure 4.2 Microhardness, average coefficient of friction (average COF) and specific wear rate of all specimens.

In addition, after the heat treatment, the Q phase in the Al-Cu-Mg-Si alloy dissolves into the Al matrix, and the nano-precipitates are dispersed uniformly in the matrix, which not only strengthen the Al matrix, but also eliminates the classical layer-by-layer microstructure generated during SLM processing (Fig. 3.6). The disappearance of the layer-by-layer microstructure results in that SLM Al-Cu-Mg-Si alloy T6 has a lower standard error of the average COF and the specific wear rate than as-prepared SLM alloy.

Table 4.1 Chemical composition of the SLM Al-Cu-Mg-Si alloy and the AA2024 alloy.

Element (wt. %)	Cu	Mg	Si	Mn	Al
AA2024 alloy O	4.06 ± 0.01	1.36 ± 0.01	0.18 ± 0.01	0.57 ± 0.01	balance
SLM Al-Cu-Mg-Si alloy	3.63 ± 0.03	1.42 ± 0.01	0.98 ± 0.01	0.63 ± 0.01	balance

In order to compare the wear mechanism of the SLM materials with the commercial alloy, the worn surfaces of all materials are shown in Fig. 4.3. The grooves in the Al-Cu-Mg-Si alloy are slim, resulting in a smooth worn surface. After T6 heat treatment, there is the existence of fine debris and the surface is smoother than the SLM alloy without heat treatment. In spite of the existence of the fine debris in the Al-Cu-Mg-Si alloy T6, the morphologies of Al-Cu-Mg-Si alloy with and without heat treatment mainly show a typical abrasive mechanism. As a comparison, the surface of the AA2024 alloy O not only shows large grooves resulting from plastic deformation but also lots of large debris, which represents the classical mixed worn morphology, indicative of abrasive and adhesive mechanisms. Even though the formation of the nano-precipitates after T6 heat treatment improves the hardness of the Al matrix, there are still lots of large debris and an insignificant plastic deformation in AA2024 alloy T6. This indicates that despite the improved mechanical properties of the AA2024 alloy T6, the main wear mechanism of the AA2024 alloy T6 does not change. The morphological comparison of the SLM alloy T6 and AA2024 alloy T6 provides evidence for the worse wear properties of the AA2024 alloy T6 with higher hardness.

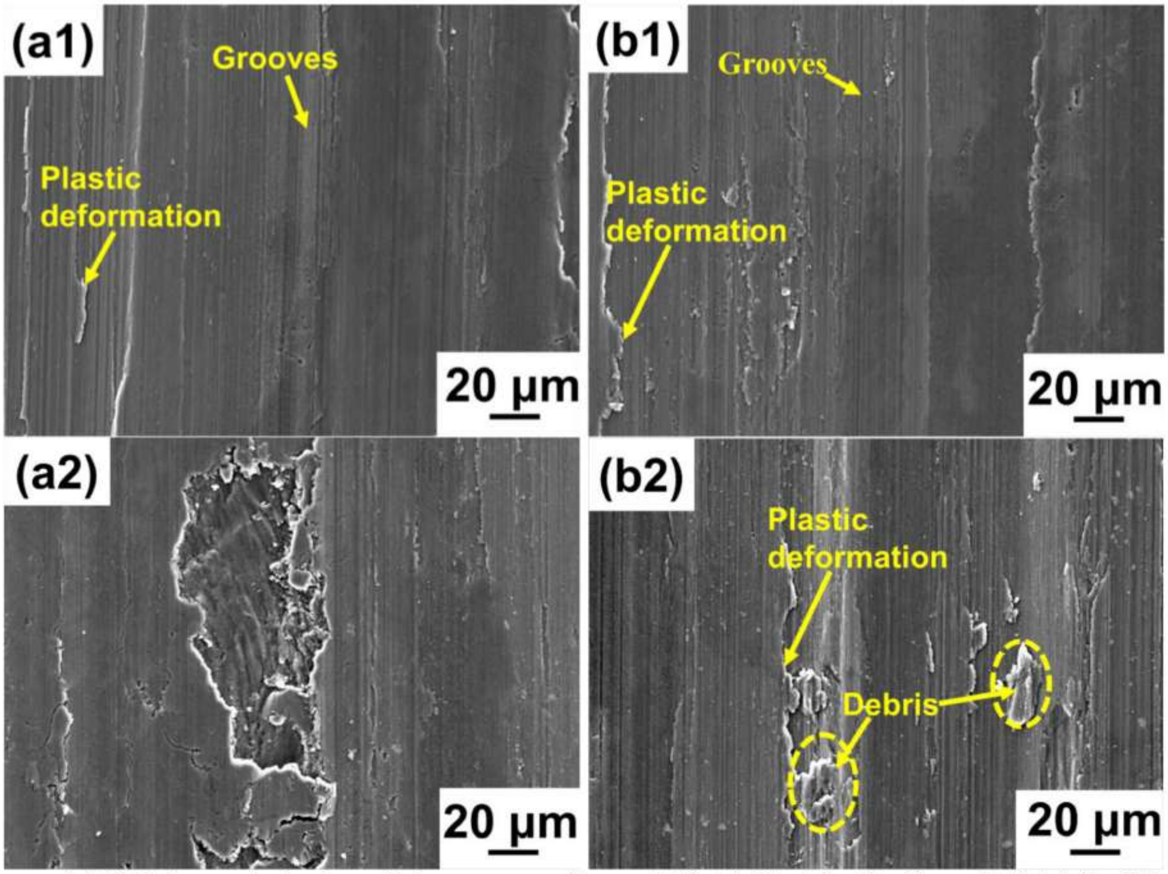

Figure 4.3 SEM morphologies of the worn surfaces: (a1) Al-Cu-Mg-Si alloy, (b1) Al-Cu-Mg-Si alloy T6, (a2) AA2024 alloy O, (b2) AA2024 alloy T6.

In order to analyze the influence of phases on the worn surfaces and wear properties, the worn surfaces of the specimens at high magnification are shown in Fig. 4.4. The fine Q phase (~ 200 nm) is embedded into the grooves of the Al matrix after wear test. After T6 heat treatment, the grooves only exhibit the area around the Mg_2Si phases. Due to the smaller size of the Al_xMn_y phase (Fig. 4.4(b1)), grooves are difficult to be observed around these fine phases. The morphologies at high magnification indicate that the small size of the Q and Mg_2Si phases respectively lead to slim grooves and smooth worn surfaces in the Al-Cu-Mg-Si alloy and the Al-Cu-Mg-Si alloy T6. Compared with the SLM alloy, the large Al_2Cu phase (≥ 2 µm) in the AA2024 alloy O is fragmented during the wear test and the pieces of the Al_2Cu phase are embedded into the Al matrix. Therefore, due to the synergistic effect of the crushed Al_2Cu hard phases and soft Al matrix, the large debris is cut off from the matrix, then attached on the Al matrix during the wear test (Fig. 4.4(a2)). In spite of the effect of the heat treatment on the strengthening of the Al matrix, the adhesive phenomenon is reduced but still some large debris on the worn surface are visible due to the large size of the (CuFeMn)Al_6 phase (Fig. 4.4(b2)). According to the above analyses, comparing with the AA2024 alloy at same heat treatment condition, the fine phases of the SLM Al-Cu-Mg-Si alloy can result in the improvement of the wear resistance.

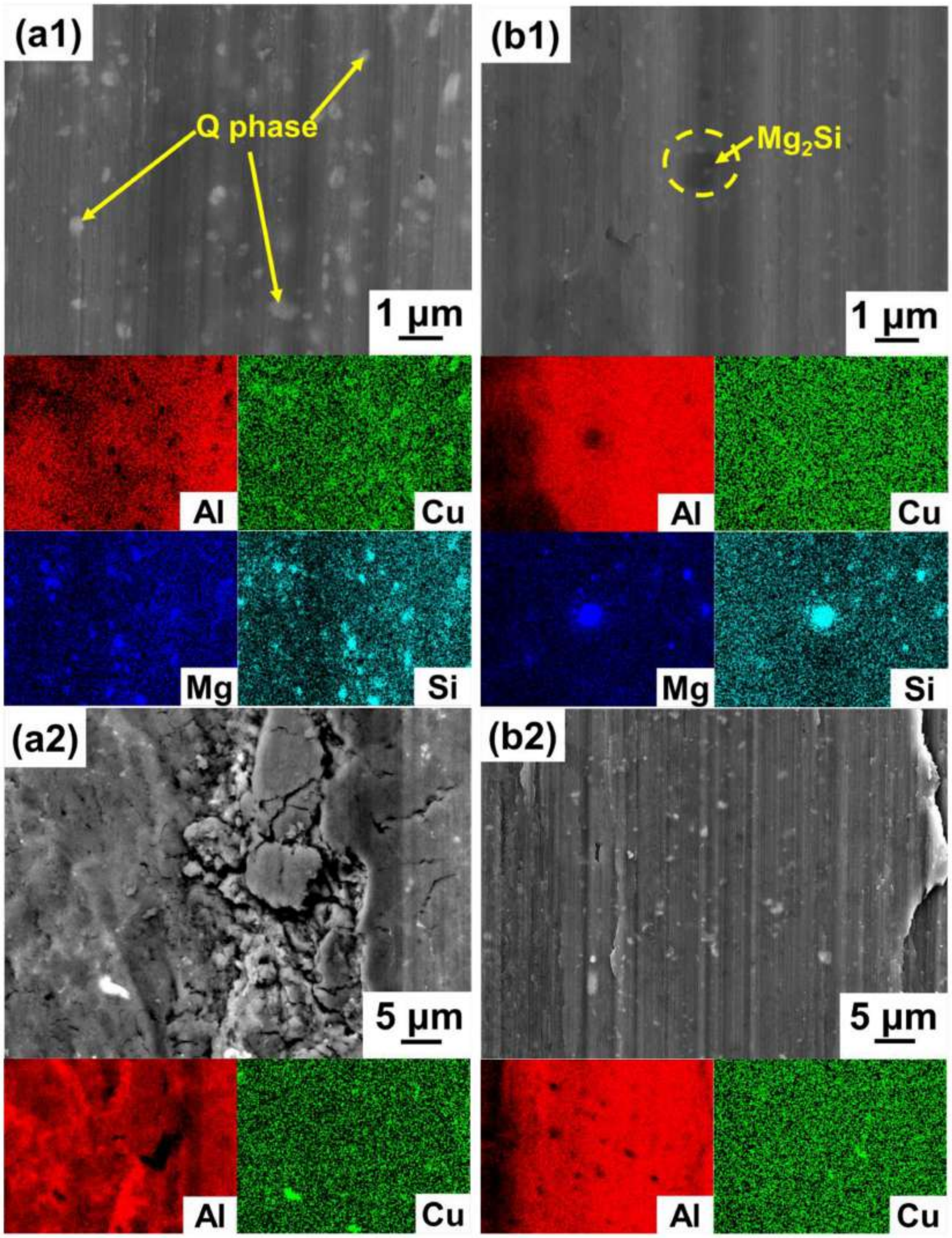

Figure 4.4 SEM close-up view and EDS mappings at high magnification: (a1) Al-Cu-Mg-Si alloy, (b1) Al-Cu-Mg-Si alloy T6, (a2) AA2024 alloy O, (b2) AA2024 alloy T6.

4.2 Corrosion behavior of SLM Al-Cu-Mg-Si alloy

Fig. 4.5 shows the representative polarization curves along with the corrosion parameters and a comparison of the polarization curves of the different alloys. As shown in Fig. 4.5(a), the potential scan starts at a value more negative than the corrosion potential (E_{corr}) and progresses in the anodic direction. This is an extreme simplification of a complex reaction scheme.

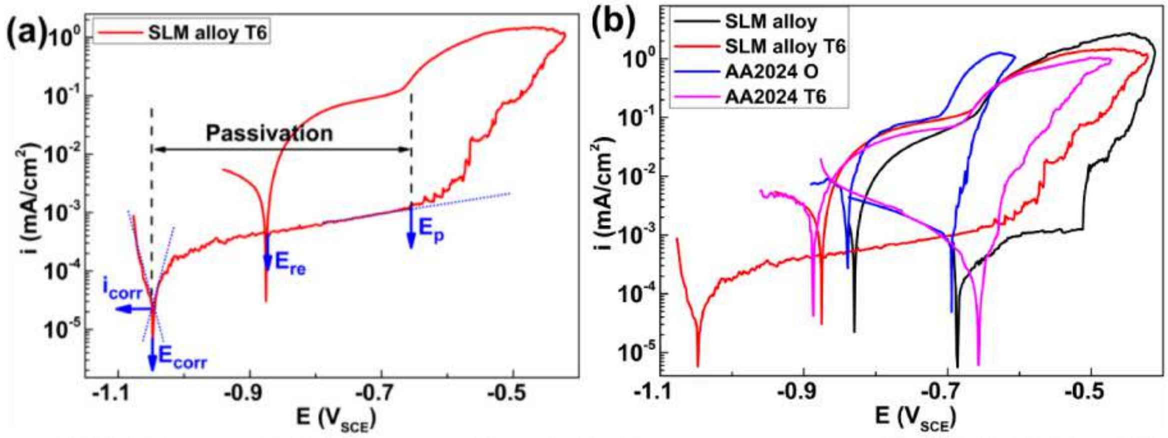

Figure 4.5 (a) Representative linear anodic polarization curves measured in 0.1 M NaCl, pH7 (de-aerated) along with the corrosion parameters, (b) Polarization curves for the SLM alloy and AA2024 alloy before and after T6 heat treatment.

Generally, in a de-aerated solution at pH7, the initial counter reaction is the water reduction [257]:

$$2H_2O + 2e^- \rightarrow H_2 + 2OH^- \tag{4.1}$$

Moreover, at this condition, there is an anodic electrochemical dissolution of Al:

$$Al \rightarrow Al^{3+} + 3e^- \tag{4.2}$$

Accordingly, the dissolved Al^{3+} further chemically reacts to form the hydroxide, which explains the immediate transfer into a passive regime:

$$Al^{3+} + 3H_2O \rightarrow Al(OH)_3 + 3H^+ \tag{4.3}$$

However, the latter reaction also causes local solution acidification, then cathodically:

$$3H^+ + 3e^- \rightarrow 3/2H_2 \tag{4.4}$$

The overall chemical reaction is the sum of two half-cell reactions based on the equations 4.1, 4.2, 4.3 and 4.4 as follows:

$$Al + 3H^+ \rightarrow Al^{3+} + 3/2H_2 \tag{4.5}$$

According to the Tafel's law [258], the electrode potential of the steady-state freely corroding condition at this two half-cell reactions is designated as the corrosion potential (E_{corr}). Moreover, the net rate of either aluminum oxidation dissolution or hydrogen reduction can be measured at E_{corr} to give the uniform corrosion rate i_{corr} at the freely corroding condition. It can be determined by the Tafel extrapolation method (dashed lines in Fig. 4.5(a)). With increasing potential, an immediate transition into the passive regime occurs as indicated by the broad anodic current density plateau (with values ≤ 1 μA/cm²). A significant increase of the current density corresponds to a local breakdown of the passive layer and pit initiation and growth. This event is reflected by a pitting potential (E_p). When the current density corresponding to the pit growth reached a pre-defined value of 1 mA/cm², the direction of the potential scan was reversed and the repassivation behaviors of the alloys was analyzed. The repassivation potential (E_{re}) can be determined as shown in Fig. 4.5(a) [259]. The typical large hysteresis in the polarization curves (i.e., a large difference between E_p and E_{re}) indicates only a limited repassivation ability (healing of the passivated surface) of all tested samples. However, the determination of E_{re}, defined as the potential at which the corroded surface repassivates during the backward scan, is not straightforward and varies in different studies [259, 260]. In the present work, the E_{re} is determined at the cross-over point of potential during the backward scan, where the hysteresis loop closes [259]. Also, E_{re} depends on the limiting current density before reverse scanning. Here, the study was limited only to one current density.

The values of the important corrosion parameters for the different alloys (listed in Table 4.2) can be derived from the polarization curves as shown in Fig. 4.5(b).

Table 4.2 Corrosion parameters obtained from polarization curves of SLM alloy and AA2024 alloy before and after heat treatment in 0.1 M NaCl solution (all potentials in V vs SCE)

Materials	E_{corr} (V_{SCE})	i_{corr} (μA/cm^2)	E_p (V_{SCE})	E_{re} (V_{SCE})
SLM Al-Cu-Mg-Si alloy	-0.686	0.1	-0.512	-0.829
SLM Al-Cu-Mg-Si alloy T6	-1.047	0.04	-0.657	-0.875
AA2024 alloy O	-0.694	1	-0.691	-0.838
AA2024 alloy T6	-0.657	0.3	-0.644	-0.886

As shown in Table 4.2, the SLM Al-Cu-Mg-Si alloy has higher E_{corr}, E_p and E_{re} values (-0.686 V, 0.512 V and -0.829 V, respectively) than the AA 2024 O (-0.694 V, -0.691 V and -0.838 V). Liang *et al.* systematically investigated the effect of the composition of Al-Cu-Mg and Al-Cu-Mg-Si alloys on the potentials and corrosion rate [261], indicating that the increasing Cu in Al-Cu-Mg-Si from 0.001 wt. % to 0.89 wt. % can increase slightly the potentials of the alloys from -0.87 ± 0.04 V_{SCE} to -0.82 ± 0.01 V_{SCE} in 0.1 M NaCl solution [261]. A similar effect of Cu on the corrosion potential of Al alloys was also reported by Meng *et al.* and Kim *et al.* [262,263]. However, as shown in Tables 4.1 and 4.2, in the present work, the AA2024 alloy O with a high content of Cu has a slightly lower corrosion potential, which may result from the high cooling rate during selective laser melting [264,265]. Even though the study of SLM alloys is quite new, especially Al-Cu-Mg-Si alloys, the Al alloys of laser surface melting have been investigated widely, which provides opportunities to understand the corrosion behavior of the SLM Al-Cu-Mg-Si alloy [247,266-268]. Liu *et al.* reported that after the surface treatment by laser melting, the E_p of the 2024Al alloy T6 containing high Si increases significantly from -0.790 V_{SCE} to -0.560 V_{SCE} in de-aerated 1 M NaCl solution, which is higher than the AA2024 pitting potential of -0.640 V_{SCE} [247]. The results reveals that the high copper solubility in the Al matrix during the high cooling rate is the key factor to the increase of the pitting potential [247].

Under the same test conditions, the corrosion potential and the pitting potential of the Al-Cu-Mg-Si alloy upon T6 heat treatment shift towards a more negative value (-1.047 V) and the corrosion rate (i_{corr}) decreases from 0.1 to 0.04 μA/cm^2. But the corrosion potential and pitting potential of the AA2024 alloy T6 shift towards a positive value (-0.657 V) and the corrosion rate (i_{corr}) decreases from 1 to 0.3 μA/cm^2. Generally, the formation and dissolution of the secondary phases have a significant influence on the changes of the corrosion potential, pitting potential and corrosion rate. Birbilis *et al.* systematically analyzed the electrochemical characteristics of the intermetallic phases in the Al matrix [269], indicating that the Mg_2Si phase has a lower corrosion potential (-1.538 V_{SCE}) but Al_7Cu_2Fe/$Al_{20}Cu_2Mn_3$ phase has a higher corrosion potential (-0.551 V_{SCE}/-0.565 V_{SCE}) than the Al matrix (-0.823 V_{SCE}) [200,269]. Therefore, after heat treatment, the formation of Mg_2Si and $(CuMnFe)Al_6$ phase shown in Fig. 4.1(b2) can result in the decrease of the corrosion potential of the Al-Cu-Mg-Si alloy T6 and increase of the corrosion potential of AA2024 T6. Moreover, after T6 heat treatment, the SLM Al-Cu-Mg-Si alloy and AA2024 alloy have a significantly lower corrosion rate than the untreated materials, as shown in Table 4.2. It results from two reasons [270]: *i*) the dissolution of the phases (such as Al_2Cu or Q phase) located in the grain boundaries of the Al matrix can improve the resistance to the intergranular corrosion (IGC) [271]; *ii*) the formation of nano-precipitates (such as Al_2CuMg or Al_2Cu) can enhance the matrix to diminishes the effect of the exfoliation and stress corrosion cracking to the corrosion rate.

In addition, as a comparison, the SLM alloys with and without T6 heat treatment have an obvious passivation range but the AA2024 alloys exhibit an active dissolution behavior. After heat treatment, the passivation range of the SLM alloy T6 is further broadened (Fig. 4.5(a)). For all tested alloys, the E_{re} values are in a similar range. But for the SLM alloy, the difference between E_p and E_{re} is much higher, indicating that once the pitting is initiated, the healing/repassivating of the alloy surface is more inhibited. Nonetheless, in comparison to actively corroding AA2024 alloy, the SLM alloys in the test solution 0.1 M NaCl show the advantage of broad and stable ranges of passivity. Therefore, the SLM Al-Cu-Mg-Si alloy can be assessed as having a good corrosion resistance.

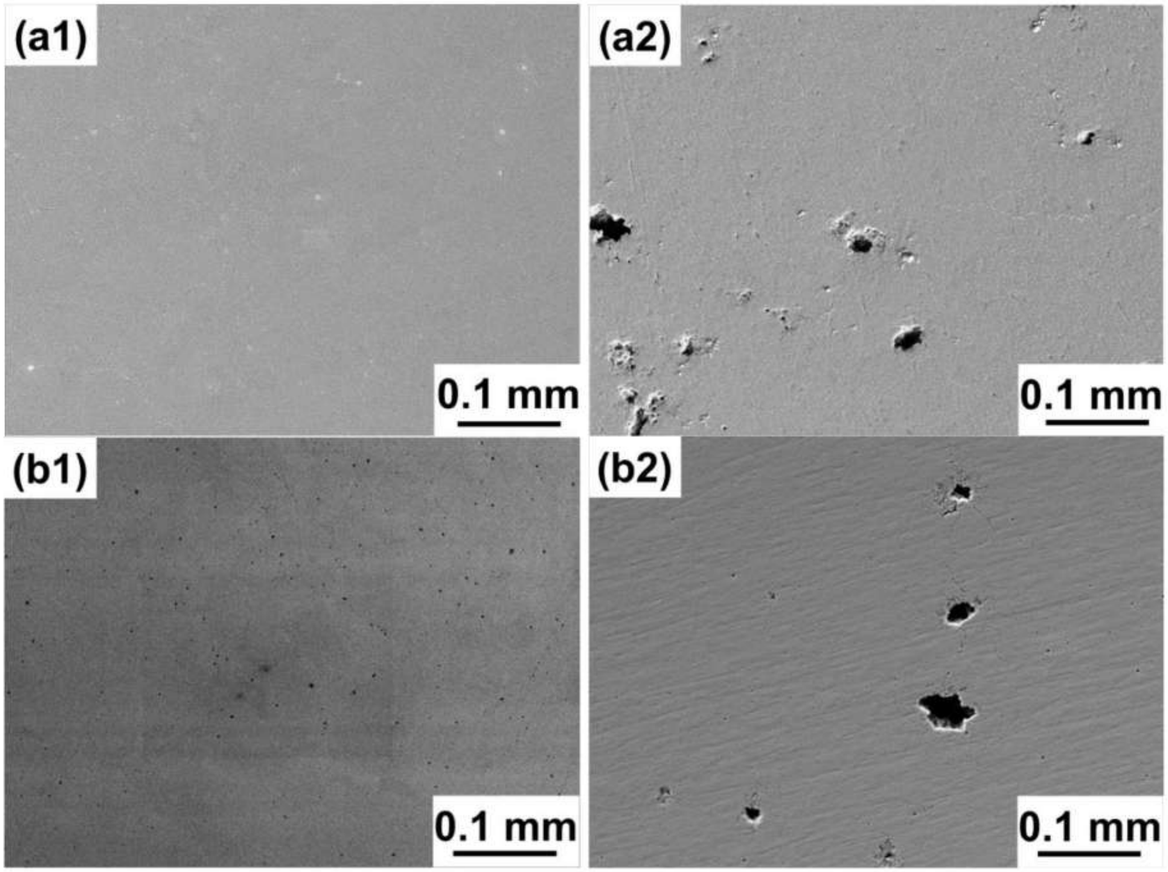

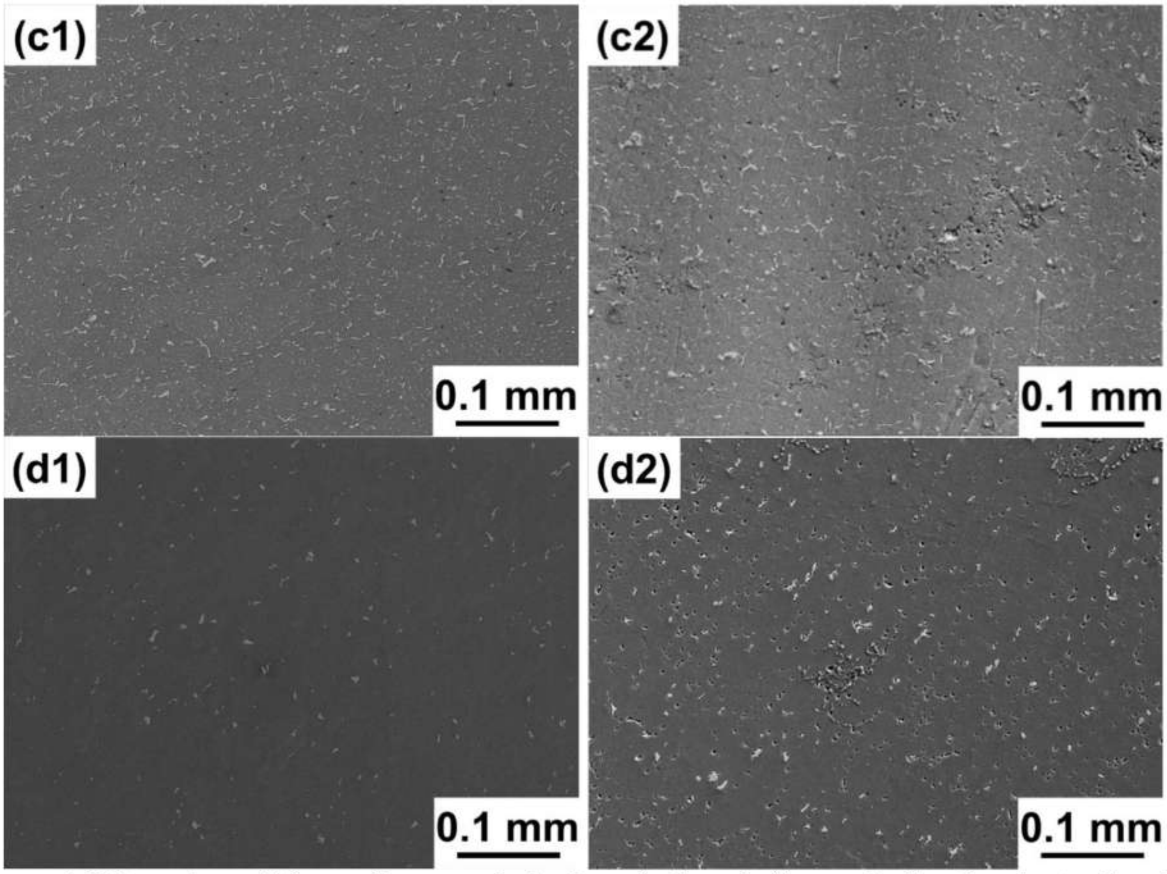

Figure 4.6 Overview of the surface morphologies of alloys before and after the electrochemical corrosion: (a1)-(a2) SLM alloy, (b1)-(b2) SLM alloy T6, (c1)-(c2) AA2024 alloy O, (d1)-(d2) AA2024 alloy T6.

Fig. 4.6 shows the surface morphologies of all materials before and after the electrochemical corrosion test. Before the corrosion test, all materials have no visible defects on the tested surface. After the corrosion test, for both SLM specimens with and without heat treatment, a significant exfoliation phenomenon of the Al matrix was observed. However, for both AA2024 alloys, a dramatic pitting phenomenon was detected. The different surface morphologies of the SLM alloys and AA2024 alloys after the corrosion test indicate that the SLM alloys and AA2024 Al during the corrosion test have a different corrosion kinetic mechanism. In order to investigate the mechanism, the microstrucutre of the alloys and the composition of precipates are characterized further.

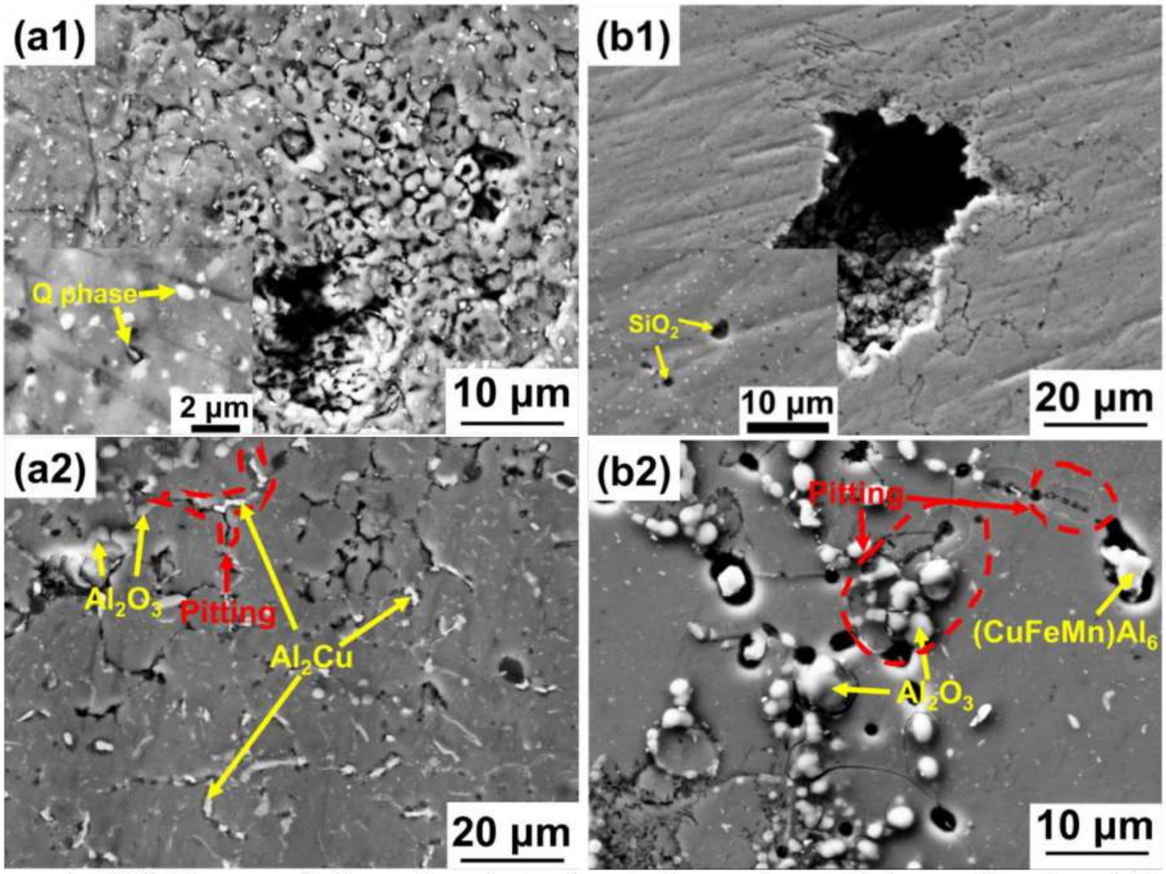

Figure 4.7 SEM images of alloys after electrochemical corrosion at high magnification: (a1) Al-Cu-Mg-Si alloy (inset: Q phase at high magnification), (b1) Al-Cu-Mg-Si alloy T6 (inset: SiO$_2$ phase at high magnification), (a2) AA2024 alloy O, (b2) AA2024 alloy T6.

The corroded surfaces and phases of all materials after corrosion test are shown in Fig. 4.7. After corrosion test, there are lots of pits generating around the orignial Q phases and these pits connect into a net (Fig. 4.7(a1)). The composition of the corroded Q phase is 90.4 ± 0.8 at. % Al, 1.8 ± 0.3 at. % Cu, 1.9 ± 0.1 at. % Mg and 0.7 ± 0.1 at. % Si, which is different from the chemical composition analysis shown in Chapter 3, especially in the ratio of Mg and Si. It indicates that there is a chemical reaction between the Q phase and the NaCl solution. However, in spite of the important effect of the Mg/Si ratio on the potential, it is difficult to further clarify this mechanism accurately in the present work due to the limitation of the equipment. As shown in Fig. 4.7(b1), there is a visible exfoliation phenomenon after the corrosion test. Around the exfoliation zone, there is a significant intergranular corrosion, where the exposed grain boundaries are acrossed by the localised precipitates. Due to the analysis of localised precipitates (inset in Fig. 4.7(b1)), the precipitates (14.9 ± 0.1 at. % Si and 27.7 ± 0.6 at. % O) are identified as SiO$_2$. In general, in the

0.1 M NaCl solution, the Mg_2Si phase has a lower corrosion potential (-1.538 V_{SCE}) than the Al matrix (-0.823 V_{SCE}) [269], which can result in a high self-dissolution of the Mg_2Si phase. The dissolution of the Mg_2Si phase protects the Al matrix. The formation of SiO_2 confirms this corrosion procedure. Moreover, the formation of SiO_2 may result in the brittleness of the grain boundaries, which can explain the exfoliation phenomenon along the boundaries in the Al matrix.

In the 0.1 M NaCl condition, due to the higher corrosion potential of the Al_2Cu phase (-0.665 V_{SCE}) than that of the Al matrix (-0.823 V_{SCE}) [269], the priority dissolution of the Al matrix results in a significant pitting phenomenon around the interface between Al and Al_2Cu phase (Fig. 4.7(a2)). The formation of Al_2O_3 (29.5 ± 2.5 at. % Al and 69.7 ± 2.6 at. % O) verifies this corrosion procedure. After T6 heat treatment, the Al_2Cu phase in the Al matrix transforms into $(CuFeMn)Al_6$ (72.6 ± 0.8 at. % Al, .6.1 ± 1.4 at. % Cu, 7.0 ± 0.0 at. % Mn and 7.4 ± 0.4 at. % Fe), which also has a higher corrosion potential (-0.551 to -0.565 V_{SCE}) than the Al matrix [269]. Therefore, there is a more significant pitting phenomenon for AA2024 alloy T6 in contrast to that for the AA2024 alloy O (Fig. 4.7(b2)).

CHAPTER 5

Al-Cu-Mg-Si-based composites and hybrid materials

Based on the good properties of the SLM Al-3.5Cu-1.5Mg-1Si alloy discussed in Chapters 3 and 4, and in order to further improve the properties of the SLM Al-Cu-Mg-Si alloy and extend their application as described in Sections 1.3.4 and 1.3.5, the Al-Cu-Mg-Si-based composites and Al-12Si/Al-Cu-Mg-Si hybrid materials were fabricated and investigated in the present chapter. Firstly, SLM alloys of Al-*x*Cu powder mixtures ($x = 4.5$, 6, 20, 33 and 40 wt.%) with the aim of designing new alloy compositions were fabricated, which also provides a certain theoretical and experimental basis on the study of the SLM composites and SLM hybrid materials. Then, a heat treatable TiB_2/Al-Cu-Mg-Si composite was fabricated by SLM, and the phase distribution, microstructure, grain size, texture and mechanical properties of the composite with and without T6 heat treatment were investigated systematically. In the last part, an Al-12Si/Al-Cu-Mg-Si hybrid alloy was designed and produced successfully. The interface quality of two base alloys (including the alloy element distribution, the microstructure and the microhardness hardness), the mechanical properties of the hybrid and its fracture mechanism were investigated.

5.1 SLM Al-*x*Cu alloys

Depending on the Al-Cu phase diagram (Fig. 5.1), the Al-*x*Cu powders ($x = 4.5$, 6, 20, 33 and 40 wt. %) were mixed and then the corresponding bulk Al-*x*Cu alloys were fabricated by SLM. The powder mixtures and their SLM samples are named after their Cu content as 4.5Cu powder, 6Cu powder, 20Cu powder, 33Cu powder, 40Cu powder; 4.5Cu alloy, 6Cu alloy, 20Cu alloy, 33Cu alloy and 40Cu alloy.

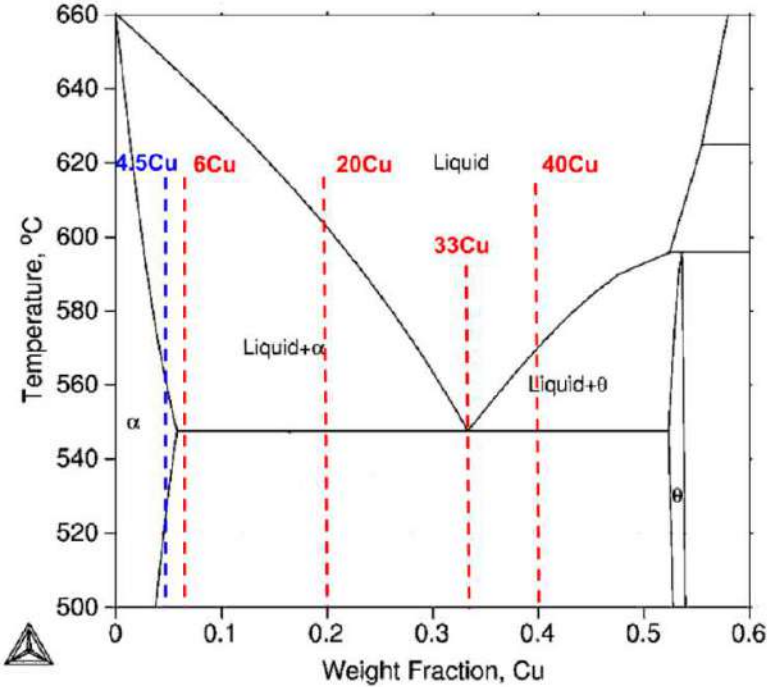

Figure 5.1 Equilibrium phase diagram of the Al-Cu system. Adapted from Ref. [272].

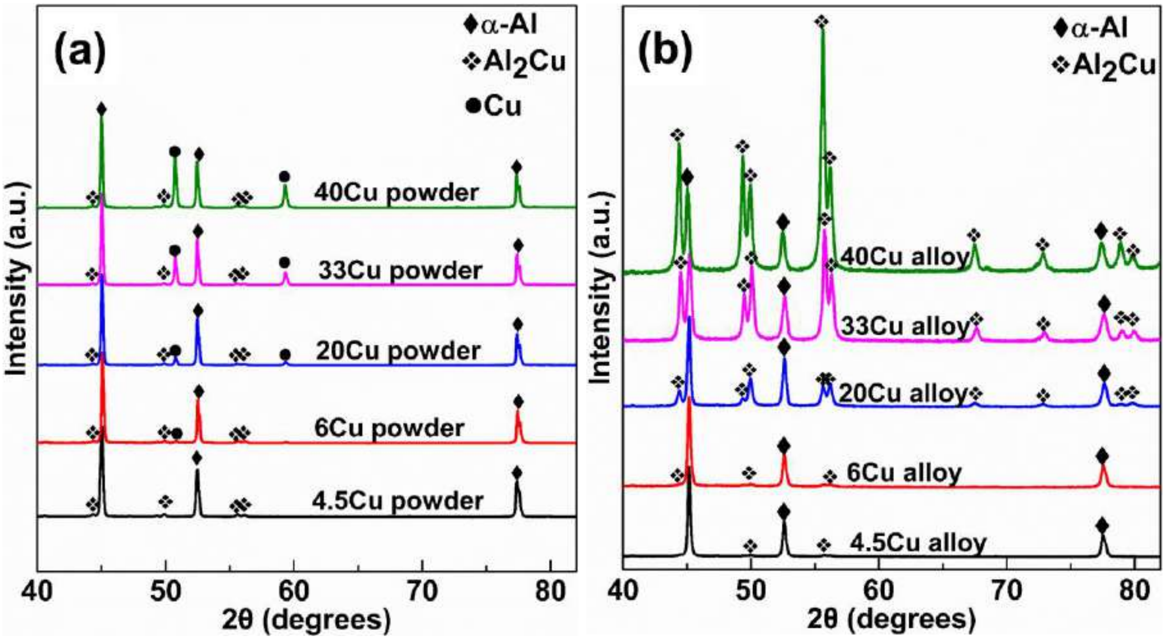

Figure 5.2. XRD patterns of (a) Al-*x*Cu powder mixtures and (b) SLM Al-*x*Cu alloys.

Fig. 5.2(a) shows the XRD patterns of the Al-*x*Cu powder mixtures. After SLM processing (Fig. 5.2(b)), pure Cu is no longer visible, whereas the intensity of the diffraction peaks belonging to Al_2Cu is enhanced significantly, indicating that Cu reacts with the Al-4.5Cu matrix to form Al_2Cu. The solubility limit of Cu in Al is an order magnitude less than that of Al in Cu, hence, the Al(Cu) solid solution is expected to saturate first, resulting in the nucleation of Al_2Cu phase firstly [273,274]. Therefore, the Al_2Cu phase becomes the main phase in these Al-Cu alloys.With increasing Cu content, the amount of Al_2Cu phase in the Al-*x*Cu alloys is 10 wt. %, 14 wt. %, 50 wt. % , 68 wt. % and 77 wt. %, based on a Rietveld refinement using the software X'pert high scores (PANanlytical).

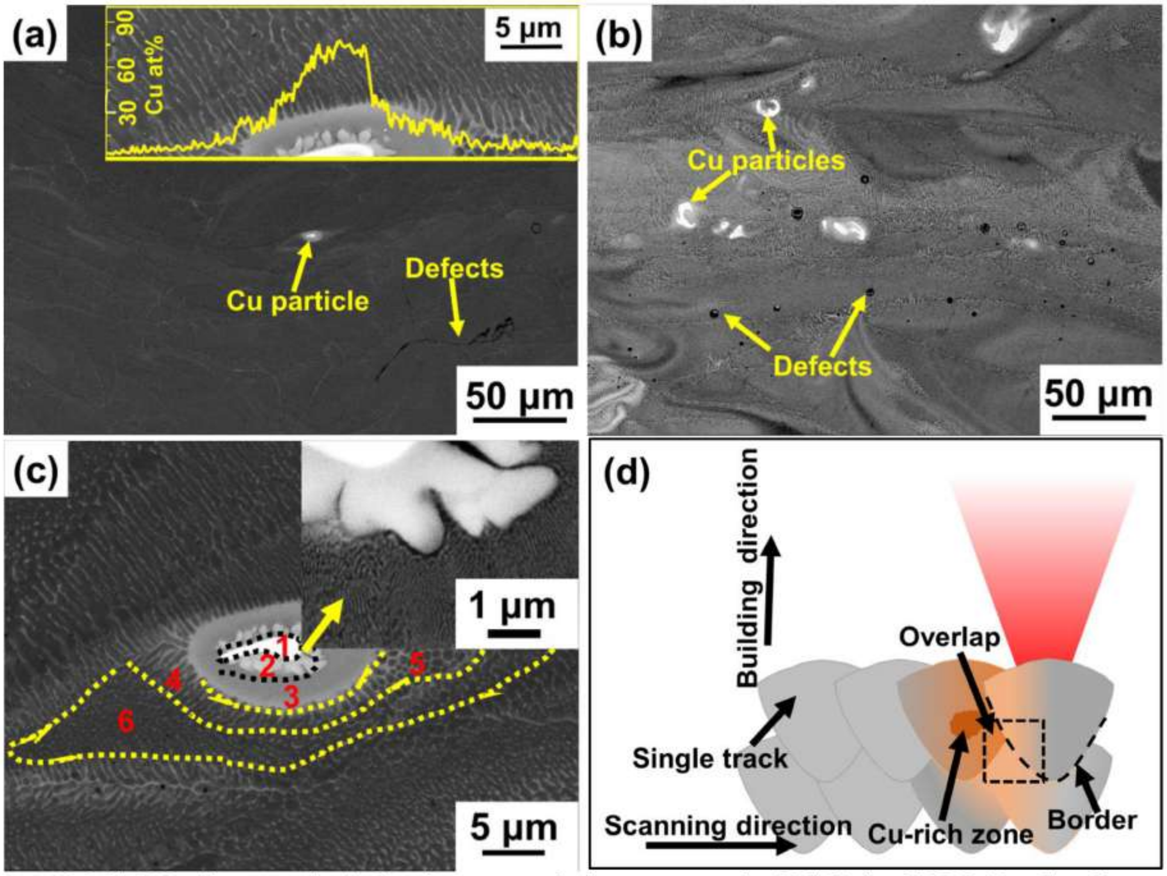

Figure 5.3 SEM micrographs in back-scattered electrons mode (BSE) for SLM Al-*x*Cu alloys: (a) 6Cu alloy (inset-: Cu distribution across the Cu-rich zone); (b) 40Cu alloy; (c) Cu-rich zone in the 6Cu alloy (inset-: high magnification). (d) Schematic illustrating the diffusion of Cu during SLM processing.

Fig. 5.3 shows the effect of Cu on the microstructure of the Al-*x*Cu alloys synthesized by SLM. The morphology of the 40Cu alloy (Fig. 5.3(b)) exihibits more bright Cu-rich zones than the 6Cu alloy (Fig. 5.3(a)), representative of a more inhomogeneous microstruture. The phenomena of the inhomogeneous microstructures have been also found in other alloys prepared by SLM starting from powder mixtures [101,275,276]. In order to explain the formation of the inhomogeneous microstructure, a Cu-rich zone including six zones (Fig. 5.3(c)) is investigated in the 6Cu alloy. The brightest part in Fig. 5.3(c) is named zone *1* which contains 26-45 at. % Al and 55-74 at. % Cu, as analyzed detected by EDS (cf. the inset in Fig. 5.3(a)). The next Cu-rich area (zone *2*) contains 61-63 at. % Al and 37-39 at. % Cu, matching the atomic ratio of Al_2Cu. The inset SEM image in Fig. 5.3(c)) reveals that a nano-eutectic Al-Cu microstructure (zone *3*) is generated next to zone *2*. The further decrease of the Cu content and the decreased cooling rate along the different melting directions [67,85] lead to the fomation of elongated Al_2Cu phase dendritics (zone *4*) and cellular structures (zone *5*) around zone *3*. With further decreasing Cu content (zone *6*), granular Al_2Cu precipitates separate out around the Al matrix.

The Cu diffusion in the Al-Cu alloys during SLM processing is schematically depicted in Fig. 5.3(d). During SLM processing, the Cu powder and the Al-4.5Cu powder are melted locally because the high-energy laser raises the temperature up to 2200 K [17,22]. However, due to the short lifetime of the molten pool ($t < 3$ ms) [65,66], and the limitation of the solute diffusivity in Al ($D_L \approx 3.5 \times 10^{-9}$ m^2/s) [277,278], Cu cannot fully diffuse into the surrounding liquid aluminum matrix. This results in a pronounced Cu gradient near the Cu powders and the formation of zones with different microstructures. As shown in Fig. 5.3(c), the width from the center of zone *1* to the edge of zone *5* (less than 20 μm) provides strong evidence for the limited diffusion of Cu during SLM processing. However, this width is larger than the estimated width (≈ 3 μm, calculated by $\sqrt{D_L t}$). This reveals that although Cu solute diffusion in the Al matrix is limited, the overlaps between tracks generated by remelting provide preferential diffusion paths, which ensures that a certain amount of Cu can diffuse into adjacent areas, as shown in Fig. 5.3(d).

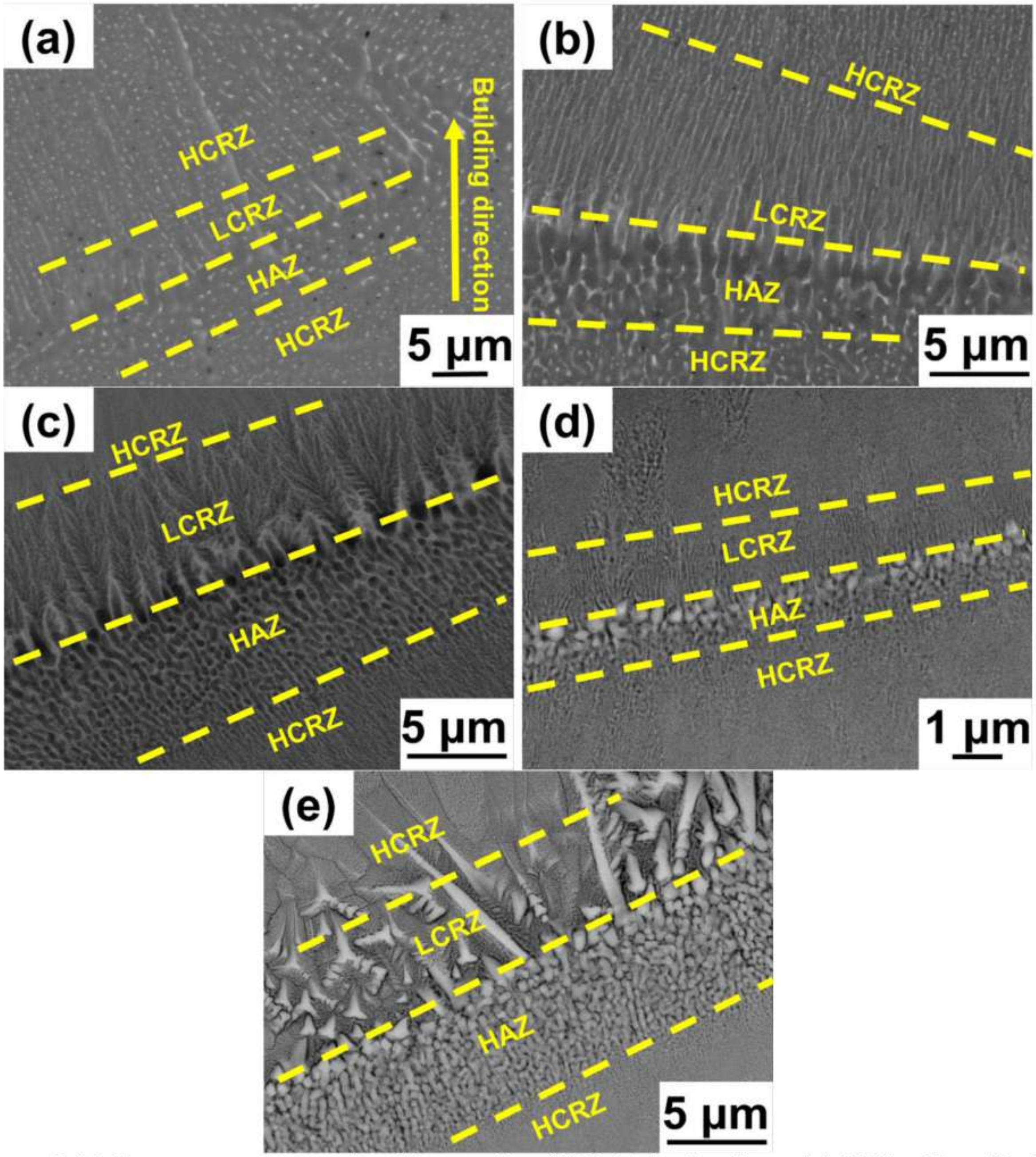

Figure 5.4 Microstructures around melting tracks of SLM Al-*x*Cu alloys: (a) 4.5Cu alloy; (b) 6Cu alloy; (c) 20Cu alloy; (d) 33Cu alloy; (e) 40Cu alloy.

The microstructures around the boundaries of the melting tracks are shown in Fig. 5.4, which confirms the existence of the diffusion through the overlaps. As shown in Fig. 5.4, although the microstructures of the Al-*x*Cu alloys are different, every alloy contains three distinct zones depending on the different microstructure around the boundaries: a high-cooling-rate zone (HCRZ), a low-cooling-rate zone (LCRZ) and a heat-affected zone (HAZ), which is similar to the classification of the SLM AlSi10Mg alloy by Thijs *et al*. [59]. The formation of HCRZ and LCRZ is caused by the increase of the solidification rate from the top of the molten pool to the boundaries along the building direction (shown in Fig. 5.4(d)) [86]. For the 4.5Cu alloy, the Al_2Cu phase is distributed uniformly in the Al matrix as a fine granular microstructure in the HCRZ, whereas the LCRZ displays a fine discontinuous line-like Al_2Cu phase. The HAZ of the 4.5Cu alloy displays a coarse granular microstructure, which is different from the microstructures of HCRZ and LCRZ. Compared with the 4.5Cu alloy, the HCRZ in the 6Cu alloy displays a coarse granular microstructure, whereas the Al_2Cu phase in LCRZ is elongated and shows a continuous line-like shape. The HAZ in the 6Cu alloy displays a discontinuous cellular microstructure, which is even more continuous in the 20Cu alloy. The increase of the Cu content up to 20 wt. % results in the formation of the line-like phase in HCRZ and a dendritic microstructure in LCRZ. For the 33Cu alloy, fine eutectic microstructures (interlamellar spacing of 29 ± 4 nm) and a coarse eutectic microstructure (interlamellar spacing of 69 ± 7 nm) are formed in the HCRZ, together with a narrow LCRZ (around 1μm). As the interlamellar spacing of the eutectics is a direct function of the cooling rate [86,279], the large interlamellar spacing in LCRZ corroborates the assumption of a low cooling rate in this area. The LCRZ and HAZ in the 40Cu alloy display hypereutectic microstructures with lumpish Al_2Cu phase and the HAZ is extended to about 5 μm, while the volume fraction of nano-eutectic microstructures in both HCRZ and LCRZ decrease (Figs. 5.4(c) and (d)).

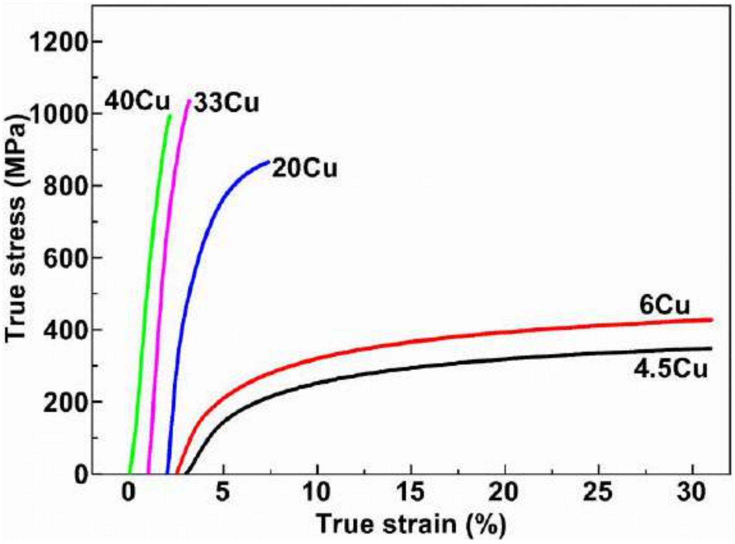

Figure 5.5 Compressive stress-strain curves of the SLM Al-*x*Cu alloys.

Figure 5.5 shows the mechanical properties of the SLM Al-*x*Cu alloys. Due to the increasing volume fraction of the Al_2Cu phase with increasing Cu content, the compressive strength progressively raises, showing the maximum value for the sample with 33 wt. % Cu, but at the expenses of the plastic strain, which decreases significantly. Reduced plasticity compared to the cast counterpart is not uncommon for Al-based alloys processed by SLM unless post heat treatment is used [184]. This is related to the refined and supersaturated structure of the SLM parts [91,184]. However, for net shape components synthesized by additive manufacturing, where metal working and shaping is usually not required, limited plasticity would not radically decrease their application potential but would nevertheless help to reduce the possibility of catastrophic failure under loading. It is striking that the 33Cu and 40Cu alloys exhibit ultra-high compressive strength of about 1000 MPa. Typically, the Al-33Cu alloy has higher strength than Al-Cu alloys with other composition due to the eutectic structure and the compressive failure of these alloys is controlled by the shearmode buckling of the lamellar eutectic structure [280,281]. Hence, the nano-scale eutectic structure is beneficial for improving the compressive strength. The present results are consistent with an early work on Al-33Cu alloys (with relative density exceeding 99 %), which has proven that a similar compressive strength (1.2 ± 0.1 GPa) can be achieved in the presence of a nano-scale eutectic in copper-mold-cast samples [280]. All results indicate that the high Al_2Cu phase content and the larger volume fraction of fine-eutectic structure are responsible for the highest compressive strength observed in the SLM 33Cu alloy.

5.2 SLM TiB_2/Al-Cu-Mg-Si composite

Fig. 5.6 shows the powder mixture of the TiB_2 particles and the Al-Cu-Mg-Si powders. Fine TiB_2 particles are attached to the surface of the Al-Cu-Mg-Si powders; however, the overall morphology of the Al-Cu-Mg-Si powder is not affected by the present powder mixing method (by using a drum hoop mixer described in Section 2.1.2), suggesting that the TiB_2/Al-Cu-Mg-Si composite can be fabricated by SLM using the same processing parameters utilized for the unreinforced Al-Cu-Mg-Si alloy [46, 56].

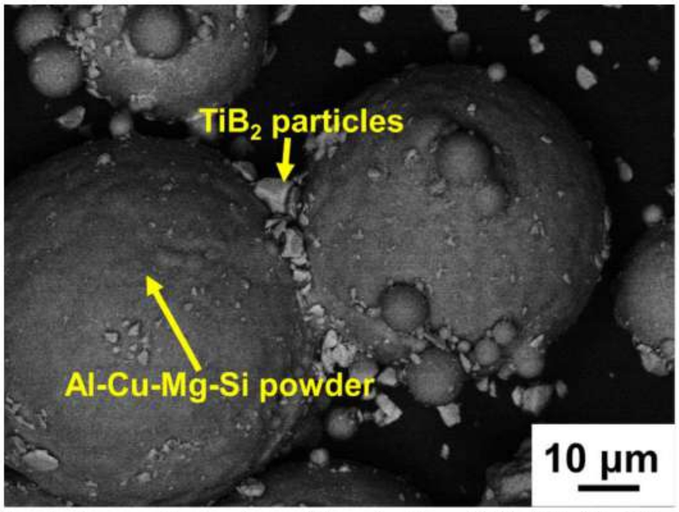

Figure 5.6 Typical morphologies of the starting TiB_2/Al-Cu-Mg-Si powders.

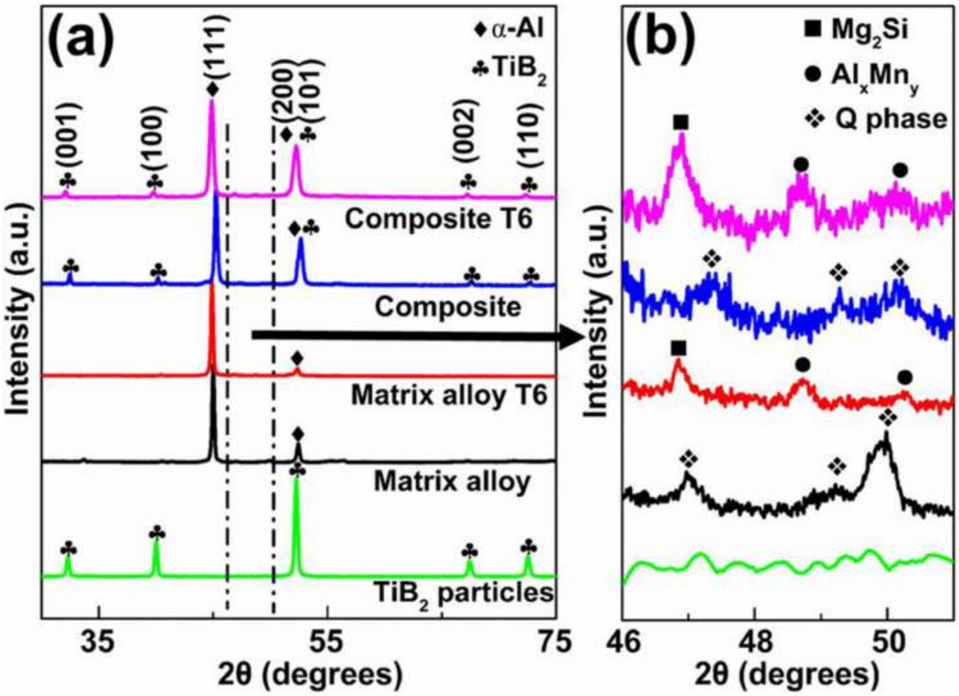

Figure 5.7 XRD patterns of the TiB_2 powder, unreinforced Al-Cu-Mg-Si alloy (matrix alloy) and TiB_2/Al-Cu-Mg-Si composite in both, as-built and heat-treated conditions. (b) Displays the close-up view of the range enclosed by the dashed lines in (a).

Fig. 5.7 shows the phases of the unreinforced Al-Cu-Mg-Si alloy (matrix alloy) and the TiB_2/Al-Cu-Mg-Si composite before and after T6 heat treatment. Comparing the TiB_2/Al-Cu-Mg-Si composite with the Al-Cu-Mg-Si alloy, additional peaks are visible indicating the presence of

TiB_2 particles. The close-up view (Fig. 5.7(b)) of the diffraction patterns between 46 °$\leq 2\theta \leq$51 ° indicates that the Q phase in the TiB_2/Al-Cu-Mg-Si composite transforms into Mg_2Si and Al_xMn_y phases upon T6 heat treatment. This phase transformation is also observed for the Al-Cu-Mg-Si alloy after heat treatment. This demonstrates that due to their chemical inertness in the Al alloys, the introduction of the TiB_2 particles has no remarkable influence neither on the phase formation in the Al-Cu-Mg-Si matrix during the SLM process nor on the phase transformation in the Al-Cu-Mg-Si matrix during T6 heat treatment.

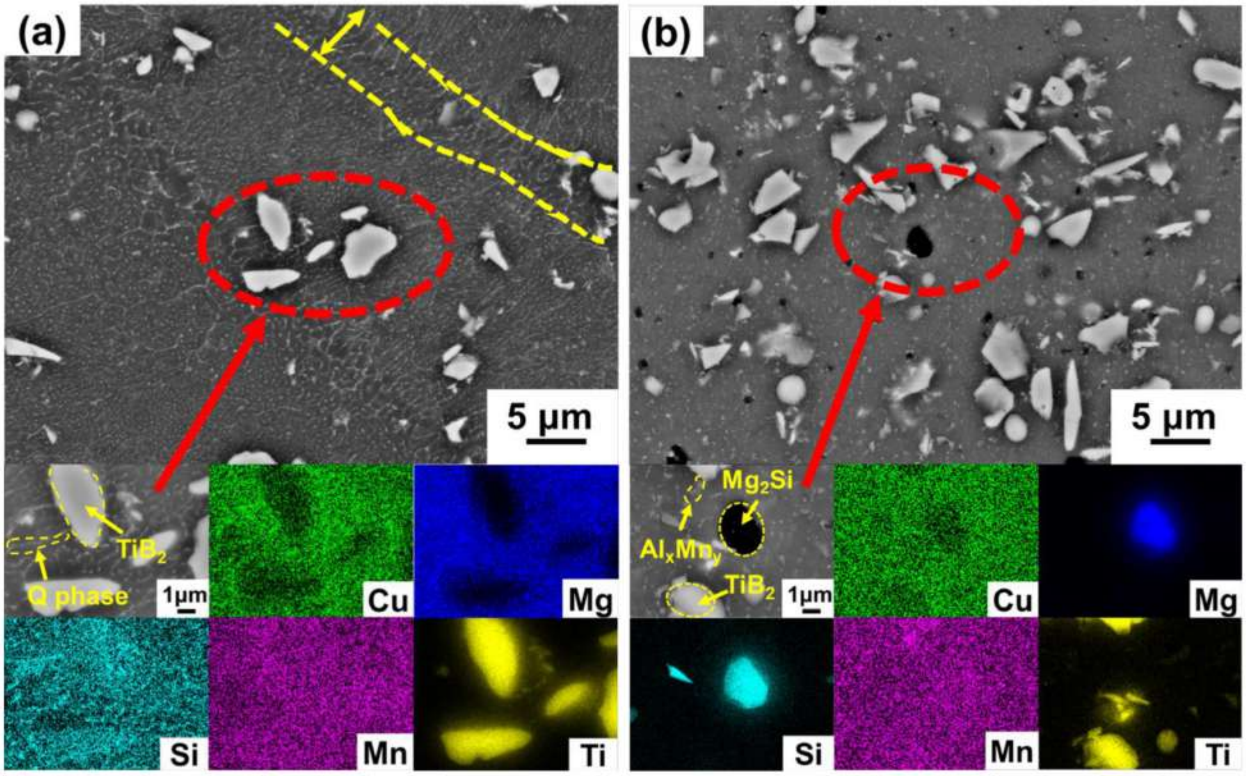

Figure 5.8 SEM micrographs and corresponding EDS maps at high magnification for TiB_2/Al-Cu-Mg-Si composite: (a) TiB_2/Al-Cu-Mg-Si composite, (b) TiB_2/Al-Cu-Mg-Si composite after T6.

Fig. 5.8 shows the microstructures of the TiB_2/Al-Cu-Mg-Si composite before and after T6 heat treatment. The TiB_2 particles are dispersed uniformly in the Al-Cu-Mg-Si matrix without clustering and do not remarkably change the microstructure of the Al-Cu-Mg-Si matrix in the composite. As shown in the area between the yellow dashed lines in Fig. 5.8(a), the sample still exhibits a coarse granular microstructure in the boundary of the melt pools. From the phase analyses of the XRD patterns (Fig. 5.7(b)) and the EDS maps (Fig. 3.5(b)), the granular phase appearing bright in the TiB_2/Al-Cu-Mg-Si composite is still the quaternary Q phase, which contains Al, Cu, Mg and Si. As shown in Fig. 5.8(b), Al_xMn_y and Mg_2Si phases form in the Al-Cu-Mg-Si matrix of the composite in the course of the T6 heat treatment, as it was also observed for the unreinforced Al-Cu-Mg-Si alloy after T6 (described in Chapter 3). The microstructures of the SLM TiB_2/Al-Cu-Mg-Si composite before and after heat treatment indicate that the addition of TiB_2 particles does not affect the phase formation of the Al-Cu-Mg-Si matrix during SLM processing and after T6 heat treatment. This is in contrast to SLM composites containing other reinforcing particles [101,165,202]. For example, due to the reaction of SiC and Al at high temperature (1670 K), the in-situ Al_4SiC_4 phase is formed in the matrix of the SiC/Al-10Si-Mg composite produced by SLM of powder mixtures [45].

Fig. 5.9 displays the EBSD maps for all conditions showing the crystal orientations, the phase distribution and the grain boundaries in the α-Al phase of the TiB_2/Al-Cu-Mg-Si composite before and after T6 heat treatment. Compared to the unreinforced Al-Cu-Mg-Si alloy (shown in Fig. 3.7), there is still no strong texture orientation in the Al matrix of the TiB_2/Al-Cu-Mg-Si composite but the Al matrix shows a significant grain refinement down to a grain size of 2.5 ± 0.1 μm (Fig. 5.9(b1). Even though the T6 heat treatment results in a slight increase in the equivalent grain diameter from 2.5 ± 0.1 μm to 3.3 ± 0.1 μm, a small grain size is retained in the composite (Fig. 5.9(b2). Moreover, similar to the Al-Cu-Mg-Si alloy, the heat treatment has no significant effect on the texture orientation of Al matrix. Again, the Mg_2Si phase is observed in the Al-Cu-Mg-Si matrix only after the heat treatment. Typically, TiB_2 is a suitable reinforcement for grain refinement of Al alloys [212,213,282-284]. Two main reasons may lead to the observed grain refinement: *i)*: under suitable conditions, the TiB_2 particles can react with the Al matrix and a nano-sized interface of $TiAl_3$ of a few atomic layers may form between the TiB_2 particles and the Al matrix [212,213,283]. The $TiAl_3$ crystals surrounding the TiB_2 particles can provide more nuclei for crystal growth than the matrix alloy, eventually promoting a significant grain refinement. However, this reaction not only depends on the reaction condition but also on the activity of the TiB_2 phase [213]. *ii)* Due to a preferable natural stacking sequence of Al atoms on TiB_2 [282], fine TiB_2 particles can also refine the grains of the Al alloys by themselves. Thus, some researchers observed a distinct grain refinement of the Al matrix without seeing a reaction interface between TiB_2 and Al alloys [282,284].

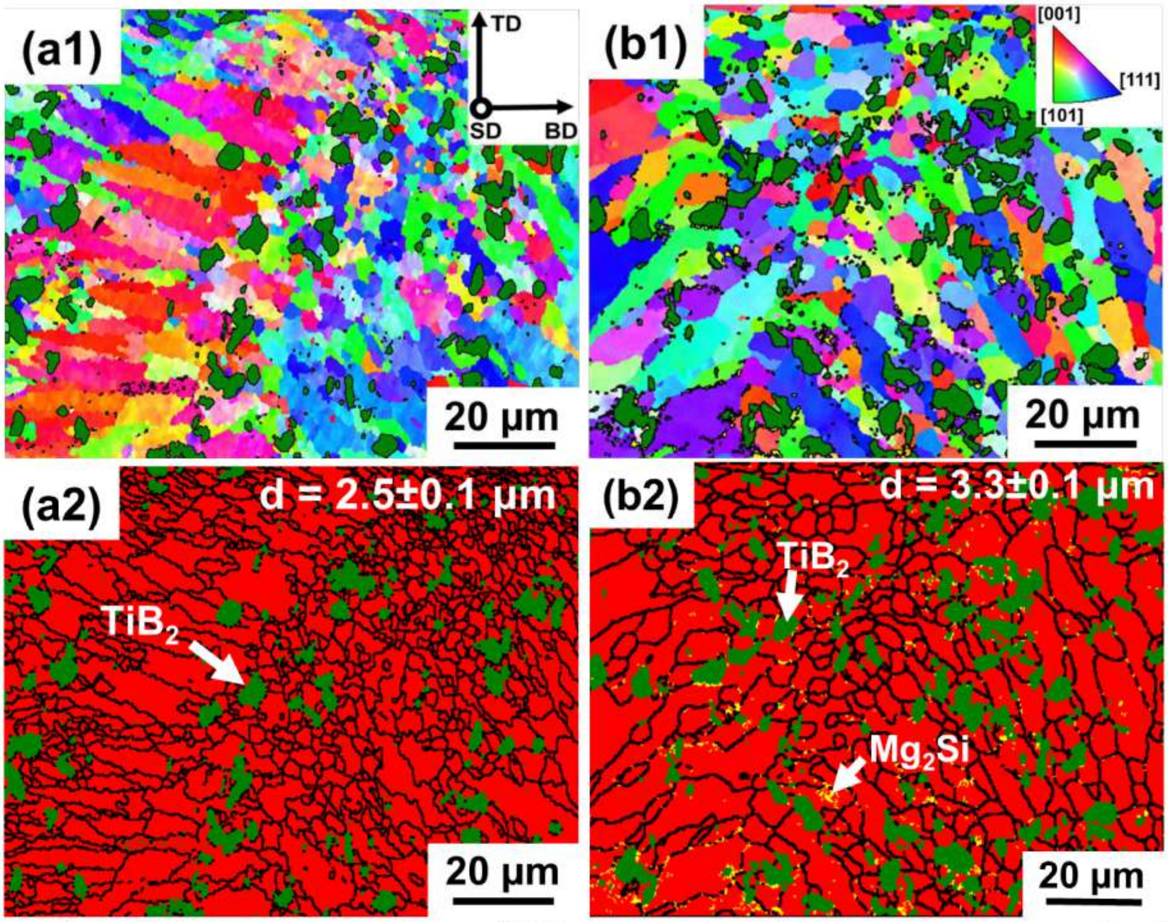

Figure 5.9 EBSD inverse pole figure (IPF) maps: (a1) TiB_2/Al-Cu-Mg-Si composite, (b1) TiB_2/Al-Cu-Mg-Si composite T6. Inset: the spatial orientation with respect to the building direction (BD), scanning direction (SD) and transverse direction (TD); the color code used for the crystal orientation along the building direction. EBSD grain boundary map and combined color phase map of the TiB_2/Al-Cu-Mg-Si composite (inset: equivalent grain diameter of Al): (a2) TiB_2/Al-Cu-Mg-Si composite, (b2) TiB_2/Al-Cu-Mg-Si composite T6. Three phases were distinguished by colors: red (α-Al phase); yellow (Mg_2Si phase); green phase (TiB_2).

Fig. 5.10 shows the bright-field images and SAED patterns of the composites. In contrast to the as-prepared unreinforced Al-Cu-Mg-Si alloy (shown in Fig. 3.8), fewer dislocations are visible in the as-synthesized composite. Martin *et al*. reported that suitable particles can induce heterogeneous nucleation and facilitate equiaxed grain growth, effectively reducing the solidification strain resulting from the high cooling rate during SLM processing [202]. Therefore, the introduction of the TiB_2 particles may also reduce the solidification strain leading to a reduced dislocations density. Moreover, fine grains are present in Fig. 5.10(a). Their size is similar to the grain size (2.5 ± 0.1 µm) determined by the EBSD analysis. As shown in Fig. 5.10(a), there is no indication of any other phase in SAED pattern of TiB_2 phase. This suggests that no visible reaction occurs between the TiB_2 phase and the Al matrix in the as-synthesized SLM composite, implying a good chemical stability of the TiB_2 phase during SLM processing. As shown in Fig. 5.10(b), Mg_2Si and nano-sized $Al_2Cu(Mg)$ precipitates form during the T6 heat treatment, which is also similar to the phase transformation of the SLM Al-Cu-Mg-Si alloy during heat treatment (Fig. 3.8(b)). From the bright-field images and SAED patterns, it can be concluded that the fine grains and the stable TiB_2 phase remain almost unchanged in the Al matrix after T6. Additionally, the SAED patterns in Fig. 5.10(b) also show no indications of significant reaction between the TiB_2 phase and the Al matrix after T6 heat treatment, similar to some early reports [284,285].

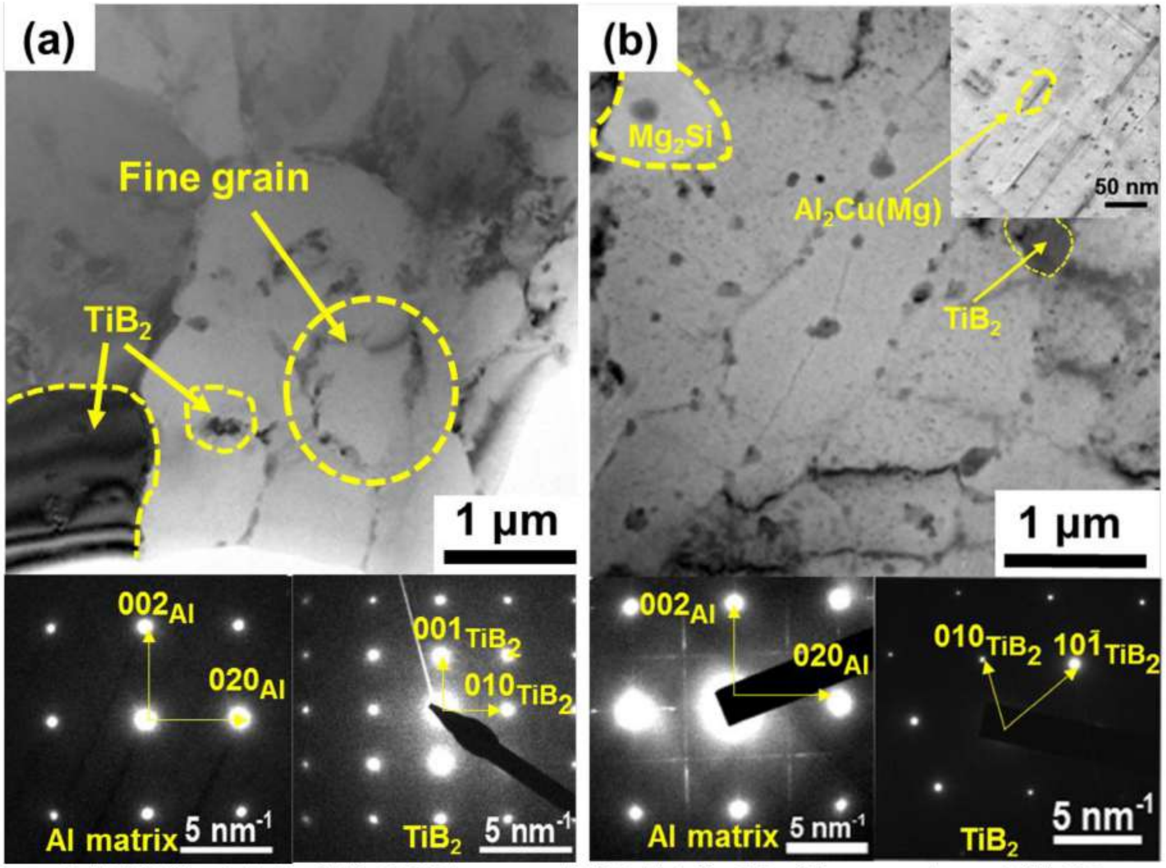

Figure 5.10 $[100]_{Al}$ bright-field TEM images of TiB_2/Al-Cu-Mg-Si composite and SAED patterns of the corresponding phases: (a) overview of the TiB_2/Al-Cu-Mg-Si composite and corresponding SAED pattern of the Al matrix and TiB_2 phase; (b) overview of the TiB_2/Al-Cu-Mg-Si composite T6 and corresponding SAED pattern of the Al matrix and TiB_2 phase (inset: $Al_2Cu(Mg)$ phase at high magnification).

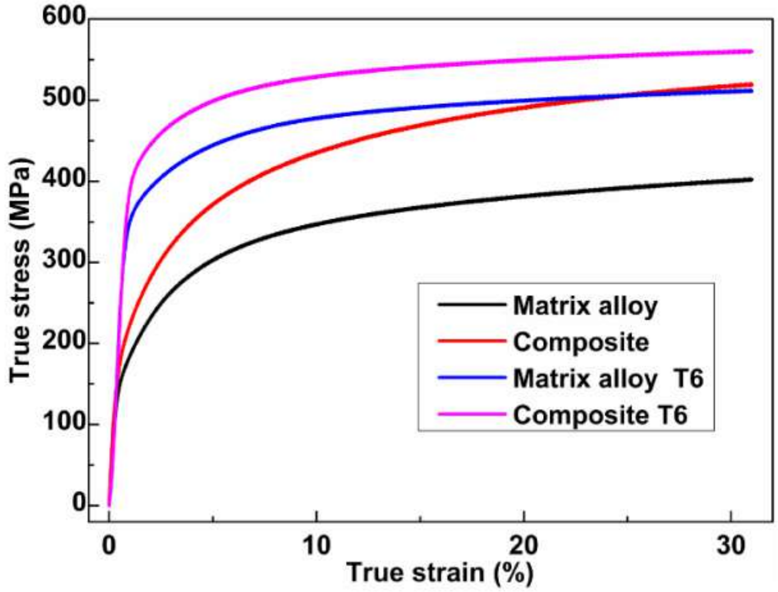

Figure 5.11 Compressive stress-strain curves of the unreinforced Al-Cu-Mg-Si alloy (matrix alloy) and the TiB_2/Al-Cu-Mg-Si composite before and after T6 heat treatment. Curves are only shown up to 30 % of true strain for the sake of clarity, however, none of the samples failed at this point. See text for details.

Table 5.1 Compressive yield strength (0.2 % offset) of the unreinforced Al-Cu-Mg-Si alloy and TiB_2/Al-Cu-Mg-Si composite before and after T6 heat treatment.

SLM materials type	Compressive yield strength	Equivalent grain sizes
Al-Cu-Mg-Si alloy	157 ± 6	23 ± 2
Al-Cu-Mg-Si alloy T6	378 ± 4	30 ± 2
TiB_2/Al-Cu-Mg-Si composite	191 ± 12	2.5 ± 0.8
TiB_2/Al-Cu-Mg-Si composite T6	401 ± 9	3.3 ± 0.4

Fig. 5.11 shows the compressive true stress-true strain curves of the unreinforced Al-Cu-Mg-Si alloy (matrix alloy) and the TiB_2/Al-Cu-Mg-Si composite before and after T6 heat treatment. The corresponding compressive yield strength (0.2 % offset) is listed in Table 5.1. It should be mentioned that none of the specimens fractured up to 60 % strain. However, in order to highlight the yield curves, the strain is only displayed for strains of up to 30 %. The large plastic strain suggests that the TiB_2/Al-Cu-Mg-Si composite in both as-built and heat-treated conditions has plastic deformability similar to that of the unreinforced Al-Cu-Mg-Si alloy. As shown in Table 5.1, the TiB_2/Al-Cu-Mg-Si composite exhibits a higher strength than the Al-Cu-Mg-Si alloy,

irrespective of the condition. It is well known that TiB_2 is a hard phase, which can hinder the propagation of dislocations and enhance grain refinement [212]. Therefore, according to the conventional strengthening mechanisms, the strength improvement of the Al matrix influenced by the TiB_2 phase might mainly result from Orowan strengthening, load-bearing effect (reinforcements can share the applied stress directly by stress transfer from the matrix) and grain refinement strengthening.

The increment of yield strength resulting from Orowan strengthening can be estimated by using Orowan-Ashby equation [286]:

$$\Delta\sigma_{Orowan} = \frac{0.13Gb}{\lambda}\ln\left(\frac{D}{2b}\right) \ , \tag{5.1}$$

where G is the matrix shear modulus (~ 26.2 GPa) [286], b is the Burgers vector (~ 0.286 nm) [286], D is the average diameter of the reinforcement (~ 3 ± 0.5 μm, mentioned in Section 2.1.2), λ is the interparticle spacing and can be expressed as [286]:

$$\lambda = \mathrm{D}\left[\left(\frac{1}{2V_P}\right)^{1/3} - 1\right] \ , \tag{5.2}$$

where V_p is the volume fraction of the reinforcement (~ 5 vol. %).

Combining equations 5.1 and 5.2, the calculated increase of strength resulting from the Orowan strengthening mechanism for the present TiB_2/Al-Cu-Mg-Si composite is 2.4 MPa, which is significantly less than the strength increase observed experimentally (Table 5.1). Therefore, the impact of the Orowan strengthening is not the main factor for the improvement of yield strength of the current composite, which is in good agreement with other reports [287, 288]. Also, the addition of 5 vol. % of particles is lower than the minimum volume fraction required for the strength improvement in many composites, making the effect of load bearing strengthening negligible [289-291].

The strengthening contribution resulting from microstructural refinement, as described by the Hall-Petch equation [286], is commonly described as:

$$\Delta\sigma_{\mathrm{Hall-Petch}} = k\left(d^{-\frac{1}{2}} - d_0^{-\frac{1}{2}}\right) \ , \tag{5.3}$$

where d and d_0 are the grain size of the composite and the unreinforced matrix alloy, respectively. k is the Hall-Petch slope, which is considered to be a measure of the resistance of the grain boundaries to slip transfer. Typically, the Hall-Petch slope (k) of the Al-4Cu alloy is 0.08 MPa·$m^{1/2}$

when only the grain size effect is considered [292,293]. Using the present EBSD results of the equivalent grain size (Table 5.1), in the Al-Cu-Mg-Si alloy and in the TiB_2/Al-Cu-Mg-Si composite (Table 5.1), the values related to grain refinement strengthening for the unreinforced Al-Cu-Mg-Si alloy and TiB_2/Al-Cu-Mg-Si composite before and after heat treatment are 34 MPa and 29 MPa, respectively. This is in good agreement with the experimentally observed differences in yield strength shown in Table 5.1, indicating that grain refinement is the dominant effect for the improved strength of the TiB_2/Al-Cu-Mg-Si composite. Additionally, in contrast to the as-prepared TiB_2/Al-Cu-Mg-Si composite, the formation of nano-precipitates $Al_2Cu(Mg)$ in the heat treated TiB_2/Al-Cu-Mg-Si composite results in a further improvement of the compressive strength due to Orowan strengthening. This strengthening mechanism is the same in the case of the heat treated Al-Cu-Mg-Si alloy as discussed in Chapter 3.

5.3 SLM Al-12Si/Al-Cu-Mg-Si hybrid

Fig. 5.12 displays the microstructures of the SLM Al-12Si/Al-Cu-Mg-Si hybrid alloy. As shown in Fig. 5.12(a), due to etching, there is a visible interface between the two base alloys (indicated by the white dashed lines). No defects are visible in the interface but small pores are present in the base alloys, indicating that the SLM hybrid has a well-bonded center. Fig. 5.12(b) shows the typical cellular microstructure of the Al-12Si fabricated by SLM. At high magnification, the cellular structure is composed of eutectic Al-Si, in agreement with a recent analysis performed by using high resolution transmission electron microscopy [294]. In this zone, the boundary between the neighboring melt pools (area within the black lines in Fig. 5.12(b)) has a width of 3 ± 1 μm and the cell size is 1 ± 0.3 μm, therefore larger than that in the adjacent melt pools (0.3 ± 0.1 μm). The coarse cellular structure in the melt pool boundary can be ascribed to the relatively low cooling rate at the bottom of the melt pool during selective laser melting [238]. The width of the melt pool at the interface (Fig. 5.12(c)) increases to 9 ± 1 μm and the cell size is 3 ± 0.5 μm, which is larger than the cell sizes in the corresponding zone of the Al-12Si part (Fig. 5.12(b)). Moreover, a remarkable heat affected zone with dispersed Si particles is present at the interface (marked by white dashed lines in Fig. 5.12(c)). A typical granular microstructure of the SLM Al-Cu-Mg-Si alloy is shown in Fig. 5.12(d). The details of the microstructure in Fig. 5.12(d), where the fine and coarse phases appear alternately, has been reported in Chapter 3 [46].

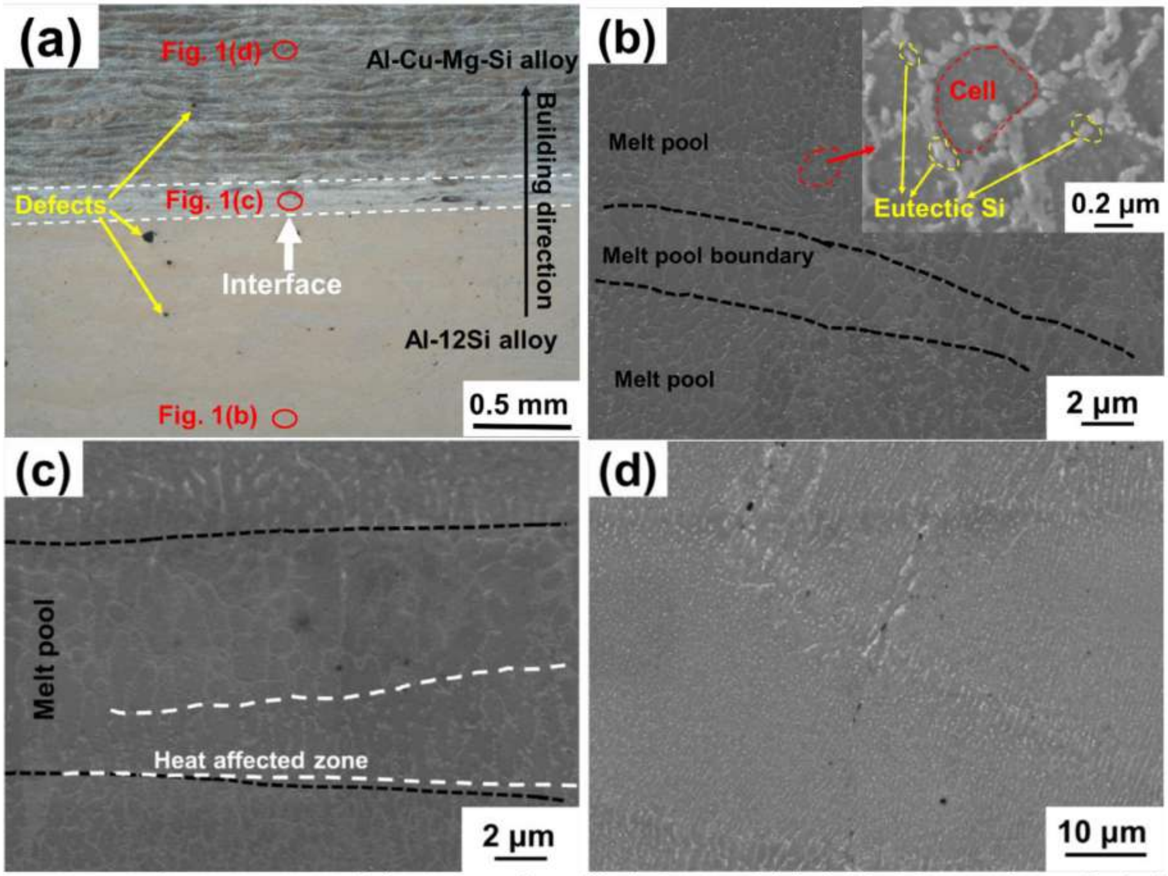

Figure 5.12 Microstructures of the SLM Al-12Si/Al-Cu-Mg-Si hybrid: (a) overview of a hybrid alloy with etching at low magnification (OM); (b) SEM micrograph of Al-12Si part (inset: cellular microstructure at high magnification); (c) interface (SEM); (d) Al-Cu-Mg-Si part (SEM). The position of (b-d) are marked by ellipses in (a).

The relationship between the grain characteristics (crystal orientation and average grain size) and the distance from the interface is depicted in Fig. 5.13. As shown in Fig. 5.13(a), the relative amount of <001> fiber texture around the interface (maximum: 57.1 % at 0.15 mm) is significantly higher than in the zones far away from the interface, and it decreases with the distance from the interface from 0.15 mm to 0.9 mm. The left side of the plot at distances < 0 mm (Al-12Si part) shows the typical grain distribution of the SLM Al-12Si alloy, where fine equiaxed grains and columnar grains form alternately along the building direction [59,124]. The right side (Al-Cu-Mg-Si part) shows the columnar grains, and the average grain size increases along the building direction from 7.9 ± 0.2 μm to 23.3 ± 0.8 μm (Fig. 5.13(b)). The refinement of the grain size and the preferential orientation along the <001> direction at the interface (Figs. 5.13(a) and (b)) point to an obvious chill zone effect, as it has also been reported by Parimi *et al.* for laser fabricated

IN718 [295]. The chill zone effect results from the fact that during the preparation of the Al-Cu-Mg-Si alloy, laser processing provides enough time to allow the complete cooling of the Al-12Si part, which initially acts as an efficient heat sink during the melting of the Al-Cu-Mg-Si alloy, and the grains of the Al-Cu-Mg-Si alloy that have a <100> orientation perpendicular to the top surface of the Al-12Si part grow faster than other less favorably oriented grains. This feature has been widely discussed in the traditional solidification [67,296].

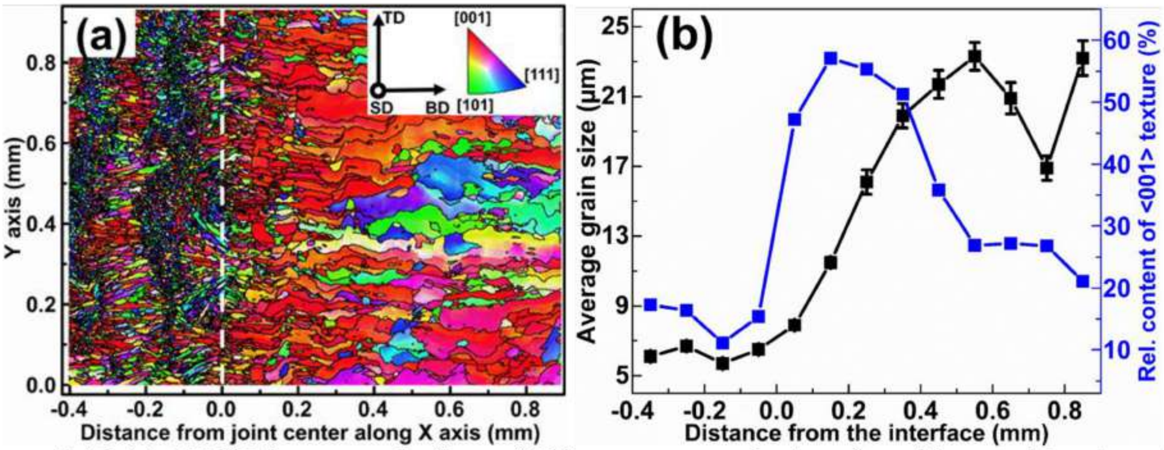

Figure 5.13 (a): EBSD inverse pole figure (IPF) map across the interface. The spatial orientation with respect to the building direction (BD), scanning direction (SD) and transverse direction (TD), and the coloring of the orientation component along the biulding direction in the maps are given in the inset; (b) average grain size and relative content of <001> fiber texture as a function of the disctance from the join center.

The evolution of the microhardness and the content of Si and Cu across the interface from the Al-12Si part to the Al-Cu-Mg-Si part is depicted in Fig. 5.14. The microhardness evolution indicates that there are four different zones (marked as *I*, *II*, *III* and *IV* in Fig. 5.14). In zone *I* (Al-12Si part from -0.6 mm to -0.075mm), the hardness is 137 ± 2 $\mathrm{HV}_{0.05}$, i.e. similar to Al-12Si specimens (138 ± 1 $\mathrm{HV}_{0.05}$). In zone *II* (-0.075 mm to 0.075 mm), the hardness decreases significantly to 125 ± 1 $\mathrm{HV}_{0.05}$ at the 0 mm position. Because the processing parameters of the Al-Cu-Mg-Si alloy are different from those of the Al-12Si alloy at zone *I.* The influence of the parameters on the corresponding microhardness of the interface has to be considered. Due to the different processing parameters of the Al-12Si alloy and Al-Cu-Mg-Si alloy, the influence of the parameters on the corresponding microhardness of the interface has to be considered. The volume-energy density has a significant relationship with the processing parameters as shown in equation

1.1. The volume-energy density used for fabricating the Al-12Si part (40 J/mm^3) at zone *I* is lower than that employed in zone *II* (360 J/mm^3). Considering the influence of volume-energy density on the hardness and microstructure of the top layers of the Al-12Si parts at the interface, Ref-Al-12Si specimens (mentioned in Section 2.1.1) were also fabricated with the optimized parameters of SLM Al-Cu-Mg-Si alloy. The hardness of the Al-12Si specimens with the optimized parameters of SLM Al-12Si alloy (138 ± 1 $HV_{0.05}$) is higher than the Ref-Al-12Si specimens (127 ± 1 $HV_{0.05}$) produced with the low laser power and slow scanning speed corresponding to the high volume-energy density. The same phenomena have also been reported for SLM-processed Al-10Si-Mg [38] and Al-50Si alloys [119]. In general, the high power and fast scanning speed can result in a high cooling rate, contributing to a small cell size in the SLM-processed Al-Si alloys [82,294]. Furthermore, the cell size is an important factor affecting the mechanical properties of SLM alloys with cellular structure, such as Al-12Si, 316L stainless steel and Al-10Si-Mg [142]. Due to Hall-Petch strengthening and the high dislocation density around the cellular walls [82,142], SLM alloys with small cell sizes can reach higher microhardness [142,297]. As shown in Figs. 5.12(b) and (c), the cell size of the melt pool (0.3 ± 0.1 μm) at zone *I* is smaller than the cell size (3 ± 0.5 μm) at zone *II*, while the microhardness at zone *I* is higher than that zone *II* (Fig. 5.14). The above discussion indicates that the re-melting of the top surface of the SLM Al-12Si part subjected to a lower power input and scanning speed can result in the formation of larger cells, leading to the decrease of the hardness in the Al-12Si part around the interface.

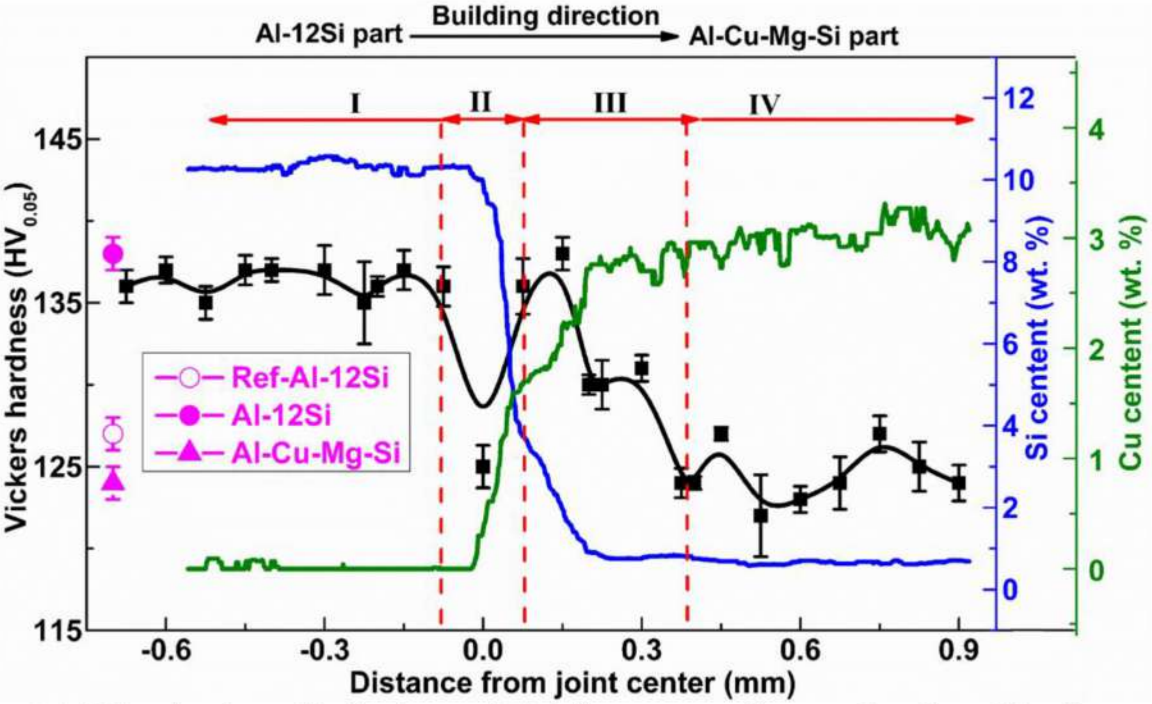

Figure 5.14 Microhardness distribution and EDS line-scan profiles as a function of the distance from the interface.

It is striking that there is a sudden increase of the hardness between zones *II* and *III*. As shown in Fig. 5.12(c), in this zone the microstructure changes from cellular to granular. Therefore, the increase of the hardness from zone *II* to *III* may result from the formation of new phases in the Al matrix, which is different from the eutectic Si of the cellular structure. In the Al-Cu-Mg-Si alloy, the change of Si/Cu ratio can affect the types of the dispersed phases and the corresponding microhardness of the alloys [198,298]. Therefore, this phenomenon will be further analyzed later via the atomic content of Si/Cu and microstructure.

In zone *III* the hardness decreases gradually from 136 ± 2 to 124 ± 1 $HV_{0.05}$ when moving from 0.075 mm to 0.4 mm distance from the interface of the basemetal. According to the measurement of the evolution of Si and Cu contents in zone *III*, Si decreases from 3.7 ± 0.1 wt. % to 0.7 ± 0.1 wt. % from 0.075 mm to 0.4 mm distance from the interface. Conversely, the Cu increases significantly from 1.7 ± 0.1 wt. % to 3.0 ± 0.1 wt. % from 0.075 mm to 0.4 mm distance from the center. Montero Sistiaga *et al*. reported that the addition of Si has a significant influence on the grain refinement of SLM Al alloys [124]. As shown in Figs. 5.13(b) and 5.14, in zone *III*, the Si content decreases from 3.7 ± 0.1 wt. % to 0.7 ± 0.1 wt. % and the grain sizes increases from 11.5

± 1.1 µm to 19.9 ± 2 µm. According to the Hall-Petch relationship observed for nanostructured Al-Cu alloys [292], the increase of the grain size in zone *III* can reduce the hardness of Al alloy. Moreover, the variation of the mechanical properties of Al-Cu-Mg-Si alloys is a direct function of the solid solubility of Si, thus the decreasing Si also can result in a decrease of the hardness [102,124,222].

In zone *IV* (0.4 mm to 0.9 mm), the hardness value fluctuates around 124 ± 2 $HV_{0.05}$, similar as for the SLM Al-Cu-Mg-Si alloy (124 ± 1 $HV_{0.05}$). The affected zone (size of zones *II* and *III* ≤ 0.5 mm) in the present SLM Al-12Si/Al-Cu-Mg-Si hybrid is narrower than for conventional hybrid alloys [216, 219]. In general, hybrid alloys fabricated by conventional method often exhibit affected zones of millimeter size (>> 1 mm), such as the nugget zone, the heat affected zone, thermo-mechanically affected zone or fusion zone, which can be easily observed by optical microscopy [223,299].

Due to the influence of the Si/Cu ratio on phase formation and microhardness of the Al-12Si and Al-Cu-Mg-Si alloys [124,222,239], the morphologies of the secondary phases and the Si and Cu atomic concentrations of the dispersed phases in selected areas have been further investigated at high magnification (Fig. 5.15). It should be mentioned that even though the measurement of the atomic concentrations under the present SEM conditions cannot be highly accurate due to the nano-scale size of the precipitates, the results of the atomic concentrations can still give a certain qualitative understanding of the evolution of the precipitates. Fig. 5.15(a) shows that there is almost no Cu (8.2 ± 0.2 at. % Si and 0.0 ± 0.0 at. % Cu) presenting in the typical cellular structure and there is no obvious enrichment of Cu in the corresponding EDS maps at -0.2 mm distance from the interface (Al-12Si part). As shown in Fig. 5.15(b), there is a clear interface, where the microstructure changes from cellular to granular. The cellular structure composed of the eutectic Si s is only found at the Al-12Si side of the interface (6.8 ± 0.8 at. % Si and 0.5 ± 0.1 at. % Cu). At the Al-Cu-Mg-Si side of the interface (Fig. 5.15(b)), the cellular microstructure suddenly changes to granular and a distinct enrichment of Cu and depletion of Si are observed (4.2 ± 0.1 at. % Si and 1.9 ± 0.3 at. % Cu). The EDS maps and the atomic concentrations of Si and Cu (Figs. 5.15(c)) at 0.2 mm distance from the center reveal a remarkable increase of Cu and a reduction of Si (1.0 ± 0.1 at. % Si and 3.9 ± 0.4 at. % Cu).

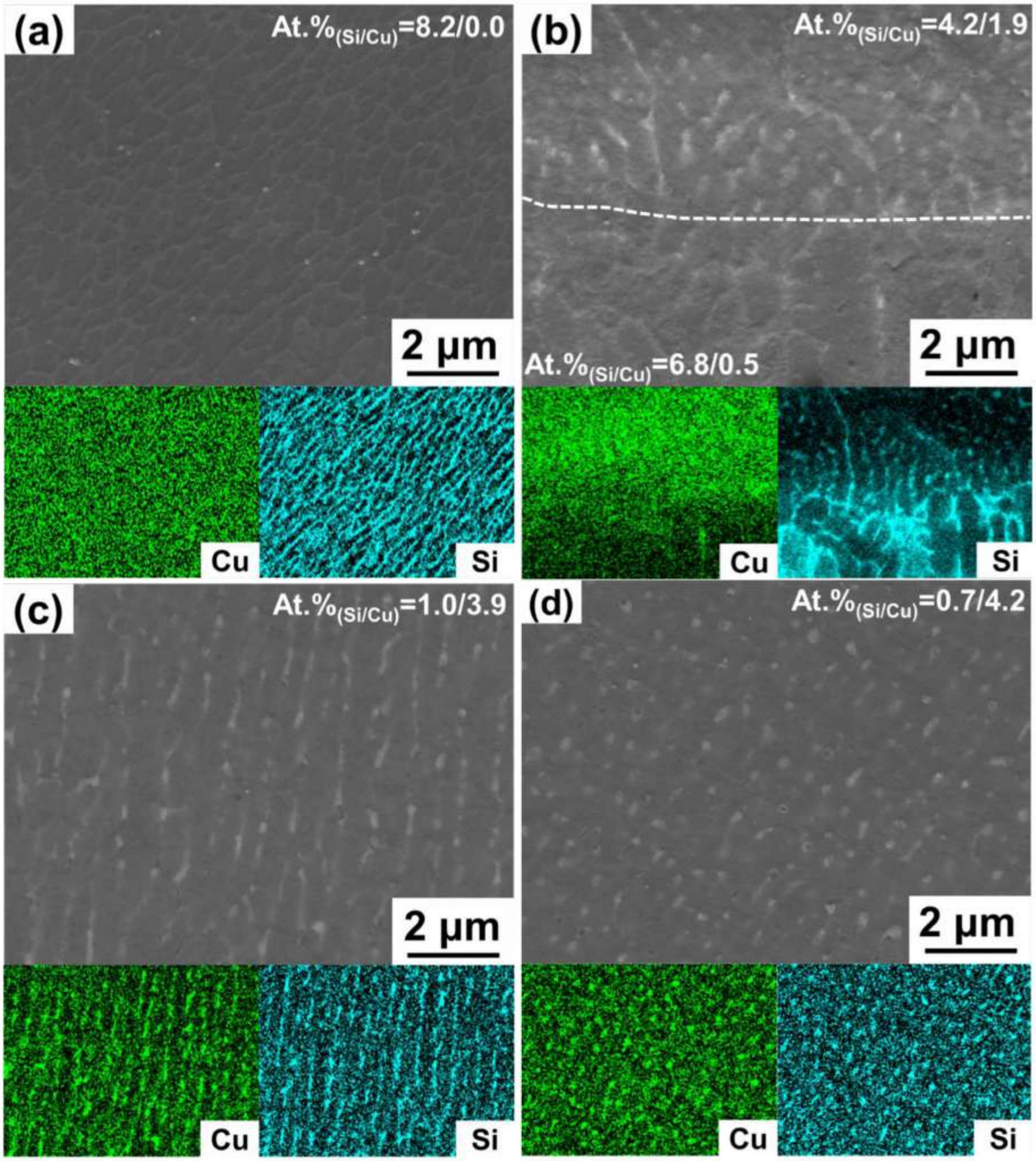

Figure 5.15 SEM micrographs and EDS maps at different distances from the interface along the building direction: (a) -0.2 mm, (b) 0 mm, (c) 0.2 mm, (d) 0.4 mm. (inset: Si and Cu atomic concentrations of the dispersed phases in the Al matrix)

Combining the analyses of the microstructures and the chemical composition of the phases in zones *II* and *III*, these results provide evidence for the phase evolution from a eutectic Si to a granular phase (containing Si and Cu). It indicates that the formation of the new phase cause the sudden increase of the hardness from zone *II* and *III*. As shown in Figs. 5.15(d), the granular phases at the 0.4 mm position have 0.7 ± 0.1 at. % Si, which is similar to the Si content of the Al-Cu-Mg-Si alloy (0.7 ± 0.1 at. % Si). It is clear that the diffusion of Si stops at a distance of about 0.4 mm from the interface. Even though the microstructures and the atomic concentration of Si and Cu at 0.2 mm distance from the center is similar to that at 0.4 mm, the microhardness at 0.2 mm is dramatically higher. The similar microstructures but different hardness in zone *III* imply that the unrecognizable variation of phase composition has an effect on the hardness of this zones [300,301], similar to the precipitate free zone (PFZ) existing in the conventional hybrid materials [302-304]. Unfortunately, zone *III* is too small for identifying the phases unambiguously with the experimental tools used in this study. In order to highlight the feature of almost identical microstructures and hardness evolution in zone *III*, which is similar to the other Al dissimilar materials [300,302], the zone *III* is termed precipitate-free zone.

Depending on the above analysis of microstructures and hardness evolution, the four zones in Al-12Si/Al-Cu-Mg-Si hybrid alloy along the building direction can be regarded as Al-12Si zone, interface, precipitate-free zone (PFZ) and Al-Cu-Mg-Si zone, respectively.

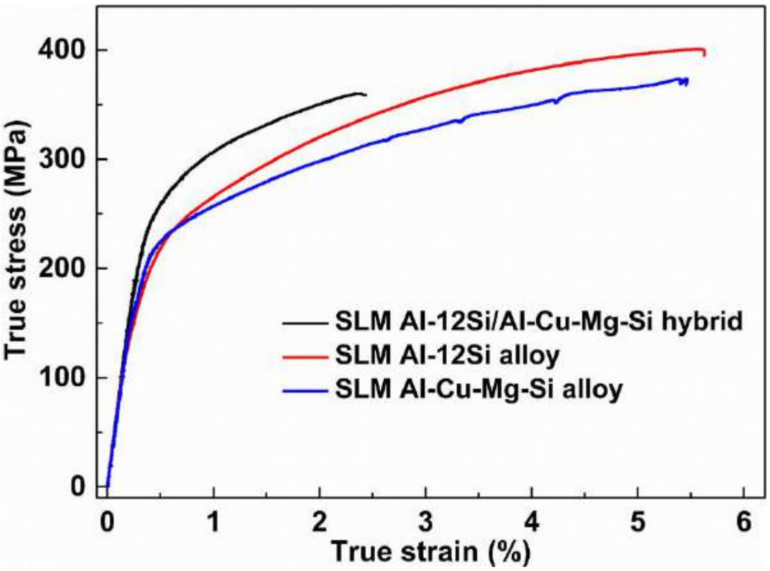

Figure 5.16 Tensile stress-strain curves of the Al-12Si/Al-Cu-Mg-Si hybrid alloy, SLM Al-12Si alloy and SLM Al-Cu-Mg-Si alloy.

Characteristic room temperature tensile curves of the Al-12Si/Al-Cu-Mg-Si hybrid alloy, Al-12Si and Al-Cu-Mg-Si specimens are shown in Fig. 5.16, and their tensile results are listed in Table 5.2. The SLM hybrid has a higher yield strength (267 ± 10 MPa) but lower elongation (2.6

± 0.1 %) than the two SLM Al-12Si and Al-Cu-Mg-Si base alloys. Due to the different zones with different microstructures and mechanical properties (Fig. 5.14), the heterogeneous stress distribution in the different zones under the tensile conditions is different, resulting in that the hybrid alloys fail early and their ultimate tensile strength (UTS) is lower than for the base alloys [305,306].

The YS and UTS of the Al-12Si/Al-Cu-Mg-Si hybrid reach or even exceed the properties of 2xxx, 4xxx and 6xxx hybrids fabricated by conventional welding technologies [219]. This reveals that selective laser melting is suitable for the joining of dissimilar materials.

Table 5.2: Comparison of the tensile properties of the SLM Al-12Si/Al-Cu-Mg-Si hybrid alloy, SLM Al-12Si alloy and SLM Al-Cu-Mg-Si alloy.

Materials type	YS (MPa)	UTS (MPa)	Elongation (%)
Al-12Si/Al-Cu-Mg-Si hybrid alloy	267 ± 10	369 ± 15	2.6 ± 0.1
Al-12Si alloy	208 ± 8	403 ± 4	5.6 ± 0.3
Al-Cu-Mg-Si alloy	222 ± 2	372 ± 7	5.8 ± 0.5

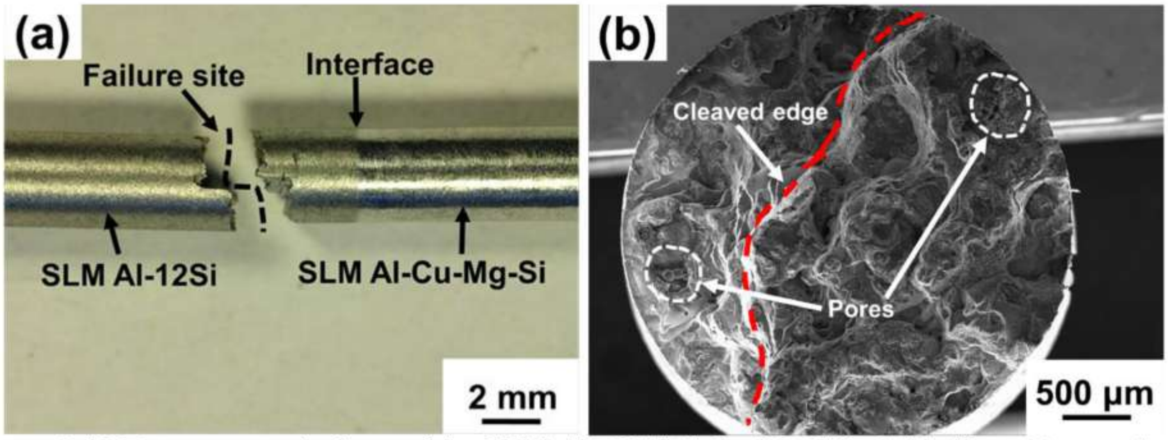

Figure 5.17 Fracture morphology of the SLM Al-12Si/Al-Cu-Mg-Si hybrid alloy: (a) overview of the fracture site along the building direction (OM), (b) SEM micrograph of the fracture morphology

Fig. 5.17 displays the fracture morphology of the SLM Al-12Si/Al-Cu-Mg-Si hybrid alloy. The overview (Fig. 5.17(a)) at the fracture site along the building direction was observed by optical microscopy. The failure site is at the Al-12Si part, at about 2 mm distance from the interface, thus rather far away from the interface. The fact that the fracture occurs at the Al-12Si part points to a good interface. There is no recognizable necking but brittle fracture at the failure site, which is consistent with the low elongation (2.6 ± 0.1 %). In general, defects, mainly pores, developing during SLM processing cannot be completely avoided, and these defects have a stronger effect on the failure under the heterogeneous stress distribution of the hybrid alloys [217]. Due to the better damage tolerance of the Al-Cu-Mg-Si alloy compared to Al-12Si [173,225], pores have a more significant effect on the fracture of the Al-12Si base alloy than for the Al-Cu-Mg-Si base alloy. The failure at the Al-12Si part and the pores on the fracture surface (Figs. 5.17(a) and (b)) provide evidence for the above analysis.

CHAPTER 6

Summary and Outlook

In this thesis, the densification, heat treatment, microstructure, mechanical properties, tribological and corrosion properties of SLM heat treatable Al-3.5Cu-1.5Mg-1Si alloy were investigated systematically. The following results are achieved:

- Densification of the Al-Cu-Mg-Si alloy: the results indicates that a lower power (*P*: around 200 W) and low scanning speed (v_s: around 200 mm/s) should be selected to avoid the formation of defects (mainly pores and cracks) and to achieve fully dense SLM Al-3.5Cu-1.5Mg-1Si alloy and its related materials.
- Microstructure of the Al-Cu-Mg-Si alloy before and after T6 heat treatment: the microstructures in the individual melt-pool and microstructures in the area between tracks can be distinguished easily in the as-prepared SLM Al-Cu-Mg-Si alloy, where the Q phase is dispersed in the Al matrix. After T6 heat treatment, the Q phase transforms to the Mg_2Si, Al_xMn_y phases and nano-$Al_2Cu(Mg)$ precipitates. In addition, T6 heat treatment causes the microstructural differences and micro-grains between the tracks in the as-prepared specimens to disappear, and the average size of columnar grains in the heat treated specimen increases slightly.
- Mechanical properties and fracture morphologies of the Al-Cu-Mg-Si alloy before and after T6 heat treatment: Due to generation of nano-$Al_2Cu(Mg)$ precipitates in the Al matrix, the heat treated SLM alloys show an increased yield strength (YS) and ultimate tensile strength (UTS) compared with the as-prepared specimens. The as-prepared Al-Cu-Mg-Si samples show a YS of 222 ± 2 MPa and an UTS of 372 ± 7 MPa along with an elongation of 5.8 ± 0.5 %. After heat treatment, both the YS and UTS increase to 433 ± 4 MPa and 512 ± 5 MPa respectively, but the elongation (6.5 ± 0.4 %) does not change significantly. All the SLM Al-3.5Cu-1.5Mg-1Si samples fail around defects and show intergranular fracture along the columnar grains.
- Tribological properties of the Al-Cu-Mg-Si alloy: due to the fine phases generated during SLM processing, the SLM Al-Cu-Mg-Si alloys before and after heat treatment both have a better specific wear rate and average of coefficient of friction (COF) than conventional

AA2024 alloys at the same heat treatment condition. The morphologies after the wear test of SLM alloys both show a typical plastic deformation with the slim grooves, indicating the occurrence of an abrasive mechanism.

- Corrosion properties of the Al-Cu-Mg-Si alloy: as a comparison, the SLM Al-Cu-Mg-Si alloys before and after heat treatment with a lower corrosion rate show a better corrosion resistant than the AA2024 alloys. However, the corroded SLM alloy with and without heat treatment displays a serious exfoliation phenomenon, not a pitting around the intermetallic phases like the AA2024 alloy. It indicates that the SLM alloys have a different corrosion mechanism with respect to the AA2024 alloy.

Moreover, the thesis also covers the SLM processing, microstructure and mechanical properties of Al-*x*Cu ($x = 4.5$, 6, 20, 33 and 40 wt. %) alloys of powder mixture, TiB_2/ Al-3.5Cu-1.5Mg-1Si composites and Al-12Si/Al-3.5Cu-1.5Mg-1Si hybrid materials. The results obtained from the investigation of these materials can be summarized as below:

- SLM Al-*x*Cu (x = 4.5, 6, 20, 33 and 40 wt. %) alloys of powder mixture: With increasing Cu content, the microstructure of the Al-*x*Cu changes from the micro-segregated (Al-6Cu), to hypoeutectic (Al-20Cu), to near-eutectic (Al-33Cu), and to hypereutectic (Al-40Cu) microstructures as in the Al-Cu phase diagram. This indicates that due to the diffusion of introduced alloying elements and its reaction with the raw materials during SLM processing, the use of powder mixtures is a possible way to design novel SLM materials. However, it also suggests that SLM composites should be designed carefully, as this reaction and diffusion in the processing of the composites can significantly result in the change of the properties of the matrix.
- SLM TiB_2/Al-3.5Cu-1.5Mg-1Si composite. The microstructure of the Al matrix, which is related to the high cooling rate and thermal gradients typically present during SLM processing, is retained in the as-built composite. The phase distribution and phase transformation of the Al matrix in the TiB_2/Al-Cu-Mg-Si composite are the same as observed in the unreinforced Al-Cu-Mg-Si alloy, both before and after T6 heat treatment. A granular Q phase is dispersed in the Al matrix, which in the course of the heat treatment transforms to Al_xMn_y, Mg_2Si and $Al_2Cu(Mg)$ nano-precipitates. The addition of 5 vol. % TiB_2 significantly refines the grains of the matrix: the grain size decreases from 23 ± 1 µm and 30 ± 3 µm for the unreinforced Al-Cu-Mg-Si alloy before and after the heat treatment, respectively, to 2.5 ± 0.1 µm and 3.3 ±

0.1 μm in the composite. The grain refinement results in a significant improvement of the compressive yield strength of the TiB_2/Al-Cu-Mg-Si composite before and after heat treatment. Moreover, due to the formation of Al_2Cu(Mg) nano-precipitates during the heat treatment, the heat-treated TiB_2/Al-Cu-Mg-Si composite exhibits an enhanced compressive strength resulting from Orowan strengthening.

- SLM Al-12Si/Al-3.5Cu-1.5Mg-1Si hybrid alloys: the successful fabrication of the Al-12Si/Al-Cu-Mg-Si alloy paves the way for the investigation and application of the SLM hybrid materials. The SLM hybrid alloy shows a narrow and good interface between the two base alloys. There are four zones displayed in the hybrid alloys: the Al-12Si zone, the interface, the precipitate free zone and the Al-Cu-Mg-Si zone. The interface zone (< 0.2 mm thick) displays a sudden change of the microstructure from cellular to granular, resulting in the low hardness. The precipitate free zone (< 0.3 mm thick) shows an almost homogenous microstructure and a similar elemental composition of the secondary phase but a remarkable variation of the hardness. EBSD analysis shows that the grains are refined around the center of the hybrid but grow gradually from the interface to the Al-Cu-Mg-Si zone along the building direction. Additionally, a strong <100> fiber texture develops around the interface and disappears gradually along the building direction. The hybrid alloy exhibits a room temperature yield strength of 267 ± 10 MPa and an ultimate tensile strength of 369 ± 15 MPa with an elongation of 2.6 ± 0.1 %, revealing an effective potential of selective laser melting in the field of hybrid materials.

These new conclusions obtained in the present thesis not only verify the old phenomena observed in the past also give a guide for the SLM processing of other Al alloys, especially Al-Zn series alloys. According to the analysis of the microstructure, mechanical properties, tribological and corrosion properties of the Al-Cu-Mg-Si alloy before and after heat treatment, it suggests that due to the non-equilibrium solidification during SLM processing, the properties of the Al-Cu-Mg-Si alloy achieve or even exceed the performance of the corresponding commercial Al alloys. Moreover, novel materials, such as the TiB_2/Al-3.5Cu-1.5Mg-1Si composite and Al-12Si/Al-3.5Cu-1.5Mg-1Si hybrids, can be designed and fabricated by selective laser melting, which also display good mechanical properties. In the near future, the systematic and comprehensive findings in the thesis can give a guide for the design and investigation of SLM materials focused on by engineers, physicists and material scientists.

Although the heat treatable Al-3.5Cu-1.5Mg-1Si alloy, SLM Al-*x*Cu (x = 4.5, 6, 20, 33 and 40 wt. %) alloys, TiB_2/Al-3.5Cu-1.5Mg-1Si composite and Al-12Si/Al-3.5Cu-1.5Mg-1Si hybrid alloys were fabricated successfully and also show good mechanical properties, some in-depth issues still need more work to figure out the following aspects:

- For the heat treatable Al-Cu series alloys fabricated by SLM, the high cooling rate during the processing results in the fine secondary phases disperse in the Al matrix, which is different from the Al-Cu series fabricated by conventional cast method. This different microstructure of SLM Al-Cu series alloys from their corresponding alloys may lead to the change of heat treatment process and mechanical properties on the same heat treatment condition. For the industrial application of SLM Al-Cu series alloys, it is thus necessary to investigate this change resulting from the microstructures.
- Powder mixture is a good way to design the composition of SLM alloys and to synthesize new materials by SLM. But how to control the reaction of additional materials and host materials and get a homogeneous microstructure of the new SLM materials is the important issue.
- For the TiB_2/Al-3.5Cu-1.5Mg-1Si composite, how to explain the grain refinement resulting from the addition of TiB_2 which occurs at a high cooling rate, is a tough challenge. We not only need to investigate the effect of TiB_2 particles on the solidification and nucleation of the Al matrix during SLM processing, but also we have to study the wetting behavior and interfacial interactions of reinforcement and matrix. This aspect needs the combination of numerous experiments, theory and numerical simulations to clarify this phenomenon.
- For the hybrid materials fabricated by SLM, this is a novel topic. Our work indicates that the SLM hybrid materials have a narrower heat affected zone (micron scale) than the hybrids fabricated by conventional method (millimeter scale). Therefore, this feature results in not only a good mechanical properties of SLM hybrids, but also a difficult analysis on the variation of the microstructure around the heat affected zoon. The future work about the SLM hybrid will focus on the variation of the microstructures, its influence on the feature of fracture, and the establishment of fracture model and mechanism.

Acknowledgements

I would like to take this opportunity to express my gratitude to all of them who helped me during my Ph.D. days in Germany. Without their support, I would not have accomplished this work successfully and enjoyed my life in Dresden.

First and foremost, I would like to express my deep gratitude to Prof. Dr. Jürgen Eckert for providing the invaluable opportunity to do my Ph.D. work in Leibniz Institute for Solid State and Materials Research (IFW Dresden), in association with Faculty of Mechanical Science and Engineering at Technische Universität Dresden (TU Dresden). Even though he moved from Dresden to Leoben during my Ph.D. days, I still can feel his encouraged love as a father from afar.

I equally express my sincere gratitude to my research supervisor Dr. Sergio Scudino who gave me numerous and impressive support during my Ph.D. days. I sincerely thank him for his understanding and concern at a professional and personal level, as well as his patience as a tutor, carefulness as a scientist and promptness as a friend, even in his busiest time. In my future academic career, his exemplary scientific acumen and meticulousness will be cherished and strived for.

The supportive atmosphere inherent to Institute for Complex Materials (ICM) contributed to the final outcome of my studies. I would like to give my thanks to Dr. Thomas Gemming and Dr. Ivan Kaban. With their help, it is possible for me to participate in international conferences and accomplish my Ph.D. work in ICM. I extent my gratitude to the various people in our institute, and without their contributions, some of my Ph.D. work would not have been possible: Dr. U. Kühn and Dr. Simon Pauly for SLM processing, Dr. Annett Gebert and Marion Johne for corrosion test and characterization, Dr. H. Wendrock for SEM and EBSD measurements, Dr. Anja Waske and Alexander Funk for CT measurements, Dr. Volker Hoffmann for surface roughness measurements, Dina Bieberstein and Dr. R. Gregorio Mendes for TEM characterization, Birgit Bartusch for DSC measurement, S. Neumann and J. Scheiter for heat treatment, and Alexander Schultze for wear test. It has been a pleasure working with them. I also equally give my gratitude to Dr. David Geißler, Birgit Opitz, Andrea Voß, S. Donath, Michael Frey, Harald Merker, Steffen Grundkowski, Falk Thunig, Tino Wolf and Nicole Geißer for their technical support and advices.

I also would like to express my sincere thanks to the friends working in our SLM lab: Tobias Gustmann, Dr. Jan Sander, Dr. Holger Schwab, Omar Oday Salman, and Liang Deng. With their

scientific discussion, kindly help and creative collaboration, I could step in the SLM field easily and accomplish my Ph.D. work so well.

I also express my great thanks to my country, who gives me the opportunity to study in Germany and the financial support of Chinese Scholarship Council (CSC).

I am indebted to all the former and current friends of the solidification processes and complex structures department in ICM, especially, Dr. Mihai Stoica, Dr. Mariana Calin, Dr. Konrad Kosiba, Dr. Hyoyun Jung, Dr. Hooyar Attar, Dr. Junhee Han, Dr. Olga Shuleshova, Jaskarn Shergill, Dr. Daniel Sopu, Dr. Baran Sarac, Pramote Thirathipviwat, Rub Nawaz Shahid, Ju Wang, Yanfei Sui, Bo Gao, Prof. Dr. Shenghai Wang, Dr. Ahmed Omar, Dr. Jinbo Pang, Mo Li, and Wenjing Ren. The sincere thanks should be given to our secretory, Brit Präßler-Wüstling and Janett Schuster, for all their administrative help and advice.

During my Ph.D. work, I have a various collaboration from different countries and get many fruitful suggestion from my friends. Thank for the helpful discussion of Assoc. Prof. Dr. Prashanth Konda Gokuldoss from Norwegian University of Science and Technology, Norge, about the preparation of SLM samples, the guiding discussion of Prof. Dr. Thomas Niendorf and Florian Brenne from University of Kassel, Germany, about the preparation and analysis of the EBSD samples, the comprehensive TEM analysis of Dr. Christoph Gammer at Erich Schmid Institute, Austria, and also the nanoindentation analysis of Dr. Tapabarata Maity at Erich Schmid Institute, Austria. Additionally, thank for some kindly friends from other universities, Assoc. Prof. Laichang Zhang from Edith Cowan University, Australia; Dr. Pan Ma from Shanghai University of Engineering Science, China; Dr. Yandong Jia from Shanghai University, China, and Tiwen Lu from South China University of Technology, China.

Thanks to my office colleagues Dr. Parthiban, Hans Weber, Dr. Lixia Xi and Dr. Supriya Bera for great memories, creative collaborations. I wish to express my sincere thanks to all my former and current flat mates: Ye Liu, Dr. Haichao Li, Dr. Tao Zhang and Dr. Long Zhang, for the pleasant atmosphere at home. Also thanks to my Chinese friends in Dresden: Dr. Yangxi Fu, Dr. Bin Cai, Baobao Chang, Lanfa Liu, Min Ji, Mo Li, Dr. Tianyi Li, Jinpeng Zhu, Dr. Kangfa Deng, Bo Yin, Jiawen Zhang, Dr. Xiaolei Sun, Dr. Hua Pang, Dr. Xueyi Lu, Dr. Luke Yan, Dr. Lulu Zhang, Tianbing He, Qiongqiong Lu, Zichao Li, Peng Xue, and Ling Ding.

Finally, I would like to give my special thanks to my mother, father, aunts, uncles, brothers- and sisters-in-law for their constant support and encouragement. Special thanks to my beloved, Zemei, for her love and support. This thesis is dedicated to my uncle, Prof. Dr. Mingde Duan, who has been my constant source of guidance and motivation.

Vielen Dank!☺ ☺ ☺

Pei Wang
30.04.2018

References

[1] J.J. Beaman, J.W. Barlow, D.L. Bourell, R.H. Crawford, H.L. Marcus, K.P. McAlea, Solid freeform fabrication: a new direction in manufacturing, Kluwer Academic Publishers, Norwell, MA 2061 (1997) 25-49.

[2] J.-P. Kruth, M.C. Leu, T. Nakagawa, Progress in Additive Manufacturing and Rapid Prototyping, CIRP Annals - Manufacturing Technology 47 (1998) 525-540.

[3] S. Singh, S. Ramakrishna, R. Singh, Material issues in additive manufacturing: A review, J. Manuf. Process. 25 (2017) 185-200.

[4] D.I. Wimpenny, P.M. Pandey, L.J. Kumar, Advances in 3D Printing & Additive Manufacturing Technologies, first ed., Springer Singapore2017.

[5] M.K. Thompson, G. Moroni, T. Vaneker, G. Fadel, R.I. Campbell, I. Gibson, A. Bernard, J. Schulz, P. Graf, B. Ahuja, F. Martina, Design for Additive Manufacturing: Trends, opportunities, considerations, and constraints, CIRP Annals - Manufacturing Technology 65 (2016) 737-760.

[6] A. Emelogu, M. Marufuzzaman, S.M. Thompson, N. Shamsaei, L. Bian, Additive manufacturing of biomedical implants: A feasibility assessment via supply-chain cost analysis, Addit. Manuf. 11 (2016) 97-113.

[7] L. Hitzler, M. Merkel, W. Hall, A. Öchsner, A Review of Metal Fabricated with Laser- and Powder-Bed Based Additive Manufacturing Techniques: Process, Nomenclature, Materials, Achievable Properties, and its Utilization in the Medical Sector, Adv. Eng. Mater (2018) 1700658.

[8] S. Mellor, L. Hao, D. Zhang, Additive manufacturing: A framework for implementation, Int. J. Prod. Econ. 149 (2014) 194-201.

[9] G. Marchelli, D. Bourell, R. Prabhakar, D. Storti, M. Ganter, The guide to glass 3D printing: developments, methods, diagnostics and results, Rapid Prototyping J. 17 (2011) 187-194.

[10] D. Herzog, V. Seyda, E. Wycisk, C. Emmelmann, Additive manufacturing of metals, Acta Mater. 117 (2016) 371-392.

[11] X.P. Li, M.P. Roberts, S. O'Keeffe, T.B. Sercombe, Selective laser melting of Zr-based bulk metallic glasses: Processing, microstructure and mechanical properties, Mater. Des. 112 (2016) 217-226.

[12] H. Wu, W. Liu, R. He, Z. Wu, Q. Jiang, X. Song, Y. Chen, L. Cheng, S. Wu, Fabrication of dense zirconia-toughened alumina ceramics through a stereolithography-based additive manufacturing, Ceram. Int. 43 (2017) 968-972.

[13] F.P.W. Melchels, M.A.N. Domingos, T.J. Klein, J. Malda, P.J. Bartolo, D.W. Hutmacher, Additive manufacturing of tissues and organs, Prog. Polym. Sci. 37 (2012) 1079-1104.

[14] V.K. Vashishtha, R. Makade, N. Mehla, Advancement of rapid prototyping in aerospace industry-a review, Int. J. Eng. Sci. Tech. 3 (2011) 2486-2493.

[15] A. Marro, T. Bandukwala, W. Mak, Three-Dimensional Printing and Medical Imaging: A Review of the Methods and Applications, Curr. Probl. Diagn. Radiol. 45 (2016) 2-9.

[16] E.K. Sackmann, L. Majlof, A. Hahn-Windgassen, B. Eaton, T. Bandzava, J. Daulton, A. Vandenbroucke, M. Mock, R.G. Stearns, S. Hinkson, S.S. Datwani, Technologies That Enable Accurate and Precise Nano- to Milliliter-Scale Liquid Dispensing of Aqueous Reagents Using Acoustic Droplet Ejection, J. Lab. Autom. 21 (2016) 166-77.

[17] L.E. Murr, S.M. Gaytan, D.A. Ramirez, E. Martinez, J. Hernandez, K.N. Amato, P.W. Shindo, F.R. Medina, R.B. Wicker, Metal Fabrication by Additive Manufacturing Using Laser and Electron Beam Melting Technologies, J. Mater. Sci. Technol. 28 (2012) 1-14.

[18] http://www.objexlab.com/educatie/regulier-onderwijs-minor-aanbod-2/.

[19] Z. Liu, M. Zhang, B. Bhandari, Y. Wang, 3D printing: Printing precision and application in food sector, Trends Food Sci. Technol. 69 (2017) 83-94.

[20] F. Rengier, A. Mehndiratta, H. von Tengg-Kobligk, C.M. Zechmann, R. Unterhinninghofen, H.U. Kauczor, F.L. Giesel, 3D printing based on imaging data: review of medical applications, Int. J. Comput. Assist. Radiol. Surg. 5 (2010) 335-41.

[21] T. Rayna, L. Striukova, From rapid prototyping to home fabrication: How 3D printing is changing business model innovation, Technol. Forecast Soc. 102 (2016) 214-224.

[22] 1] Liu R, Wang Z, Sparks T, Liou F, Newkirk J. 13-Aerospace applications of laser additive manufacturing. In: M. Brandt (Ed.). Laser Additive Manufacturing Elsevier Ltd, New York, USA: 2017. pp. 351-371.

[23] C.Y. Yap, C.K. Chua, Z.L. Dong, Z.H. Liu, D.Q. Zhang, L.E. Loh, S.L. Sing, Review of selective laser melting: Materials and applications, Appl. Phys. Rev. 2 (2015) 04110.

[24] K. Brans, 3D Printing, a Maturing Technology, IFAC Proceedings Volumes 46 (2013) 468-472.

[25] https://www.pinterest.com/pin/344595808965405860/).

[26] C. Atwood, M. Griffith, M. Schlienger, L. Harwell, M. Ensz, D. Keicher, M. Schlienger, J. Romero, J. Smugeresky, Laser engineered net shaping (LENS): a tool for direct fabrication of metal parts, Proceedings of ICALEO, 1998, pp. 16-19.

[27] J. Laeng, J.G. Stewart, F.W. Liou, Laser metal forming processes for rapid prototyping - A review, Int. J. Prod. Res. 38 (2010) 3973-3996.

[28] F. Weng, C. Chen, H. Yu, Research status of laser cladding on titanium and its alloys: A review, Mater. Des. 58 (2014) 412-425.

[29] M.R. Boddu, R.G. Landers, F.W. Liou, Control of laser cladding for rapid prototyping-A review, Proceedings of the Solid Freeform Fabrication Symposium, 2001, pp. 6-8.

[30] http://www.haydencorp.com/content.php?p=laser_metal_deposition).

[31] H.P. Qu, P. Li, S.Q. Zhang, A. Li, H.M. Wang, Microstructure and mechanical property of laser melting deposition (LMD) Ti/TiAl structural gradient material, Mater. Des. 31 (2010) 574-582.

[32] T. Gualtieri, A. Bandyopadhyay, Niobium carbide compostie coatings on SS304 using laser engineered net shaping (LENS™), Mater. Lett. 189 (2017) 89-92.

[33] A. Singh, A. Ramakrishnan, G.P. Dinda, Direct Laser Metal Deposition of Eutectic Al-Si Alloy for Automotive Applications, (2017) 71-80.

[34] A. Singh, A. Ramakrishnan, D. Baker, A. Biswas, G.P. Dinda, Laser metal deposition of nickel coated Al 7050 alloy, J. Alloys Compd. 719 (2017) 151-158.

[35] D.D. Gu, W. Meiners, K. Wissenbach, R. Poprawe, Laser additive manufacturing of metallic components: materials, processes and mechanisms, Int. Mater. Rev. 57 (2012) 133-164.

[36] X. Zhou, K. Li, D. Zhang, X. Liu, J. Ma, W. Liu, Z. Shen, Textures formed in a CoCrMo alloy by selective laser melting, J. Alloys Compd. 631 (2015) 153-164.

[37] E.O. Olakanmi, R.F. Cochrane, K.W. Dalgarno, Densification mechanism and microstructural evolution in selective laser sintering of Al-12Si powders, J. Mater. Process. Tech. 211 (2011) 113-121.

[38] D. Buchbinder, H. Schleifenbaum, S. Heidrich, W. Meiners, J. Bültmann, High Power Selective Laser Melting (HP SLM) of Aluminum Parts, Phys. Procedia 12 (2011) 271-278.

[39] E.O. Olakanmi, R.F. Cochrane, K.W. Dalgarno, A review on selective laser sintering/melting (SLS/SLM) of aluminium alloy powders: Processing, microstructure, and properties, Prog. Mater. Sci. 74 (2015) 401-477.

[40] B. Vandenbroucke, J.-P. Kruth, Selective laser melting of biocompatible metals for rapid manufacturing of medical parts, Rapid Prototyping J. 13 (2007) 196-203.

[41] K.V. Wong, A. Hernandez, A Review of Additive Manufacturing, in: N. Anifantis., F. Findik (Ed.), ISRN Mechanical Engineering2012, pp. 1-10.

[42] A. Mohammadhosseini, S.H. Masood, D. Fraser, M. Jahedi, Dynamic compressive behaviour of Ti-6Al-4V alloy processed by electron beam melting under high strain rate loading, Advances in Manufacturing 3 (2015) 232-243.

[43] H.K. Rafi, N.V. Karthik, H. Gong, T.L. Starr, B.E. Stucker, Microstructures and Mechanical Properties of Ti6Al4V Parts Fabricated by Selective Laser Melting and Electron Beam Melting, J. Mater. Eng. Perform. 22 (2013) 3872-3883.

[44] C.J. Smith, F. Derguti, E. Hernandez Nava, M. Thomas, S. Tammas-Williams, S. Gulizia, D. Fraser, I. Todd, Dimensional accuracy of Electron Beam Melting (EBM) additive manufacture with regard to weight optimized truss structures, J. Mater. Process. Tech. 229 (2016) 128-138.

[45] D.D. Gu, F. Chang, D.D. Dai, Selective laser melting additive manufacturing of novel aluminum based composites with multiple reinforcing phases, ASME. J. Manuf. Sci. Eng. 137 (2014) 021010.

[46] P. Wang, C. Gammer, F. Brenne, K.G. Prashanth, R.G. Mendes, M.H. Rümmeli, T. Gemming, J. Eckert, S. Scudino, Microstructure and mechanical properties of a heat-treatable Al-3.5Cu-1.5Mg-1Si alloy produced by selective laser melting, Mater. Sci. Eng., A 711 (2018) 562-570.

[47] K.G. Prashanth, S. Scudino, T. Maity, J. Das, J. Eckert, Is the energy density a reliable parameter for materials synthesis by selective laser melting?, Mater. Res. Lett. 5 (2017) 1-5.

[48] R. Chou, J. Milligan, M. Paliwal, M. Brochu, Additive Manufacturing of Al-12Si Alloy Via Pulsed Selective Laser Melting, JOM 67 (2015) 590-596.

[49] U.S. Bertoli, A.J. Wolfer, M.J. Matthews, J.P.R. Delplanque, J.M. Schoenung, On the limitations of Volumetric Energy Density as a design parameter for Selective Laser Melting, Mater. Des. 113 (2017) 331-340.

[50] T. Gustmann, A. Neves, U. Kühn, P. Gargarella, C.S. Kiminami, C. Bolfarini, J. Eckert, S. Pauly, Influence of processing parameters on the fabrication of a Cu-Al-Ni-Mn shape-memory alloy by selective laser melting, Addit. Manuf. 11 (2016) 23-31.

[51] W. Li, J. Liu, Y. Zhou, S. Li, S. Wen, Q. Wei, C. Yan, Y. Shi, Effect of laser scanning speed on a Ti-45Al-2Cr-5Nb alloy processed by selective laser melting: Microstructure, phase and mechanical properties, J. Alloys Compd. 688 (2016) 626-636.

[52] J.J. Wu, L.Z. Wang, X.G An, Numerical analysis of residual stress evolution of AlSi10Mg manufactured by selective laser melting, Optik. 137 (2017) 65-78.

[53] C. Zhao, K. Fezzaa, R.W. Cunningham, H. Wen, F. De Carlo, L. Chen, A.D. Rollett, T. Sun, Real-time monitoring of laser powder bed fusion process using high-speed X-ray imaging and diffraction, Sci. Rep. 7 (2017).

[54] D. Wang, C. Yu, J. Ma, W. Liu, Z. Shen, Densification and crack suppression in selective laser melting of pure molybdenum, Mater. Des. 129 (2017) 44-52.

[55] X. Shi, S. Ma, C. Liu, Q. Wu, Parameter optimization for Ti-47Al-2Cr-2Nb in selective laser melting based on geometric characteristics of single scan tracks, Opt. Laser Technol. 90 (2017) 71-79.

[56] H. Attar, M. Bönisch, M. Calin, L.C. Zhang, S. Scudino, J. Eckert, Selective laser melting of in situ titanium-titanium boride composites: Processing, microstructure and mechanical properties, Acta Mater. 76 (2014) 13-22.

[57] K.G. Prashanth, S. Scudino, J. Eckert, Defining the tensile properties of Al-12Si parts produced by selective laser melting, Acta Mater. 126 (2017) 25-35.

[58] B. Cheng, S. Shrestha, K. Chou, Stress and deformation evaluations of scanning strategy effect in selective laser melting, Addit. Manuf. 12 (2016) 240-251.

[59] L. Thijs, K. Kempen, J.-P. Kruth, J. Van Humbeeck, Fine-structured aluminium products with controllable texture by selective laser melting of pre-alloyed AlSi10Mg powder, Acta Mater. 61 (2013) 1809-1819.

[60] W. Li, J. Liu, S. Wen, Q. Wei, C. Yan, Y. Shi, Crystal orientation, crystallographic texture and phase evolution in the Ti-45Al-2Cr-5Nb alloy processed by selective laser melting, Mater. Charact. 113 (2016) 125-133.

[61] J.R. Ho, C.P. Grigoropoulos, J.A.C. Humphrey, Gas dynamics and radiation heat transfer in the vapor plume produced by pulsed laser irradiation of aluminum, J. Appl. Phys. 79 (1996) 7205-7215.

[62] Y.L. Li, D.D. Gu, Parametric analysis of thermal behavior during selective laser melting additive manufacturing of aluminum alloy powder, Mater. Des. 63 (2014) 856-867.

[63] D. Dai, D. Gu, Influence of thermodynamics within molten pool on migration and distribution state of reinforcement during selective laser melting of AlN/AlSi10Mg composites, Int. J. Mach. Tool. 100 (2016) 14-24.

[64] S. Pauly, L. Löber, R. Petters, M. Stoica, S. Scudino, U. Kühn, J. Eckert, Processing metallic glasses by selective laser melting, Mater. Today 16 (2013) 37-41.

[65] D.H. Dai, D.D. Gu, R. Poprawe, M.J. Xia, Influence of additive multilayer feature on thermodynamics, stress and microstructure development during laser 3D printing of aluminum-based material, Sci. Bull. 62 (2017) 779-787.

[66] L.E. Loh, C.K. Chua, W.Y. Yeong, J. Song, M. Mapar, S.L. Sing, Z.H. Liu, D.Q. Zhang, Numerical investigation and an effective modelling on the selective laser melting (SLM) process with aluminium alloy 6061, Int. J. Heat and Mass Transfer 80 (2015) 288-300.

[67] W. Kurz, D.J. Fisher, Fundamentals of solidification, third ed., Trans Tech Publications, Switzerland, 1989.

[68] S. Kou, Welding metallurgy, second ed., John Wiley & Sons, Inc2003.

[69] W.A. Tiller, K.A. Jackson, J.W. Rutter, B. Chalmers, The redistribution of solute atoms during the solidification of metals, Acta Metall. 1 (1953) 428-437.

[70] J.W. Rutter, B. Chalmers, A prismatic substructure formed during solidification of metals, Can. J. Phys. 31 (1953) 15-39.

[71] W.W. Mullins, R.F. Sekerka, Morphological Stability of a Particle Growing by Diffusion or Heat Flow, J. Appl. Phys. 34 (1963) 323-329.

[72] W.W. Mullins, R.F. Sekerka, Stability of a Planar Interface During Solidification of a Dilute Binary Alloy, J. Appl. Phys. 35 (1964) 444-451.

[73] S.R. Coriell, R.F. Sekerka, Oscillatory morphological instabilities due to non-equilibrium segregation, J. Cryst. Growth 61 (1983) 499-508.

[74] K.A. Jackson, J.D. Hunt, Transparent compounds that freeze like metals, Acta Metall. 13 (1965) 1212-1215.

[75] L.R. Morris, W.C. Winegard, The development of cells during the solidification of a dilute Pb-Sb alloy, J. Cryst. Growth 5 (1969) 361-375.

[76] Y.J. Xie, M.C. Wang, Microstructural morphology of electrospark deposition layer of a high gamma prime superalloy, Surf. Coat. Technol. 201 (2006) 691-698.

[77] J.D. Hunt, Steady state columnar and equiaxed growth of dendrites and eutectic, Mater. Sci. and Eng. 65 (1984) 75-83.

[78] W.J. Boettinger, D. Shechtman, R.J. Schaefer, F.S. Biancaniello, The Effect of Rapid Solidification Velocity on the Microstructure of Ag-Cu Alloys, Metall. Trans. A 15 (1984) 55-66.

[79] M. Gremaud, M. Carrard, W. Kurz, The microstructure of rapidly solidified Al-Fe alloys subjected to laser surface treatment, Acta Metall. 38 (1990) 2587-2599.

[80] M. Carrard, M. Gremaud, M. Zimmermann, W. Kurz, About the banded structure in rapidly solidified dendritic and eutectic alloys, Acta Metall. 40 (1992) 983-996.

[81] J.T. McKeown, A.K. Kulovits, C. Liu, K. Zweiacker, B.W. Reed, T. LaGrange, J.M.K. Wiezorek, G.H. Campbell, In situ transmission electron microscopy of crystal growth-mode transitions during rapid solidification of a hypoeutectic Al-Cu alloy, Acta Mater. 65 (2014) 56-68.

[82] X.P. Li, X.J. Wang, M. Saunders, A. Suvorova, L.C. Zhang, Y.J. Liu, M.H. Fang, Z.H. Huang, T.B. Sercombe, A selective laser melting and solution heat treatment refined Al-12Si alloy with a controllable ultrafine eutectic microstructure and 25 % tensile ductility, Acta Mater. 95 (2015) 74-82.

[83] R. Dayal, T. Gambaryan-Roisman, Heat transfer in granular medium for application to selective laser melting: A numerical study, Int. J. Therm. Sci. 113 (2017) 38-50.

[84] L. Thijs, F. Verhaeghe, T. Craeghs, J.V. Humbeeck, J.-P. Kruth, A study of the microstructural evolution during selective laser melting of Ti-6Al-4V, Acta Mater. 58 (2010) 3303-3312.

[85] Y.J. Liu, Z. Liu, Y. Jiang, G.W. Wang, Y. Yang, L.C. Zhang, Gradient in microstructure and mechanical property of selective laser melted AlSi10Mg, J. Alloys Compd. 735 (2018) 1414-1421.

[86] Q. Lei, B.P. Ramakrishnan, S. Wang, Y. Wang, J. Mazumder, A. Misra, Structural refinement and nanomechanical response of laser remelted Al-Al_2Cu lamellar eutectic, Mater. Sci. Eng., A 706 (2017) 115-125.

[87] M. Zimmermann, M. Carrard, W. Kurz, Rapid solidification of Al-Cu eutectic alloy by laser remelting, Acta Metall. 37 (1989) 3305-3313.

[88] H. Rao, S. Giet, K. Yang, X. Wu, C.H.J. Davies, The Influence of Processing Parameters on Aluminium Alloy A357 Manufactured by Selective Laser Melting, Mater. Des. 109 (2016) 334-346.

[89] S.N. Cao, D.D. Gu, Q.M. Shi, Relation of microstructure, microhardness and underlying thermodynamics in molten pools of laser melting deposition processed TiC/Inconel 625 composites, J. Alloys Compd. 692 (2017) 758-769.

[90] Y. Liu, J. Zhang, Z. Pang, Numerical and experimental investigation into the subsequent thermal cycling during selective laser melting of multi-layer 316L stainless steel, Opt Laser Technol 98 (2018) 23-32.

[91] W. Li, S. Li, J. Liu, A. Zhang, Y. Zhou, Q.S. Wei, C.Z. Yan, Y.S. Shi, Effect of heat treatment on AlSi10Mg alloy fabricated by selective laser melting: Microstructure evolution, mechanical properties and fracture mechanism, Mater. Sci. Eng., A 663 (2016) 116-125.

[92] S. Pauly, C. Schricker, S. Scudino, L. Deng, U. Kühn, Processing a glass-forming Zr-based alloy by selective laser melting, Mater. Des. 135 (2017) 133-141.

[93] L. Deng, S. Wang, P. Wang, U. Kühn, S. Pauly, Selective laser melting of a Ti-based bulk metallic glass, Mater. Lett. 212 (2018) 346-349.

[94] A.B. Anwar, Q.-C. Pham, Selective laser melting of AlSi10Mg: Effects of scan direction, part placement and inert gas flow velocity on tensile strength, J. Mater. Process. Tech. 240 (2017) 388-396.

[95] G. Ziółkowski, E. Chlebus, P. Szymczyk, J. Kurzac, Application of X-ray CT method for discontinuity and porosity detection in 316L stainless steel parts produced with SLM technology, Archives of Civil and Mechanical Engineering 14 (2014) 608-614.

[96] P. Wang, H.C. Li, K.G. Prashanth, J. Eckert, S. Scudino, Selective laser melting of Al-Zn-Mg-Cu: Heat treatment, microstructure and mechanical properties, J. Alloys Compd. (2016).

[97] G. Yablokova, M. Speirs, J. Van Humbeeck, J.-P. Kruth, J. Schrooten, R. Cloots, F. Boschini, G. Lumay, J. Luyten, Rheological behavior of β-Ti and NiTi powders produced by atomization for SLM production of open porous orthopedic implants, Powder Technol. 283 (2015) 199-209.

[98] T. Marcu, M. Todea, I. Gligor, P. Berce, C. Popa, Effect of surface conditioning on the flowability of Ti6Al7Nb powder for selective laser melting applications, Appl. Surf. Sci. 258 (2012) 3276-3282.

[99] R.E. Russo, Laser ablation, Appl. Spectrosc. 49 (1995) 14A-28A.

[100] W. Reschetnik, J.-P. Brüggemann, M.E. Aydinöz, O. Grydin, K.-P. Hoyer, G. Kullmer, H.A. Richard, Fatigue crack growth behavior and mechanical properties of additively processed EN AW-7075 aluminium alloy, Procedia Struct. Integr. 2 (2016) 3040-3048.

[101] H. Zhang, H.H. Zhu, X.J. Nie, J. Yin, Z.H. Hu, X.Y. Zeng, Effect of Zirconium addition on crack, microstructure and mechanical behavior of selective laser melted Al-Cu-Mg alloy, Scr. Mater. 134 (2017) 6-10.

[102] T. Kimura, T. Nakamoto, M. Mizuno, H. Araki, Effect of silicon content on densification, mechanical and thermal properties of Al-xSi binary alloys fabricated using selective laser melting, Mater. Sci. Eng., A 682 (2017) 593-602.

[103] R. Li, Y. Shi, Z. Wang, L. Wang, J. Liu, W. Jiang, Densification behavior of gas and water atomized 316L stainless steel powder during selective laser melting, Appl. Surf. Sci. 256 (2010) 4350-4356.

[104] L.X. Liu, I. Marziano, A.C. Bentham, J.D. Litster, E.T. White, T. Howes, Effect of particle properties on the flowability of ibuprofen powders, Int. J. Pharm. 362 (2008) 109-17.

[105] E.O. Olakanmi, Selective laser sintering/melting (SLS/SLM) of pure Al, Al-Mg, and Al-Si powders: Effect of processing conditions and powder properties, J Mater Process Tech 213 (2013) 1387-1405.

[106] W.J. Boettinger, L. Bendersky, J.G. Early, An analysis of the microstructure of rapidly solidified Al-8 wt pct Fe powder, Metall. Trans. A 17 (1986) 781-790.

[107] E. Yasa, J.-P. Kruth, Application of laser re-melting on selective laser melting parts, Adv. Prod. Eng. Manag. 6 (2011) 259-270.

[108] P. Mercelis, J.-P. Kruth, Residual stresses in selective laser sintering and selective laser melting, Rapid Prototyping J. 12 (2006) 254-265.

[109] T. Simson, A. Emmel, A. Dwars, J. Böhm, Residual stress measurements on AISI 316L samples manufactured by selective laser melting, Addit. Manuf. 17 (2017) 183-189.

[110] S. Afazov, W.A.D. Denmark, B. Lazaro Toralles, A. Holloway, A. Yaghi, Distortion prediction and compensation in selective laser melting, Addit. Manuf. 17 (2017) 15-22.

[111] T. Vilaro, C. Colin, J.D. Bartout, As-Fabricated and Heat-Treated Microstructures of the Ti-6Al-4V Alloy Processed by Selective Laser Melting, Metall. Mater. Trans. A 42 (2011) 3190-3199.

[112] N. Kaufmann, M. Imran, T.M. Wischeropp, C. Emmelmann, S. Siddique, F. Walther, Influence of Process Parameters on the Quality of Aluminium Alloy EN AW 7075 Using Selective Laser Melting (SLM), Phys. Procedia 83 (2016) 918-926.

[113] W. Xu, M. Brandt, S. Sun, J. Elambasseril, Q. Liu, K. Latham, K. Xia, M. Qian, Additive manufacturing of strong and ductile Ti-6Al-4V by selective laser melting via in situ martensite decomposition, Acta Mater. 85 (2015) 74-84.

[114] B. Vrancken, L. Thijs, J.-P. Kruth, J.V. Humbeeck, Heat treatment of Ti6Al4V produced by Selective Laser Melting: Microstructure and mechanical properties, J. Alloys Compd. 541 (2012) 177-185.

[115] C.Y. Yap, C.K. Chua, Z.L. Dong, Z.H. Liu, D.Q. Zhang, L.E. Loh, S.L. Sing, Review of selective laser melting: Materials and applications, Appl Phys Rev 2 (2015) 041101.

[116] J. Suryawanshi, K.G. Prashanth, S. Scudino, J. Eckert, O. Prakash, U. Ramamurty, Simultaneous enhancements of strength and toughness in an Al-12Si alloy synthesized using selective laser melting, Acta Mater. 115 (2016) 285-294.

[117] N.T. Aboulkhair, I. Maskery, C. Tuck, I. Ashcroft, N.M. Everitt, Improving the fatigue behaviour of a selectively laser melted aluminium alloy: Influence of heat treatment and surface quality, Mater. Des. 104 (2016) 174-182.

[118] M. Tang, P. Chris Pistorius, Oxides, porosity and fatigue performance of AlSi10Mg parts produced by selective laser melting, Int. J. Fatigue 94 (2017) 192-201.

[119] N. Kang, P. Coddet, C. Chen, Y. Wang, H. Liao, C. Coddet, Microstructure and wear behavior of in-situ hypereutectic Al-high Si alloys produced by selective laser melting, Mater. Des. 99 (2016) 120-126.

[120] Y.D. Jia, P. Ma, K.G. Prashanth, G. Wang, J. Yi, S. Scudino, F.Y. Cao, J.F. Sun, J. Eckert, Microstructure and thermal expansion behavior of Al-50Si synthesized by selective laser melting, J. Alloys Compd. 699 (2017) 548-553.

[121] P. Ma, K. Prashanth, S. Scudino, Y. Jia, H. Wang, C. Zou, Z. Wei, J. Eckert, Influence of Annealing on Mechanical Properties of Al-20Si Processed by Selective Laser Melting, Metals 4 (2014) 28-36.

[122] K.V. Yang, P. Rometsch, T. Jarvis, J. Rao, S. Cao, C. Davies, X. Wu, Porosity formation mechanisms and fatigue response in Al-Si-Mg alloys made by selective laser melting, Mater. Sci. Eng., A 712 (2018) 166-174.

[123] M. Ostermeier, H. Hoffmann, E. Werner, The Effects of Hot Isostatic Pressing on Aluminium Castings, Key Eng. Mater. 345-346 (2007) 1545-1548.

[124] M.L. Montero Sistiaga, R. Mertens, B. Vrancken, X. Wang, B. Van Hooreweder, J.-P. Kruth, J. Van Humbeeck, Changing the alloy composition of Al7075 for better processability by selective laser melting, J. Mater. Process. Tech. 238 (2016) 437-445.

[125] T. Qi, H. Zhu, H. Zhang, J. Yin, L. Ke, X. Zeng, Selective laser melting of Al7050 powder: Melting mode transition and comparison of the characteristics between the keyhole and conduction mode, Mater. Des. 135 (2017) 257-266.

[126] D. Banerjee, J.C. Williams, Perspectives on Titanium Science and Technology, Acta Mater. 61 (2013) 844-879.

[127] S.E. Haghighi, H.B. Lu, G.Y. Jian, G.H. Cao, D. Habibi, L.C. Zhang, Effect of α″ martensite on the microstructure and mechanical properties of beta-type Ti–Fe–Ta alloys, Mater. Des. 76 (2015) 47-54.

[128] M. Geetha, A.K. Singh, R. Asokamani, A.K. Gogia, Ti based biomaterials, the ultimate choice for orthopaedic implants – A review, Prog. Mater. Sci. 54 (2009) 397-425.

[129] H. Attar, M. Calin, L.C. Zhang, S. Scudino, J. Eckert, Manufacture by selective laser melting and mechanical behavior of commercially pure titanium, Mater. Sci. Eng., A 593 (2014) 170-177.

[130] S. Zhang, X. Lin, J. Chen, W. Huang, Heat-treated microstructure and mechanical properties of laser solid forming Ti-6Al-4V alloy, Rare Metals 28 (2009) 537-544.

[131] L.C. Zhang, H. Attar, Selective Laser Melting of Titanium Alloys and Titanium Matrix Composites for Biomedical Applications: A Review Adv. Eng. Mater. 18 (2016) 463-475.

[132] M. Wang, X. Lin, W. Huang, Laser additive manufacture of titanium alloys, Mater. Tech. (2015) 1753555715Y.000.

[133] P. Heinl, L. Muller, C. Korner, R.F. Singer, F.A. Muller, Cellular Ti-6Al-4V structures with interconnected macro porosity for bone implants fabricated by selective electron beam melting, Acta Biomater. 4 (2008) 1536-44.

[134] H. Schwab, K. Prashanth, L. Löber, U. Kühn, J. Eckert, Selective Laser Melting of Ti-45Nb Alloy, Metals 5 (2015) 686-694.

[135] H. Schwab, F. Palm, U. Kühn, J. Eckert, Microstructure and mechanical properties of the near-beta titanium alloy Ti-5553 processed by selective laser melting, Mater. Des. 105 (2016) 75-80.

[136] W. Li, J. Liu, Y. Zhou, S. Wen, Q. Wei, C. Yan, Y. Shi, Effect of substrate preheating on the texture, phase and nanohardness of a Ti-45Al-2Cr-5Nb alloy processed by selective laser melting, Scr. Mater. 118 (2016) 13-18.

[137] D. Gu, H. Wang, G. Zhang, Selective Laser Melting Additive Manufacturing of Ti-Based Nanocomposites: The Role of Nanopowder, Metall. Mater. Trans. A 45 (2013) 464-476.

[138] D. Gu, G. Meng, C. Li, W. Meiners, R. Poprawe, Selective laser melting of TiC/Ti bulk nanocomposites: Influence of nanoscale reinforcement, Scr. Mater. 67 (2012) 185-188.

[139] D. Gu, Y.-C. Hagedorn, W. Meiners, G. Meng, R.J.S. Batista, K. Wissenbach, R. Poprawe, Densification behavior, microstructure evolution, and wear performance of selective laser melting processed commercially pure titanium, Acta Mater. 60 (2012) 3849-3860.

[140] K. Prashanth, L. Löber, H.-J. Klauss, U. Kühn, J. Eckert, Characterization of 316L Steel Cellular Dodecahedron Structures Produced by Selective Laser Melting, Technologies 4 (2016) 34.

[141] X. Lin, T.M. Yue, Phase formation and microstructure evolution in laser rapid forming of graded SS316L/Rene88DT alloy, Mater. Sci. Eng., A 402 (2005) 294-306.

[142] Y.M. Wang, T. Voisin, J.T. McKeown, J. Ye, N.P. Calta, Z. Li, Z. Zeng, Y. Zhang, W. Chen, T.T. Roehling, R.T. Ott, M.K. Santala, P.J. Depond, M.J. Matthews, A.V. Hamza, T. Zhu, Additively manufactured hierarchical stainless steels with high strength and ductility, Nat. Mater. 17 (2018) 63-71.

[143] J. Sander, J. Hufenbach, L. Giebeler, M. Bleckmann, J. Eckert, U. Kühn, Microstructure, mechanical behavior, and wear properties of FeCrMoVC steel prepared by selective laser melting and casting, Scr. Mater. 126 (2017) 41-44.

[144] J. Sander, J. Hufenbach, M. Bleckmann, L. Giebeler, H. Wendrock, S. Oswald, T. Gemming, J. Eckert, U. Kühn, Selective laser melting of ultra-high-strength TRIP steel: processing, microstructure, and properties, J. Mater. Sci. 52 (2016) 4944-4956.

[145] B. AlMangour, D. Grzesiak, J.M. Yang, Selective laser melting of TiB2/H13 steel nanocomposites: Influence of hot isostatic pressing post-treatment, J. Mater. Process. Tech. 244 (2017) 344-353.

[146] J. Sander, J. Hufenbach, L. Giebeler, H. Wendrock, U. Kühn, J. Eckert, Microstructure and properties of FeCrMoVC tool steel produced by selective laser melting, Mater. Des. 89 (2016) 335-341.

[147] B. AlMangour, D. Grzesiak, J.-M. Yang, Selective laser melting of TiB2/316L stainless steel composites: The roles of powder preparation and hot isostatic pressing post-treatment, Powder Technol. 309 (2017) 37-48.

[148] B. AlMangour, D. Grzesiak, J.-M. Yang, In-situ formation of novel TiC-particle-reinforced 316L stainless steel bulk-form composites by selective laser melting, J. Alloys Compd. 706 (2017) 409-418.

[149] I.A. Choudhury, M.A. El-Baradie, Machinability of nickel-base super alloys: a general review, J. Mater. Process. Tech. 77 (1998) 278-284.

[150] J. Strößner, M. Terock, U. Glatzel, Mechanical and Microstructural Investigation of Nickel-Based Superalloy IN718 Manufactured by Selective Laser Melting (SLM), Adv. Eng. Mater. 17 (2015) 1099-1105.

[151] Q. Jia, D. Gu, Selective laser melting additive manufacturing of Inconel 718 superalloy parts: Densification, microstructure and properties, J. Alloys Compd. 585 (2014) 713-721.

[152] Q. Jia, D. Gu, Selective laser melting additive manufactured Inconel 718 superalloy parts: High-temperature oxidation property and its mechanisms, Opt Laser Technol 62 (2014) 161-171.

[153] L. Rickenbacher, T. Etter, S. Hövel, K. Wegener, High temperature material properties of IN738LC processed by selective laser melting (SLM) technology, Rapid Prototyping J. 19 (2013) 282-290.

[154] S. Li, Q. Wei, Y. Shi, Z. Zhu, D. Zhang, Microstructure Characteristics of Inconel 625 Superalloy Manufactured by Selective Laser Melting, J. Mater. Sci. Technol. 31 (2015) 946-952.

[155] S. Scudino, C. Unterdörfer, K.G. Prashanth, H. Attar, N. Ellendt, V. Uhlenwinkel, J. Eckert, Additive manufacturing of Cu-10Sn bronze, Mater. Lett. 156 (2015) 202-204.

[156] A. Popovich, V. Sufiiarov, I. Polozov, E. Borisov, D. Masaylo, A. Orlov, Microstructure and mechanical properties of additive manufactured copper alloy, Mater. Lett. 179 (2016) 38-41.

[157] C. Yang, Y.J. Zhao, L.M. Kang, D.D. Li, W.W. Zhang, L.C. Zhang, High-strength silicon brass manufactured by selective laser melting, Mater. Lett. 210 (2018) 169-172.

[158] A.P. Ventura, C.A. Wade, G. Pawlikowski, M. Bayes, M. Watanabe, W.Z. Misiolek, Mechanical Properties and Microstructural Characterization of Cu-4.3 Pct Sn Fabricated by Selective Laser Melting, Metall. Mater. Trans. A 48 (2016) 178-187.

[159] C. Shuai, Y. Yang, P. Wu, X. Lin, Y. Liu, Y. Zhou, P. Feng, X. Liu, S. Peng, Laser rapid solidification improves corrosion behavior of Mg-Zn-Zr alloy, J. Alloys Compd. 691 (2017) 961-969.

[160] H. Liao, P. Fu, L. Peng, J. Li, S. Zhang, G. Hu, W. Ding, Microstructure and mechanical properties of laser melting deposited GW103K Mg-RE alloy, Mater. Sci. Eng., A (2017).

[161] A.G. Demir, L. Monguzzi, B. Previtali, Selective laser melting of pure Zn with high density for biodegradable implant manufacturing, Addit. Manuf. 15 (2017) 20-28.

[162] X. Lin, Y.Q. Cao, Z.T. Wang, J. Cao, L.L. Wang, W.D. Huang, Regular eutectic and anomalous eutectic growth behavior in laser remelting of Ni-30 wt. %Sn alloys, Acta Mater. 126 (2017) 210-220.

[163] M. Speirs, B. Van Hooreweder, J. Van Humbeeck, J.-P. Kruth, Fatigue behaviour of NiTi shape memory alloy scaffolds produced by SLM, a unit cell design comparison, J. Mech. Behav. Biomed. Mater. 70 (2017) 53-59.

[164] P. Gargarella, C.S. Kiminami, E.M. Mazzer, R.D. Cava, L.A. Basilio, C. Bolfarini, W.J. Botta, J. Eckert, T. Gustmann, S. Pauly, Phase Formation, Thermal Stability and Mechanical Properties of a Cu-Al-Ni-Mn Shape Memory Alloy Prepared by Selective Laser Melting, Mater. Res. 18 (2015) 35-38.

[165] X.P. Li, G. Ji, Z. Chen, A. Addad, Y. Wu, H.W. Wang, J. Vleugels, J. Van Humbeeck, J.-P. Kruth, Selective laser melting of nano-TiB_2 decorated AlSi10Mg alloy with high fracture strength and ductility, Acta Mater. 129 (2017) 183-193.

[166] D.D. Gu, H.Q. Wang, D.H. Dai, P.P. Yuan, W. Meiners, R. Poprawe, Rapid fabrication of Al-based bulk-form nanocomposites with novel reinforcement and enhanced performance by selective laser melting, Scr. Mater. 96 (2015) 25-28.

[167] A.G. Demir, B. Previtali, Multi-material selective laser melting of Fe/Al-12Si components, Manuf. Lett. 11 (2017) 8-11.

[168] N. Xiang, X.Z. Xin, J. Chen, B. Wei, Metal-ceramic bond strength of Co-Cr alloy fabricated by selective laser melting, J. Dent. 40 (2012) 453-7.

[169] H.Y. Jung, S.J. Choi, K.G. Prashanth, M. Stoica, S. Scudino, S. Yi, U. Kühn, D.H. Kim, K.B. Kim, J. Eckert, Fabrication of Fe-based bulk metallic glass by selective laser melting: A parameter study, Mater. Des. 86 (2015) 703-708.

[170] Y. Brif, M. Thomas, I. Todd, The use of high-entropy alloys in additive manufacturing, Scr. Mater. 99 (2015) 93-96.

[171] C. Haase, F. Tang, M.B. Wilms, A. Weisheit, B. Hallstedt, Combining thermodynamic modeling and 3D printing of elemental powder blends for high-throughput investigation of high-entropy alloys – Towards rapid alloy screening and design, Mater. Sci. Eng., A 688 (2017) 180-189.

[172] Y. Fu, N. Kang, H. Liao, Y. Gao, C. Coddet, An investigation on selective laser melting of Al-Cu-Fe-Cr quasicrystal: From single layer to multilayers, Intermetallics 86 (2017) 51-58.

[173] G.E. Totten, D.S. MacKenzie, Handbook of Aluminum Vol. 1: Physical Metallurgy and Processes, Marcel Dekker, New York, 2003.

[174] F.H. Froes, C. Suryanarayana, W. Quist, E.J. Lavernia, B.I. Bondarev, N.F. Anoshkin, I.S. Polkin, O.K. Fatkullin, V. Samarov, A.B. Notkin, Advanced Aerospace Metals Requirements and Characteristics - An Overview, Key Eng. Mater. 77-78 (1992) 1-38.

[175] J.R. Davis, Aluminum and aluminum alloys, ASM International, Materials Park, Ohio, 1993.

[176] L.F. Mondolfo, Aluminum alloys: structure and properties, Butterworths, London, 1976.

[177] K. Bartkowiak, S. Ullrich, T. Frick, M. Schmidt, New developments of laser processing Aluminium alloys via additive manufacturing technique, Physics Procedia 12 (2011) 393-401.

[178] J.-P. Kruth, G. Levy, F. Klocke, T.H.C. Childs, Consolidation phenomena in laser and powder-bed based layered manufacturing, CIRP Annals - Manufacturing Technology 56 (2007) 730-759.

[179] M. Wong, S. Tsopanos, C.J. Sutcliffe, I. Owen, Selective laser melting of heat transfer devices, Rapid Prototyping J. 13 (2007) 291-297.

[180] T. DebRoy, H.L. Wei, J.S. Zuback, T. Mukherjee, J.W. Elmer, J.O. Milewski, A.M. Beese, A. Wilson-Heid, A. De, W. Zhang, Additive manufacturing of metallic components-Process, structure and properties, Prog. Mater. Sci. 92 (2018) 112-224.

[181] N.T. Aboulkhair, I. Maskery, C. Tuck, I. Ashcroft, N.M. Everitt, On the formation of AlSi10Mg single tracks and layers in selective laser melting: Microstructure and nano-mechanical properties, J. Mater. Process. Tech. 230 (2016) 88-98.

[182] N. Read, W. Wang, K. Essa, M.M. Attallah, Selective laser melting of AlSi10Mg alloy: Process optimisation and mechanical properties development, Mater. Des. 65 (2015) 417-424.

[183] E. Brandl, U. Heckenberger, V. Holzinger, D. Buchbinder, Additive manufactured AlSi10Mg samples using Selective Laser Melting (SLM): Microstructure, high cycle fatigue, and fracture behavior, Mater. Des. 34 (2012) 159-169.

[184] K.G. Prashanth, S. Scudino, H.J. Klauss, K.B. Surreddi, L. Löber, Z. Wang, A.K. Chaubey, U. Kühn, J. Eckert, Microstructure and mechanical properties of Al-12Si produced by selective laser melting: Effect of heat treatment, Mater. Sci. Eng., A 590 (2014) 153-160.

[185] K.G. Prashanth, B. Debalina, Z. Wang, P.F. Gostin, A. Gebert, M. Calin, U. Kühn, M. Kamaraj, S. Scudino, J. Eckert, Tribological and corrosion properties of Al-12Si produced by selective laser melting, J. Mater. Res. 29 (2014) 2044-2054.

[186] C.K.S. Moy, M. Weiss, J. Xia, G. Sha, S.P. Ringer, G. Ranzi, Influence of heat treatment on the microstructure, texture and formability of 2024 aluminium alloy, Mater. Sci. Eng., A 552 (2012) 48-60.

[187] E.A. Starke, J.T. Staley, Application of modern aluminum alloys to aircraft, Progress in Aerospace Sciences 32 (1996) 131-172.

[188] T. Dursun, C. Soutis, Recent developments in advanced aircraft aluminium alloys, Mater. Des. 56 (2014) 862-871.

[189] H. Zhang, H.H. Zhu, T. Qi, Z.H. Hu, X.Y. Zeng, Selective laser melting of high strength Al-Cu-Mg alloys: processing, microstructure and mechanical properties, Mater. Sci. Eng., A 656 (2016) 47-54.

[190] R. Casati, J.N. Lemke, A.Z. Alarcon, M. Vedani, Aging behavior of high-strength Al alloy 2618 produced by selective laser melting, Metal. and Mater. Trans. A 48 (2016) 575-579.

[191] M. Karg, B. Ahuja, S. Wiesenmayer, S. Kuryntsev, M. Schmidt, Effects of process conditions on the mechanical behavior of aluminium wrought alloy EN AW-2219 (AlCu6Mn) Additively Manufactured by Laser Beam Melting in Powder Bed, Micromachines 8 (2017) 23.

[192] O. Lopez-Botello, U. Martinez-Hernandez, J. Ramírez, C. Pinna, K. Mumtaz, Two-dimensional simulation of grain structure growth within selective laser melted AA-2024, Mater. Des. 113 (2017) 369-376.

[193] H. Zhang, H.H. Zhu, X.J. Nie, T. Qi, Z.H. Hu, X.Y. Zeng, Fabrication and heat treatment of high strength Al-Cu-Mg alloy processed using selective laser melting, Laser 3D Manufacturing III. International Society for Optics and Photonics 9738 (2016) 97380X.

[194] S. Kou, A simple index for predicting the susceptibility to solidification cracking, Weld. J. 94 (2015) 374-388.

[195] A. Arata, F. Matsuda, K. Nakata, I. Sasaki, Solidification crack susceptibility of aluminum alloy weld metals (Report I): characteristics of ductility curves during solidification by means of the trans-varestraint Test, Trans. JWRI 5 (1976) 53-67.

[196] D. Koutnya, D. Palouseka, O. Koukala, T. Zikmunda, L. Pantelejeva, F. Dokoupila, Processing of high strength Al-Cu alloy using 400W selective laser melting-initial study, Lasers in Manufacturing Conference 2015, 2015.

[197] A. Zatočilová, T. Zikmund, J. Kaiser, D. Paloušek, D. Koutný, Measurement of the Porosity of Additive-Manufactured Al-Cu Alloy Using X-Ray Computed Tomography, Solid State Phenom. 258 (2016) 448-451.

[198] D.J. Chakrabarti, D.E. Laughlin, Phase relations and precipitation in Al-Mg-Si alloys with Cu additions, Prog. Mater. Sci. 49 (2004) 389-410.

[199] C. Ravi, First-principles study of crystal structure and stability of Al-Mg-Si-(Cu) precipitates, Acta Mater. 52 (2004) 4213-4227.

[200] F.L. Zeng, Z.L. Wei, J.F. Li, C.X. Li, X. Tan, Z. Zhang, Z.Q. Zheng, Corrosion mechanism associated with Mg_2Si and Si particles in Al-Mg-Si alloys, T. Nonferr. Metal. Soc. 21 (2011) 2559-2567.

[201] Y.H. Zhao, X.Z. Liao, Z. Jin, R.Z. Valiev, Y.T. Zhu, Microstructures and mechanical properties of ultrafine grained 7075 Al alloy processed by ECAP and their evolutions during annealing, Acta Mater. 52 (2004) 4589-4599.

[202] J.H. Martin, B.D. Yahata, J.M. Hundley, J.A. Mayer, T.A. Schaedler, T.M. Pollock, 3D printing of high-strength aluminium alloys, Nature 549 (2017) 365-369.

[203] A.A. Iqbal, D.M. Nuruzzaman, Effect of the Reinforcement on the Mechanical Properties of Aluminium Matrix Composite: A Review, Int. J. Appl. Eng. Res. 11 (2016) 10408-10413.

[204] J.M. Torralba, C.E. Da Costa, F. Velasco, P/M aluminum matrix composites: an overview, J. Mater. Process. Tech. 133 (2003) 203-206.

[205] C. Yang, Y.Y. Zong, Z.Z. Zheng, D.B. Shan, Experimental and theoretical investigation on the compressive behavior of aluminum borate whisker reinforced 2024Al composites, Mater. Charact. 96 (2014) 84-92.

[206] X.Z. Kai, K.L. Tian, C.M. Wang, L. Jiao, G. Chen, Y.T. Zhao, Effects of ultrasonic vibration on the microstructure and tensile properties of the nano ZrB2/2024Al composites synthesized by direct melt reaction, J. Alloys Compd. 668 (2016) 121-127.

[207] K.G. Prashanth, S. Scudino, A.K. Chaubey, L. Löber, P. Wang, H. Attar, F.P. Schimansky, F. Pyczak, J. Eckert, Processing of Al-12Si-TNM composites by selective laser melting and evaluation of compressive and wear properties, J. Mater. Res. 31 (2015) 55-65.

[208] D.D. Gu, W. Meiners, Microstructure characteristics and formation mechanisms of in situ WC cemented carbide based hardmetals prepared by Selective Laser Melting, Mater. Sci. Eng., A 527 (2010) 7585-7592.

[209] X. Zhao, B. Song, W. Fan, Y. Zhang, Y. Shi, Selective laser melting of carbon/AlSi10Mg composites: Microstructure, mechanical and electronical properties, J. Alloys Compd. 665 (2016) 271-281.

[210] P. Wang, H.C. Li, K.G. Prashanth, J. Eckert, S. Scudino, Selective laser melting of Al-Zn-Mg-Cu: Heat treatment, microstructure and mechanical properties, J. Alloys Compd. 707 (2017) 287-290.

[211] L. Xi, I. Kaban, R. Nowak, B. Korpała, G. Bruzda, N. Sobczak, N. Mattern, J. Eckert, High-temperature wetting and interfacial interaction between liquid Al and TiB_2 ceramic, J. Mater. Sci. 50 (2015) 2682-2690.

[212] J.A. Marcantonio, L.F. Mondolfo, Grain refinement in aluminum alloyed with titanium and boron, Metall. Trans. 2 (1971) 465-471.

[213] P. Schumacher, A.L. Greer, J. Worth, P.V. Evans, M.A. Kearns, P. Fisher, A.H. Green, New studies of nucleation mechanisms in aluminium alloys: implications for grain refinement practice, Mater. Sci. Technol. 14 (2013) 394-404.

[214] T.S. Parel, S.C. Wang, M.J. Starink, Hardening of an Al-Cu-Mg alloy containing Types I and II S phase precipitates, Mater. Des. 31 (2010) S2-S5.

[215] S. Tailor, R.M. Mohanty, V.K. Sharma, P.R. Soni, A.V. Doub, Nanostructured 2024Al-SiCpcomposite coatings, Surf. Eng. 32 (2014) 526-534.

[216] P.L. Threadgill, A.J. Leonard, H.R. Shercliff, P.J. Withers, Friction stir welding of aluminium alloys, Int. Mater. Rev. 54 (2013) 49-93.

[217] S.T. Amancio-Filho, S. Sheikhi, J.F. dos Santos, C. Bolfarini, Preliminary study on the microstructure and mechanical properties of dissimilar friction stir welds in aircraft aluminium alloys 2024-T351 and 6056-T4, J. Mater. Process. Tech. 206 (2008) 132-142.

[218] M. Aonuma, K. Nakata, Dissimilar Metal Joining of 2024 and 7075 Aluminium Alloys to Titanium Alloys by Friction Stir Welding, Mater. Trans. 52 (2011) 948-952.

[219] S. Sasabe, Welding of 2000 series aluminium alloy materials, Welding Int. 26 (2012) 339-350.

[220] K.G. Basavakumar, P.G. Mukunda, M. Chakraborty, Impact toughness in Al-12Si and Al-12Si-3Cu cast alloys−Part 1: Effect of process variables and microstructure, Int. J. Impact. Eng. 35 (2008) 199-205.

[221] N. Kang, P. Coddet, H.L. Liao, T. Baur, C. Coddet, Wear behavior and microstructure of hypereutectic Al-Si alloys prepared by selective laser melting, Appl. Surf. Sci. 378 (2016) 142-149.

[222] M. Zeren, Effect of copper and silicon content on mechanical properties in Al-Cu-Si-Mg alloys, J. Mater. Process. Tech. 169 (2005) 292-298.

[223] P. Sadeesh, M. Venkatesh Kannan, V. Rajkumar, P. Avinash, N. Arivazhagan, K. Devendranath Ramkumar, S. Narayanan, Studies on Friction Stir Welding of AA 2024 and AA 6061 Dissimilar Metals, Procedia Eng. 75 (2014) 145-149.

[224] S.L. Sing, L.P. Lam, D.Q. Zhang, Z.H. Liu, C.K. Chua, Interfacial characterization of SLM parts in multi-material processing: Intermetallic phase formation between AlSi10Mg and C18400 copper alloy, Mater. Charact. 107 (2015) 220-227.

[225] X. Cao, W. Wallace, J.P. Immarigeon, C. Poon, Research and Progress in Laser Welding of Wrought Aluminum Alloys. II. Metallurgical Microstructures, Defects, and Mechanical Properties, Mater. Manuf. Processes 18 (2003) 23-49.

[226] Y.Q. Li, Y.Y. Shen, M.C. Leu, H.L. Tsai, Building Zr-based metallic glass part on Ti-6Al-4V substrate by laser-foil-printing additive manufacturing, Acta Mater. 144 (2018) 810-821.

[227] R.K.W. Marceau, G. Sha, R.N. Lumley, S.P. Ringer, Evolution of solute clustering in Al-Cu-Mg alloys during secondary ageing, Acta Mater. 58 (2010) 1795-1805.

[228] S. Gao, C.S. Wu, G.K. Padhy, L. Shi, Evaluation of local strain distribution in ultrasonic enhanced Al 6061-T6 friction stir weld nugget by EBSD analysis, Mater. Des. 99 (2016) 135-144.

[229] J. Zeisig, N. Schädlich, L. Giebeler, J. Sander, J. Eckert, U. Kühn, J. Hufenbach, Microstructure and abrasive wear behavior of a novel FeCrMoVC laser cladding alloy for high-performance tool steels, Wear 382-383 (2017) 107-112.

[230] A. Strondl, O. Lyckfeldt, H. Brodin, U. Ackelid, Characterization and Control of Powder Properties for Additive Manufacturing, JOM 67 (2015) 549-554.

[231] M.K. Stanford, C. DellaCorte, D. Eylon, Effect of Particle Morphology on Flow Characteristics of a Composite Plasma Spray Powder, J. Therm. Spray. Techn. 13 (2004) 586-592.

[232] X.J. Wang, L.C. Zhang, M.H. Fang, T.B. Sercombe, The effect of atmosphere on the structure and properties of a selective laser melted Al-12Si alloy, Mater. Sci. Eng., A 597 (2014) 370-375.

[233] P. Wei, Z. Wei, Z. Chen, J. Du, Y. He, J. Li, Y. Zhou, The AlSi10Mg samples produced by selective laser melting: single track, densification, microstructure and mechanical behavior, Appl. Surf. Sci. 408 (2017) 38-50.

[234] D.D. Gu, D.H. Dai, Role of melt behavior in modifying oxidation distribution using an interface incorporated model in selective laser melting of aluminum-based material, J. Appl. Phys. 120 (2016) 083104.

[235] W.P. Liu, Computational analysis and prediction of weld-solidification cracking, Comput. Mater. Sci. 4 (1995) 211-219.

[236] I. Yadroitsev, P. Bertrand, I. Smurov, Parametric analysis of the selective laser melting process, Appl. Surf. Sci. 253 (2007) 8064-8069.

[237] I. Yadroitsev, P. Krakhmalev, I. Yadroitsava, S. Johansson, I. Smurov, Energy input effect on morphology and microstructure of selective laser melting single track from metallic powder, J. Mater. Process. Tech. 213 (2013) 606-613.

[238] P. Wang, L. Deng, K.G. Prashanth, S. Pauly, J. Eckert, S. Scudino, Microstructure and mechanical properties of Al-Cu alloys fabricated by selective laser melting of powder mixtures, J. Alloys Compd. 735 (2018) 2263-2266.

[239] C. Wolverton, Crystal structure and stability of complex precipitate phases in Al-Cu-Mg-(Si) and Al-Zn-Mg alloys, Acta Mater. 49 (2001) 3129-3142.

[240] A. Riemer, S. Leuders, M. Thöne, H.A. Richard, T. Tröster, T. Niendorf, On the fatigue crack growth behavior in 316L stainless steel manufactured by selective laser melting, Eng. Fract. Mech. 120 (2014) 15-25.

[241] S. Leuders, M. Thöne, A. Riemer, T. Niendorf, T. Tröster, H.A. Richard, H.J. Maier, On the mechanical behaviour of titanium alloy TiAl6V4 manufactured by selective laser melting: Fatigue resistance and crack growth performance, Int. J. Fatigue 48 (2013) 300-307.

[242] Y.C. Chen, J.C. Feng, H.J. Liu, Precipitate evolution in friction stir welding of 2219-T6 aluminum alloys, Mater. Charact. 60 (2009) 476-481.

[243] S.C. Wang, M.J. Starink, N. Gao, Precipitation hardening in Al-Cu-Mg alloys revisited, Scr. Mater. 54 (2006) 287-291.

[244] Y. Chen, N. Gao, G. Sha, S.P. Ringer, M.J. Starink, Microstructural evolution, strengthening and thermal stability of an ultrafine-grained Al-Cu-Mg alloy, Acta Mater. 109 (2016) 202-212.

[245] A. Hekmat-Ardakan, X. Liu, F. Ajersch, X.G. Chen, Wear behaviour of hypereutectic Al-Si-Cu-Mg casting alloys with variable Mg contents, Wear 269 (2010) 684-692.

[246] M.H. Goodarzy, H. Arabi, M.A. Boutorabi, S.H. Seyedein, S.H. Hasani Najafabadi, The effects of room temperature ECAP and subsequent aging on mechanical properties of 2024 Al alloy, J. Alloys Compd. 585 (2014) 753-759.

[247] Z. Liu, P.H. Chong, A.N. Butt, P. Skeldon, G.E. Thompson, Corrosion mechanism of laser-melted AA 2014 and AA 2024 alloys, Appl. Surf. Sci. 247 (2005) 294-299.

[248] G.R. Ebrahimi, A. Zarei-Hanzaki, M. Haghshenas, H. Arabshahi, The effect of heat treatment on hot deformation behaviour of Al 2024, J. Mater. Process. Tech. 206 (2008) 25-29.

[249] Z. Huda, N.I. Taib, T. Zaharinie, Characterization of 2024-T3: An aerospace aluminum alloy, Mater. Chem. Phys. 113 (2009) 515-517.

[250] J.C.B. Bertoncello, S.M. Manhabosco, L.F.P. Dick, Corrosion study of the friction stir lap joint of AA7050-T76511 on AA2024-T3 using the scanning vibrating electrode technique, Corros. Sci. 94 (2015) 359-367.

[251] D.A. Rigney, The roles of hardness in the sliding behavior of materials, Wear 175 (1994) 63-69.

[252] R. Liu, D.Y. Li, Modification of Archard's equation by taking account of elastic/pseudoelastic properties of materials, Wear 251 (2001) 956-964.

[253] J.F. Archard, W. Hirst, The wear of metals under unlubricated conditions, Proc. R. Soc. Lond. A 236 (1956) 397-410.

[254] M.J. Starink, N. Gao, L. Davin, J. Yan, A. Cerezo, Room temperature precipitation in quenched Al-Cu-Mg alloys: a model for the reaction kinetics and yield strength development, Phil. Mag. 85 (2005) 1395-1417.

[255] F. Wang, H. Liu, Y. Ma, Y. Jin, Effect of Si content on the dry sliding wear properties of spray-deposited Al-Si alloy, Mater. Des. 25 (2004) 163-166.

[256] Q. Xiao, H. Liu, D. Yi, D. Yin, Y. Chen, Y. Zhang, B. Wang, Effect of Cu content on precipitation and age-hardening behavior in Al-Mg-Si-xCu alloys, J. Alloys Compd. 695 (2017) 1005-1013.

[257] T.C. Timmes, Electrocoagulation pretreatment prior to ultrafiltration, Department of Civil and Environmental Engineering, The Pennsylvania State University, 2009.

[258] E. McCafferty, Validation of corrosion rates measured by the Tafel extrapolation method, Corros. Sci. 47 (2005) 3202-3215.

[259] P. Marcus, Introduction to the fundamentals of corrosion, ASM handbook, Vol. 13A, ASM International, 2003.

[260] P.F. Gostin, D. Eigel, D. Grell, J. Eckert, E. Kerscher, A. Gebert, Comparing the pitting corrosion behavior of prominent Zr-based bulk metallic glasses, J. Mater. Res. 30 (2014) 233-241.

[261] W.J. Liang, P.A. Rometsch, L.F. Cao, N. Birbilis, General aspects related to the corrosion of 6xxx series aluminium alloys: Exploring the influence of Mg/Si ratio and Cu, Corros. Sci. 76 (2013) 119-128.

[262] Q. Meng, G.S. Frankel, Effect of Cu content on corrosion behavior of 7xxx series Aluminum alloys, J. Electrochem. Soc. 151 (2004) B271.

[263] Y. Kim, R.G. Buchheit, A characterization of the inhibiting effect of Cu on metastable pitting in dilute Al-Cu solid solution alloys, Electrochim. Acta 52 (2007) 2437-2446.

[264] S.J. Ketcham, Polarization and stress-corrosion studies of an Al-Cu-Mg alloy, Corros. Sci. 7 (1967) 305-314.

[265] S.J. Ketcham, F.H. Haynie, Electrochemical behavior of aluminum alloys susceptible to intergranular corrosion. I. effect of cooling elate on structure and electrochemical behavior in 2024 Aluminum alloy, Corrosion 19 (1963) 242-246.

[266] H. Pokhmurska, L. Kwiatkowski, W. Kalita, J. Hoffman, Corrosion behavior of laser-remelted aluminum alloy, Laser Technology VII: Applications of Lasers, International Society for Optics and Photonics, 2003, pp. 260-266.

[267] R. Li, M.G.S. Ferreira, A. Almeida, R. Vilar, K.G. Watkins, M.A. McMahon, W.M. Steen, Localized corrosion of laser surface melted 2024-T351 aluminium alloy, Surf. Coat. Technol. 81 (1996) 290-296.

[268] K. Watkins, M. McMahon, W. Steen, Microstructure and corrosion properties of laser surface processed aluminium alloys: a review, Mater. Sci. Eng., A 231 (1997) 55-61.

[269] N. Birbilis, R.G. Buchheit, Electrochemical Characteristics of Intermetallic Phases in Aluminum Alloys, J. Electrochem. Soc. 152 (2005) B140.

[270] J.R. Davis, Corrosion of aluminum and aluminum alloys, Asm International. 1999.

[271] G. Svenningsen, M.H. Larsen, J.H. Nordlien, K. Nisancioglu, Effect of high temperature heat treatment on intergranular corrosion of AlMgSi(Cu) model alloy, Corros. Sci. 48 (2006) 258-272.

[272] C. Jiang, Z.K. Liu, Computational investigation of constitutional liquation in Al-Cu alloys, Acta Mater. 51 (2003) 4447-4459.

[273] J.L. Murray, The aluminium-copper system, International metals reviews 30 (1985) 211-234.

[274] Y. Guo, G. Liu, H. Jin, Z. Shi, G. Qiao, Intermetallic phase formation in diffusion-bonded Cu/Al laminates, J. Mater. Sci. 46 (2010) 2467-2473.

[275] B. Vrancken, L. Thijs, J.-P. Kruth, J. Van Humbeeck, Microstructure and mechanical properties of a novel β titanium metallic composite by selective laser melting, Acta Mater. 68 (2014) 150-158.

[276] S. Dadbakhsh, L. Hao, P.G.E. Jerrard, D.Z. Zhang, Experimental investigation on selective laser melting behaviour and processing windows of in situ reacted Al/Fe_2O_3 powder mixture, Powder Technol. 231 (2012) 112-121.

[277] H.B. Dong, P.D. Lee, Simulation of the columnar-to-equiaxed transition in directionally solidified Al-Cu alloys, Acta Mater. 53 (2005) 659-668.

[278] J.M. Quaresma, C.A. Santos, A. Garcia, Correlation between unsteady-state solidification conditions, dendrite spacings, and mechanical properties of Al-Cu alloys, Metall. Mater. Trans. A 31 (2000) 3167-3178.

[279] R.M. Srivastava, J. Eckert, W. Löser, B.K. Dhindaw, L. Schultz, Cooling Rate Evaluation for Bulk Amorphous Alloys from Eutectic Microstructures in Casting Processes, Mater. Trans. 43 (2002) 1670-1675.

[280] J.M. Park, N. Mattern, U. Kühn, J. Eckert, K.B. Kim, W.T. Kim, K. Chattopadhyay, D.H. Kim, High-strength bulk Al-based bimodal ultrafine eutectic composite with enhanced plasticity, J. Mater. Res. 24 (2011) 2605-2609.

[281] A. Pattnaik, A. Lawley, Deformation and fracture in Al-CuAl$_2$ eutectic composites, Metall. Mater. Trans. B 2 (1971) 1529-1536.

[282] Y.F. Han, Y.B. Dai, D. Shu, J. Wang, B.D. Sun, First-principles calculations on the stability of Al/TiB$_2$ interface, Appl. Phys. Lett. 89 (2006) 144107.

[283] M. Emamy, M. Mahta, J. Rasizadeh, Formation of TiB$_2$ particles during dissolution of TiAl$_3$ in Al-TiB$_2$ metal matrix composite using an in situ technique, Composites Science and Technology 66 (2006) 1063-1066.

[284] Q. Guo, L.T. Jiang, G.Q. Chen, D. Feng, D.L. Sun, G.H. Wu, SEM and TEM characterization of the microstructure of post-compressed TiB$_2$/2024Al composite, Micron 43 (2012) 380-386.

[285] L. Lu, M.O. Lai, F.L. Chen, Al-4 wt. % Cu composite reinforced with in-situ TiB$_2$ particles, Acta Mater. 45 (1997) 4297-4309.

[286] F. Chen, Z.N. Chen, F. Mao, T.M. Wang, Z.Q. Cao, TiB$_2$ reinforced aluminum based in situ composites fabricated by stir casting, Mater. Sci. Eng., A 625 (2015) 357-368.

[287] S.V. Kamat, J.P. Hirth, R. Mehrabian, Mechanical properties of particulate-reinforced aluminum-matrix composites., Acta Metall. 37 (1989) 2395-2402.

[288] R.M. Aikin, L. Christodoulou, The role of equiaxed particles on the yield stress of composites, Scr. Metall. Mater. 25 (1991) 9-14.

[289] S. Jayalakshmi, S. Gupta, S. Sankaranarayanan, S. Sahu, M. Gupta, Structural and mechanical properties of Ni60Nb40 amorphous alloy particle reinforced Al-based composites produced by microwave-assisted rapid sintering, Mater. Sci. Eng., A 581 (2013) 119-127.

[290] S. Jayalakshmi, S.V. Kailas, S. Seshan, Tensile behaviour of squeeze cast AM100 magnesium alloy and its Al$_2$O$_3$ fibre reinforced composites, Compos. Part A-Appl. S. 33 (2002) 1135-1140.

[291] N.J. Musson, T.M. Yue, The effect of matrix composition on the mechanical properties of squeeze-cast aluminium alloy-Saffil metal matrix composites, Mater. Sci. Eng., A 135 (1991) 237-242.

[292] T. Shanmugasundaram, M. Heilmaier, B.S. Murty, V. Subramanya Sarma, On the Hall-Petch relationship in a nanostructured Al-Cu alloy, Mater. Sci. Eng., A 527 (2010) 7821-7825.

[293] M.L. Wang, D. Chen, Z. Chen, Y. Wu, F.F. Wang, N.H. Ma, H.W. Wang, Mechanical properties of in-situ TiB_2/A356 composites, Mater. Sci. Eng., A 590 (2014) 246-254.

[294] B. Chen, S.K. Moon, X. Yao, G. Bi, J. Shen, J. Umeda, K. Kondoh, Strength and strain hardening of a selective laser melted AlSi10Mg alloy, Scr. Mater. 141 (2017) 45-49.

[295] L.L. Parimi, G.A. Ravi, D. Clark, M.M. Attallah, Microstructural and texture development in direct laser fabricated IN718, Mater. Charact. 89 (2014) 102-111.

[296] D.R. Askeland, P.P. Fulay, W.J. Wright, The Science and Engineering of Materials, Cengage Learning, United States, 2010.

[297] K.G. Prashanth, J. Eckert, Formation of metastable cellular microstructures in selective laser melted alloys, J. Alloys Compd. 707 (2017) 27-34.

[298] C.R. Hutchinson, S.P. Ringer, Precipitation processes in Al-Cu-Mg alloys microalloyed with Si, Metallurgical and Materials Transactions A 31 (2000) 2721-2733.

[299] B. Hu, I.M. Richardson, Microstructure and mechanical properties of AA7075(T6) hybrid laser/GMA welds, Mater. Sci. Eng., A 459 (2007) 94-100.

[300] M. Jones, P. Heurtier, C. Desrayaud, F. Montheillet, D. Allehaux, J. Driver, Correlation between microstructure and microhardness in a friction stir welded 2024 aluminium alloy, Scr. Mater. 52 (2005) 693-697.

[301] C. Genevois, A. Deschamps, A. Denquin, B. Doisneau-cottignies, Quantitative investigation of precipitation and mechanical behaviour for AA2024 friction stir welds, Acta Mater. 53 (2005) 2447-2458.

[302] J.Q. Su, T.W. Nelson, R. Mishra, M. Mahoney, Microstructural investigation of friction stir welded 7050-T651 aluminium, Acta Mater. 51 (2003) 713-729.

[303] B. Heinz, B. Skrotzki, Characterization of a friction-stir-welded aluminum alloy 6013, Metall. Mater. Trans. B 33 (2002) 489-498.

[304] C. Gallais, A. Denquin, Y. Bréchet, G. Lapasset, Precipitation microstructures in an AA6056 aluminium alloy after friction stir welding: Characterisation and modelling, Mater. Sci. Eng., A 496 (2008) 77-89.

[305] H.J. Liu, H. Fujii, M. Maeda, K. Nogi, Tensile properties and fracture locations of friction-stir-welded joints of 2017-T351 aluminum alloy, J. Mater. Process. Tech. 142 (2003) 692-696.

[306] H.J. Liu, H. Fujii, M. Maeda, K. Nogi, Heterogeneity of mechanical properties of friction stir welded joints of 1050-H24 aluminum alloy, J. Mater. Sci. Lett. 22 (2003) 441-444.

Publications

1. **P. Wang***, C. Gammer, F. Brenne, T. Niendorf, J. Eckert, Sergio Scudino, A heat treatable TiB_2/Al-3.5Cu-1.5Mg-1Si composite fabricated by selective laser melting: microstructure, heat treatment and mechanical properties, Compos. Part B- Eng. 147 (2018) 162-168.

2. S. Pauly, **P. Wang**, U. Kühn, K. Kosiba, Experimental determination of cooling rates in selectively laser-melted eutectic Al-33Cu, Additive Manufacturing 22 (2018) 753-757.

3. T. Lu, S. Scudino, W. Chen, **P. Wang**, D. Li, M. Mao, L. Kang, Y. Liu, Z. Fu, The influence of nanocrystalline $CoNiFeAl_{0.4}Ti_{0.6}Cr_{0.5}$ high-entropy alloy particles addition on microstructure and mechanical properties of SiCp/7075Al composites, Mater. Sci. Eng., A 726 (2018) 126-136.

4. T.W. Lu, W.P. Chen*, W.Y. Xu, **P. Wang****, M.D. Mao, Y.X. Liu, Z.Q. Fu, The effects of Cr particles addition on the aging behavior and mechanical properties of SiCp/7075Al composites, Mater. Charact. 136 (2018) 264-271.

5. L. Deng, S. Wang, **P. Wang**, U. Kühn, S. Pauly, Selective laser melting of a Ti-based bulk metallic glass, Mater. Lett. 212 (2018) 346-349.

6. **P. Wang***, C. Gammer, F. Brenne, K.G. Prashanth, R.G. Mendes, M.H. Rümmeli, T. Gemming, J. Eckert, S. Scudino, Microstructure and mechanical properties of a heat-treatable Al-3.5Cu-1.5Mg-1Si alloy produced by selective laser melting Mater. Sci. Eng., A 711 (2017) (562–570)

7. **P. Wang***, L. Deng, K.G. Prashanth, S. Pauly, J. Eckert and S. Scudino, Microstructure and mechanical properties of Al-Cu alloys fabricated by selective laser melting of powder mixtures J. Alloys Compd. 735 (2017) 2263-2266

8. **P. Wang***, H.C. Li, K.G. Prashanth, J. Eckert, S. Scudino, Selective laser melting of Al-Zn-Mg-Cu: Heat treatment, microstructure and mechanical properties, J. Alloys Compd. 707 (2017) 287-290.

9. T.W. Lu, W.P. Chen, **P. Wang**, M.D. Mao, Y.X. Liu, Z.Q. Fu, Enhanced mechanical properties and thermo-physical properties of 7075Al hybrid composites reinforced by the mixture of Cr particles and SiC_p, J. Alloys Compd.735 (2017) 1137-1144.

10. K.G. Prashanth, R. Damodaram, T. Maity, **P. Wang**, J. Eckert, Friction welding of selective laser melted Ti6Al4V parts, Mater. Sci. Eng., A 704 (2017) 66-71.

11. L. Zhang, H. Zhang, W. Li, T. Gemming, **P. Wang**, M. Bönisch, D. Şopu, J. Eckert, S. Pauly, β-type Ti-based bulk metallic glass composites with tailored structural metastability, J. Alloys Compd. 708 (2017) 972-981.

12. H. Li, F. Cao, S. Guo, Y. Jia, D. Zhang, Z. Liu, **P. Wang**, S. Scudino, J. Sun, Effects of Mg and Cu on microstructures and properties of spray-deposited Al-Zn-Mg-Cu alloys, J. Alloys Compd. 719 (2017) 89-96.

13. K.G. Prashanth, S. Scudino, A.K. Chaubey, L. Löber, **P. Wang**, H. Attar, F.P. Schimansky, F. Pyczak, J. Eckert, Processing of Al-12Si-TNM composites by selective laser melting and evaluation of compressive and wear properties, J. Mater. Res. 31(01) (2015) 55-65.

Erklärung

Hiermit versichere ich, dass ich die vorliegende Arbeit ohne unzulässige Hilfe Dritter und ohne Benutzung anderer als der angegebenen Hilfsmittel angefertigt habe; die aus fremden Quellen direkt oder indirekt übernommenen Gedanken sind als solche kenntlich gemacht. Bei der Auswahl und Auswertung des Materials sowie bei der Herstellung des Manuskripts habe ich Unterstützungsleistungen von folgenden Personen erhalten: Prof. Dr. J. Eckert und Dr. S. Scudino. Weitere Personen waren an der geistigen Herstellung der vorliegenden Arbeit nicht beteiligt. Insbesondere habe ich nicht die Hilfe eines kommerziellen Promotionsberaters in Anspruch genommen. Dritte haben von mir keine geldwerten Leistungen für Arbeiten erhalten, die in Zusammenhang mit dem Inhalt der vorgelegten Dissertation stehen. Die Arbeit wurde bisher weder im Inland noch im Ausland in gleicher oder ähnlicher Form einer anderen Prüfungsbehörde vorgelegt und ist auch noch nicht veröffentlicht worden. Dissertation wurde an der TU Dresden am Institut für Werkstoffwissenschaft der Fakultät Maschinenwesen unter der wissenschaftlichen Betreuung durch Prof. Dr.-Ing. habil. Dr. h.c. Jürgen Eckert angefertigt. Die Promotionsordnung der Fakultät Maschinenwesen der TU Dresden aus dem Jahre 2001 erkenne ich an.

....

Pei Wang
Dresden, 30.04.2018